Cartilage Biomechanical and Mechanobiological Response to Sliding Contact

by

Ali Shegaf

A thesis submitted to the
Faculty of Graduate and Postdoctoral Affairs
in partial fulfillment of the requirements for the degree of

Doctor of Philosophy in Mechanical Engineering

Ottawa-Carleton Institute for Mechanical and Aerospace Engineering
Department of Mechanical & Aerospace Engineering
Carleton University
Ottawa, Ontario
August, 2019

Abstract

Osteoarthritis (OA) is the leading cause of disability, worldwide. OA leads to breakdown of the articular cartilage (AC), the highly structured tissue that lines the end of bones of the synovial joints. The cartilage cells synthesize and maintain the homeostasis of articular cartilage, a function that is largely influenced by mechanical forces.

Mechanobiological studies of cartilage are conducted toward a better understanding of osteoarthritis pathological mechanism. However, the typically applied loading protocols omit the relative surface motion that is essential for cartilage tribological function. Therefore, this work aimed to examine the effects of a more physiological loading mode on cartilage mechanobiological function.

Finite element analysis (FEA) was performed to investigate the biomechanical response of cartilage to loading regimes that permits migrating contact area compared to uniaxial cyclic compression. Interstitial fluid pressure was maintained high under sliding contact while it reduced by 20% in cyclic compression model. Also, maximum fluid flow was reduced by 44% in uniaxial cyclic compression where fluid imbibition was limited to a small region near the lateral periphery. Cartilage surface curvature may contribute to cartilage mechanobiological function by increasing tissue rehydration.

Motivated by FE results, two low-cost mechanical testing devices were designed and constructed to allow for *in vitro* mechanobiological experimentation of cartilage. Healthy and degenerated human cartilage samples were subjected to two types of intermittent loading, load-controlled sliding and displacement-controlled unconfined cyclic compression. Changes in biochemical signals that are believed to control chondrocytes functionality were measured. The level of growth factor (TGF-β) was significantly higher in specimen subjected to sliding contact compared to cyclic compression. Also, the level of all measured cytokines

and TIMPs was always lower in sliding contact loading mode, although not statistically significant. These results suggest that the sliding contact loading mode does influence chondrocytes anabolic activities.

Results obtained from this thesis demonstrate the importance of incorporating realistic loading conditions in *in vitro* mechanobiological testing of cartilage. Findings of this work should contribute to the ongoing research on the role of chondrocytes in OA onset and progression toward developing therapeutic interventions and tissue engineering approaches for OA.

To my family in Canada and abroad...

Acknowledgments

Table of Contents

List of Tables

List of Figures

Nomenclature

List of Abbreviations

AC	Articular Cartilage
BCs	Boundary Conditions
BMD	Bone Mineral Density
BNS	Bovine Nasal Septum
BW	Body Weight
CLE	Conewise Linear Elasticity
CPM	Continuous Passive Motion
DZ	Deep Zone
ECM	ExtraCellular Matrix
FEBio	Finite Element for Biomechanics
FEA	Finite Element Analysis
FSR	Force Sensing Resistors
GAGs	GlycomsAminoGlycans
IAM	Intermittent Active Motion
LED	Light Emitting Diode
MMP	Matrix MetalloProteinase-
PBS	Phosphate-Buffered Saline
PGs	Proteoglycans

<u>List of Abbreviations.. Continued</u>

SZ	Superficial Zone
FNF	Femoral Neck Fracture
TIMP	Tissue Inhibitor of Metalloproteases
BMP	Bone Morphogenetic Protein
FGF	Fibroblast Growth Factor
IFN	Interferon
IL	Interleukin
LIF	Leukemia Inhibitory Factor
OSM	Oncostatin M
TGF	Transforming Growth Factor
TNF	Tumor Necrosis Factor
SF	Synovial Fluid
VEGF	Vascular Endothelial Growth Factor
CCL	Chemokine
CCR	Chemokine Receptor

List of Symbols

σ	Engineering stress
E	Young's modulus
ε	Total strain
ν	Poisson's ratio
p	Fluid pressure
σ_S	Solid phase stress
I	Linear transformation tensor
w	Volumetric flux
v^s	Velocity of the solid phase
k	Hydraulic permeability
k_0	Initial hydraulic permeability
σ_f	fibril network stress
σ_{nf}	non-fibrillar matrix stress
E_f	Strain-dependent stiffness
ε_f	Spring strain
E_f^0	Initial spring stiffness
ψ	Strain energy
J	Deformation tensor determinant
μ	First Lame parameter
λ	Second Lame parameter
ψ_f	Fiber strain energy
ξ	Fiber modulus (CFD)
I_n	The square of the fiber stretch
β	Fiber material property

List of Symbols .. Continued

H_{+A}	Tensile modulus
H_{-A}	Compressive modulus
δ	Contact depth
δ_s	Static equilibrium contact depth
δ_d	Dynamic equilibrium contact depth
h	Cartilage thickness
a	Contact radius
R	Spherical indenter radius
r	Cartilage specimen radius
D	Cartilage specimen diameter
d	Sliding distance
v	Sliding speed
W	Applied load
W^p	Fluid load support
E_C	Contact modulus
E_s	Static contact modulus
E_d	Dynamic contact modulus
R^2	Coefficient of determination
V	Voltage
I_{max}	Max current
L	Stepper motor inductance
$s.p.r$	Steps per revolution
η	Efficiency of ball screw
P	Lead of ball screw

Chapter 1

Introduction and Background

1.1 Osteoarthritis

Arthritis is an inflammatory disease that affects the synovial joints and some of its symptoms are pain, stiffness, and swelling of the joint. More than 100 conditions of arthritis exist; however, there are two main types of arthritis: inflammatory arthritis and osteoarthritis. Osteoarthritis (OA) alone affects nearly 13% of Canadian adults and 57% of those are below the age of 65 (Dunlop et al., 2003; O'Donnell et al., 2011). A large portion of people with osteoarthritis suffers from daily pain and limited activities. As a result, they earn lower income and tend to be socially isolated and depend on governmental aid for living (Badley, 1995). In the year 2010, the impact of osteoarthritis on the Canadian economy was estimated to be 27.5 billion dollars (Bombardier et al., 2012). Two thirds of the total osteoarthritis related costs are attributed to the loss of productivity due to long term disability. The remaining costs are directly spent on health care expenses. The number of affected people as well as the associated disabilities and economic costs are expected to escalate with an aging population (Bombardier et al., 2012; Badley and Wang,

1998). Prevention or slowing of disease progression would therefore greatly benefit patients and the economy. However, such strategies are difficult to develop since in most cases the cause of OA is unknown.

Osteoarthritis is a disorder that causes cartilage degeneration and decreased joint space, see Figure 1.1. However, it also causes changes in bone structure of joints, deterioration of tendons and ligaments, and inflammation of the joint synovium. In late stages of OA, the cartilage completely wears away causing bone-bone contact. Osteophytes or bone spurs also grow on the margins of articular surfaces and cause increased pain and friction. Diagnosis of OA is usually performed only after the disease symptoms appear and at that stage the cartilage is usually severely degenerated (Taljanovic et al., 2008; Mao et al., 2014).

Figure 1.1: OA in the hip joints. Visible narrowing in the joint space in the left hip, indicative of cartilage loose. Increased subchondral bone density is also obvious in the same joint. With permission from (Taljanovic et al., 2008).

Osteoarthritis can affect any joint in the human body but most commonly affects the lower extremity joints and mainly the hip and knee joints. Osteoarthritis is more common in elderly people, though young people are not safe from OA. Other factors such as obesity, trauma, female sex, and family history could contribute to

the risk of developing OA (Ipresc and Barr, 2015; Gosvig et al., 2010).

To date, there are no medical treatments that are proven to prevent or delay the onset of OA mostly due to poor understanding of the mechanisms of the disease pathology. Therefore, treatments for OA focus on symptom management. During early and moderate stages of the disease, treatments usually involve some nonsurgical measures such as weight loss, physical therapy, various aids, and anti-inflammatory medications. At later stages of osteoarthritis and due to severe pain and disability, surgical intervention and replacement of the joint with an artificial one (joint arthroplasty) may become necessary. Therefore, understanding the initiation and the progression of OA during its early stages is prerequisite for improving the diagnosis, treatments, and prevention techniques.

1.2 Synovial Joints

Synovial joints, also known as diarthroial joints, are the most common and movable joints in the animal skeletal system. The knee, hip, and shoulder are typical examples of the synovial joints. The purpose of synovial joints is to transmit large loads acting in various directions while providing low friction motion throughout an individuals' lifetime.

The main features of a synovial joint are illustrated in Figure 1.2. Essentially, the end of bones in a synovial joint are coated by a thin layer of hyaline cartilage, known as articular cartilage. This tissue is well adapted to support the contact forces in the joint while providing almost friction-free motions. The bone layer below the articular cartilage, called subchondral bone, acts as hard backing material. The entire joint is encapsulated by a fibrous capsule that is further supported by ligaments and muscles. The inner surface of the joint capsule is lined by a layer of

a connective tissue called synovium or synovial membrane. The synovium main function is to secret the synovial fluid (SF) that is primarily made of water (85%), hyaluronic acid, and proteins. Synovial fluid fills the joint cavity and acts as a lubricant to the articulating surfaces (Mitchell, 2003; Dowson, 2012).
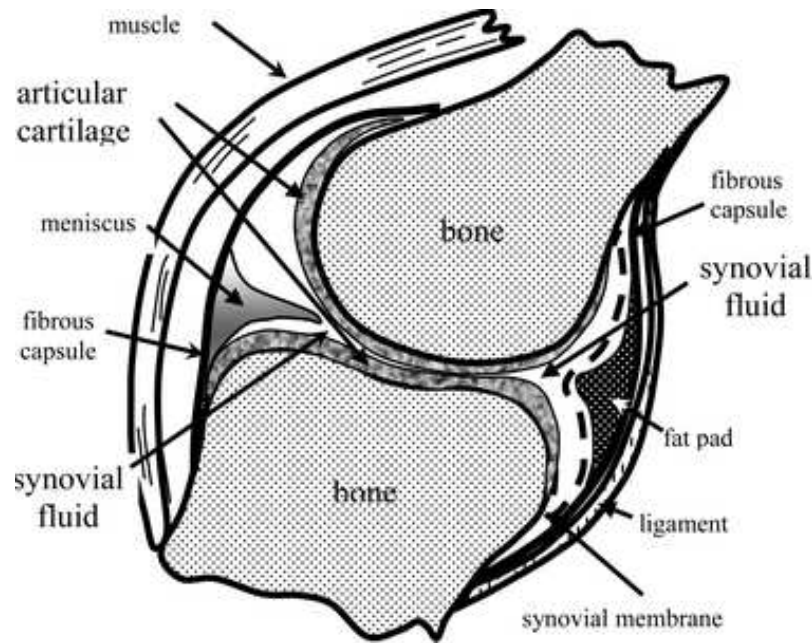
Figure 1.2: Essential features of a synovial joint. With permission from (Dowson, 2012).

Large joints in the lower extremity may contain additional fibrous tissue such as the labrum in the hip joint which is believed to provide a sealing mechanism against fluid expression from the joint space (Ferguson et al., 2000, 2003; Haemer et al., 2012) or the meniscus in the knee joint which is known for its role in load transmission (Radin et al., 1984; Dowson, 2012). These fibrous tissues are subjected to repetitive and large forces which may lead to injury. Labrum tear and meniscus damage are very common causes for joint instability which may ultimately lead to osteoarthritis (Blalock et al., 2015).

1.2.1 Articular Cartilage - Composition

The articular cartilage (AC) is a form of hyaline cartilage that lines the end of bones in synovial joints. It is an avascular and aneural porous tissue that is saturated with water. Chondrocytes are the only cell type in articular cartilage, and they synthesize and secrete the extracellular cartilage matrix components and enzymes that maintain or degrade the tissue under certain conditions. The hyaline cartilage is a metabolically active tissue and the integrity of extracellular matrix is maintained by balanced degradation and synthesis processes. During maturation, the composition of articular cartilage experiences significant development in adaptation to external loads it is subjected to. The solid matrix of a mature cartilage is primarily made of a ground substance, proteoglycans (PGs), that is reinforced by collagen fibrils. The articular cartilage thickness is subject and location dependent and it is generally accepted that cartilage thickness increases with body size. Human articular cartilage thickness, however, normally ranges from 1.0 to 2.5 mm with thicker cartilage being found in large and incongruent joints (e.g. knee) (Shepherd and Seedhom, 1999).

Extracellular Matrix (ECM)

The extracellular matrix of articular cartilage is made of porous ground substance that is reinforced by collagen fibrils and saturated with water. The ground substance of the solid matrix is primarily made of proteoglycan aggrecan which comprise between 22 - 38% of the articular cartilage dry weight. Proteoglycans are large macromolecules consisting of glycosaminoglycans (GAGs) and oligosaccharides that are attached to a core protein. The core protein is attached to hyaluronic

acid by link protein to form the proteoglycan aggregate, see Figure 1.3. The glycosaminoglycans include chondroitin sulfate and keratan sulfate which makes proteoglycans highly negatively charged molecules. During normal function of articular cartilage, PGs play an important role in restoration of the original tissue dimensions by osmotically reabsorbing the interstitial water and small solutes released during compression.
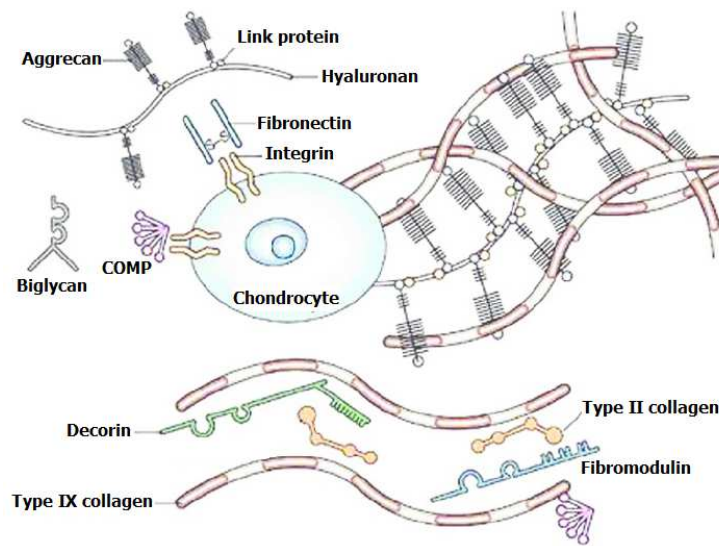
Figure 1.3: AC matrix composition, reproduced with permission from (Sophia Fox et al., 2009).

Like many other connective tissues in the human body, hyaline cartilage is primarily made of collagen fibrils which make 40 to 70% of its total dry weight. Several types of collagen (i.e., types VI, IX, and XI) can be found within the solid matrix; however, collagen II is the predominant fibrous component of articular cartilage as it accounts for $90 - 95\%$ of collagen in hyaline cartilage (Ateshian et al., 1994). The collagen structure is mainly observed in long fibers that group together in bundles with a preferred orientation that varies through the tissue depth.

The solid matrix of articular cartilage is filled with interstitial fluid, mainly water, that accounts for 75 - 80% of the tissue wet weight. Water is also the main

component of the synovial fluid that is found in the joint capsule. Most of the
interstitial water is freely exchangeable with outside medium by diffusion. Since
cartilage lacks a vascular network (Maroudas, 1979), interstitial fluid plays an im-
portant role in transporting of nutrients and minerals through the tissue and re-
moving waste products. Mechanically, movement of the interstitial water through
the cartilage pores, of approximately 6.0 nm (Maroudas, 1979; Mow et al., 1992),
induces large drag forces which provides the tissue with high compressive stiff-
ness (Mow and Guo, 2002). Further, squeezing the water out of the tissue surface
is thought to help in joint lubrication (McCutchen, 1962).

Chondrocytes

Chondrocytes, which means "cartilage cells" in Greek, are the sole type of living
cells in articular cartilage. Chondrocytes constitute around 2% of the total tissue
volume (Alford and Cole, 2005). That is a very low density compared to other
surrounding tissues, e.g. 4-6% bone cells (Capulli et al., 2014). Chondrocytes size,
shape, and density varies through the cartilage depth. However, the chondrocyte
diameter ranges from 10 - 13 μm. They are thought to be post-mitotic, i.e. they
stop differentiating after growth has ceased but survive individuals' lifetime. The
primary function of chondrocytes is to produce proteins that compose the extracel-
lular matrix, such as collagen and proteoglycans. Under certain conditions chon-
drocytes may release molecules associated with inflammation e.g. cytokines, or
enzymes that break down the extracellular matrix e.g. collagenase or ADAMTS5.
The factors influencing this are not completely understood, but the micromechan-
ical environment of the cell is believed to play a crucial role (Guilak, 2011). The
normal function of the chondrocytes has also been found to be largely influenced

by mechanical stimuli which have been shown to differently modulate the chondrocytes biosynthetic activities, depending on the specific loading protocol, magnitude, and frequency (Muir, 1995). Since nutrition of articular cartilage relies on diffusion from outside, chondrocytes are well adapted to low oxygen conditions (Brighton and Heppenstall, 1971).

1.2.2 Articular Cartilage - Structure

The concentration and distribution of the cells and the extracellular matrix components varies through the depth. Most notably, variation in chondrocytes morphology and distribution as well as collagen fibers orientation. Therefore, three successive layers can be identified through the cartilage thickness, as shown in Figure 1.4.
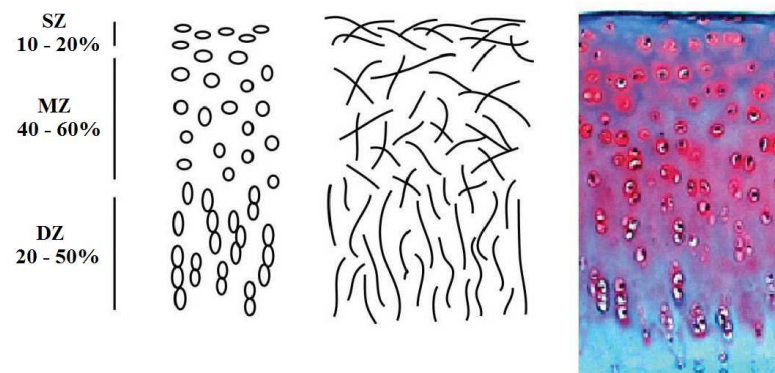
Figure 1.4: Zonal structure of articular cartilage identified by cells shape and orientation, left, and collagen fibers, middle. With permission from (Athanasiou et al., 2009)

The top layer, the superficial tangential zone (SZ), makes about 10-20% of the cartilage thickness. In this layer, the concentration of collagen fibers is high, and they are organized in bundles that are oriented in a plane parallel to the cartilage surface. The water content is high ($> 80\%$), in this zone, and the proteoglycans content is at the lowest level. The PGs are strongly cross-linked with the collagen

fibers which promotes the in plane mechanical properties of the cartilage surface such as shear strength (Mow and Guo, 2002; Alford and Cole, 2005; Fox et al., 2009). Chondrocytes in this zone are dense and relatively smaller in diameter compared to other zones. They are flattened and have a more discoidal shape.

The middle zone (MZ) is the thickest layer of the articular cartilage and represents approximately 50% of the total thickness of the tissue. In this zone, the collagen fibers do not show preferred direction of orientation, they are random or arc-like oriented. The PG content in this layer increases to the highest level and balanced by the decrease in the water and the collagen content. Compared to superficial zone, chondrocytes in the middle zone are more rounded and larger in size. However, they are less dense and randomly distributed in this layer. Due to the random orientation of the collagen fibers, the mechanical properties of this zone could be considered isotropic. This layer provides a transition zone between the top and deep layers (Mow and Guo, 2002; Alford and Cole, 2005; Fox et al., 2009).

In the deep zone (DZ), the collagen fibers are vertically oriented and extend into the calcified cartilage. In this zone, the cells have elliptic shape and organized in columns perpendicular to the tissue surface. The PG content in the deep zone is high but the water is at its lowest level. Due to high PG content, the deep zone is thought to provide the tissue with the highest amount of resistance to compressive forces. Another role of this layer is to ensure a strong fixation of the articular cartilage to the subchondral bone by extending the collagen fibrils through the tidemark and into the calcified cartilage.

The calcified cartilage is often considered as the forth zone in the articular cartilage. The tide mark is the boundary between the deep zone and the calcified cartilage. The calcified cartilage layer is very thin, ranging from 3% to 8% of the

tissue's depth (Müller-Gerbl et al., 1987), and the cartilage is calcified with crystals of calcium salts. The calcified cartilage region provides a transition between the cartilage and the stiff subchondral bone plate. The stiffness of this layer is many times higher (10 - 100 times) than that of the hyaline cartilage but still more than one order of magnitude lower than that of the underlying subchondral bone plate (Oegema et al., 1997; Mente and Lewis, 1994; Bullough and Jagannath, 1983).

1.2.3   Biomechanical Properties of Articular Cartilage

Being multiphasic, inhomogeneous and anisotropic structure, the articular cartilage exhibits highly complex behavior. The cartilage is known to demonstrate fluid-dependent and fluid-independent visco-elasticity (Mow et al., 1980; Ateshian, 2009). When the tissue is loaded in compression, the interstitial fluid flow through the porous matrix induces high drag forces between the two phases due to the low permeability of the cartilage, in the range of $10^{-15}\ m^4/N.s$ (Athanasiou et al., 1991) creating large fluid pressure and pressure gradients (Mow et al., 1980). As the fluid leaves the tissue, it gradually decreases in thickness and the load is gradually transferred to the solid phase. At equilibrium, as the fluid flow ceases, the load is entirely carried by the solid phase. Under load, the solid matrix also exhibits flow-independent visco-elasticity. When the external load is removed the cartilage restores its original shape and volume that was lost by fluid exudation. The elasticity of the solid matrix as well as some electrostatic forces and swelling pressure contribute to this behavior (Wilson et al., 2005; Mohammadi et al., 2013).

The articular cartilage also exhibits tension-compression nonlinearity that is imparted by collagen fibrils anisotropic distribution and orientation. The collagen fibers resist only tensile forces; thus, the cartilage stiffness in tension is much higher than that in compression (Soltz and Ateshian, 2000; Fox et al., 2009). The

tensile stiffness of cartilage is also much higher in the superficial zone compared to middle and deep zones (Ruggiero et al., 2015).

Although the articular cartilage behavior in compression is mainly governed by PGs, the collagen fibrils also contribute to the cartilage stiffness in compression by resisting the lateral expansion of the tissue which increases the fluid pressure. Further, the collagen fibrils enhance the cartilage in-plane mechanical properties, such as shear stress, under small deformation that does not cause change in volume (Bader et al., 1992; Zhu et al., 1993). Moreover, the concentration of ECM components and interstitial water contents as well as the orientation of collagen fibrils and chondrocytes varies through the depth. This variation produces depth dependent material properties; thus, cartilage stiffness and permeability varies through the depth (Chen et al., 2001; Federico and Herzog, 2008a).

1.3 Testing of Articular Cartilage

1.3.1 Compression Testing

Typically, compression tests are performed on cartilage under three types of loading configurations: confined compression, unconfined compression, or indentation as shown in Figure 1.5. In confined compression test, Figure 1.5 (i), the specimen is axially compressed using porous rigid platen while the lateral deformation of the specimen is prevented by the confining chamber walls. The advantage of confined compression test is reducing the problem to one dimension and hence analytical solution can be obtained. However, experiments have shown that surface interdigitation into the pores of the compressing platen and incomplete confinement are difficult to avoid in this loading configuration (Buschmann et al., 1997).
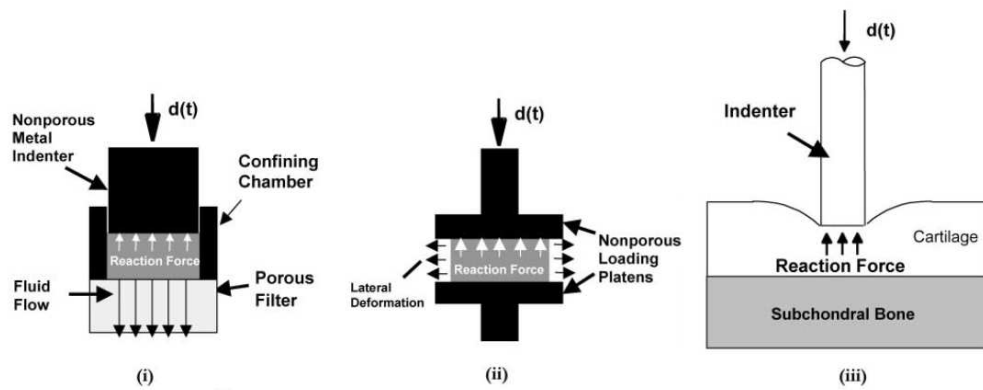
Figure 1.5: Schematics of loading protocols used for articular cartilage testing. With permission from (DiSilvestro and Suh, 2001).

In unconfined compression, as the name implies, the tissue can expand in the lateral direction as it is compressed axially with an impermeable rigid platen (DiSilvestro et al., 2001). This configuration is also difficult to perform as it requires the use of a sample with a flat surface which does not occur naturally in most joints. Investigators usually work around that by using samples with small diameter (e.g. 3 mm) and remove the bone layer to allow the cartilage layer to lay flat. However, stripping the cartilage off from the bone could affect the mechanical behavior of the tissue as the cartilage is pre-stressed while attached to the subchondral bone. Furthermore, the removal of bone also removes the constraints to lateral expansion of the deep layer of the cartilage.

Indentation testing of cartilage is performed using a compression tool, (e.g. indenter), that is relatively small in size compared to the cartilage sample (Mak et al., 1987; Mow et al., 1989). Indenters with different geometries (flat, spherical, cylindrical, etc.) have been previously used. A schematic diagram of an indentation test is shown in Figure 1.5, (iii). It is an attractive technique as it doesn't require further sample preparation (e.g. removing the bone layer in unconfined compression or cutting the perfect sample dimensions in unconfined compression). This makes

indentation test easy to perform in both *in vitro* and *in vivo* experiments. However, indentation test is associated with complex boundary conditions and hence the solution cannot be directly obtained via theoretical analysis. Therefore, finite element constitutive models (linear elastic, visco-elastic, biphasic) are used to extract the material properties using standard testing approaches (i.e., indentation and creep or stress relaxation). Using these loading configurations two uniaxially compression tests are commonly performed,stress relaxation or creep test. Figure 1.6 illustrates the typical response of articualar cartilage to stress relaxation and creeps test.
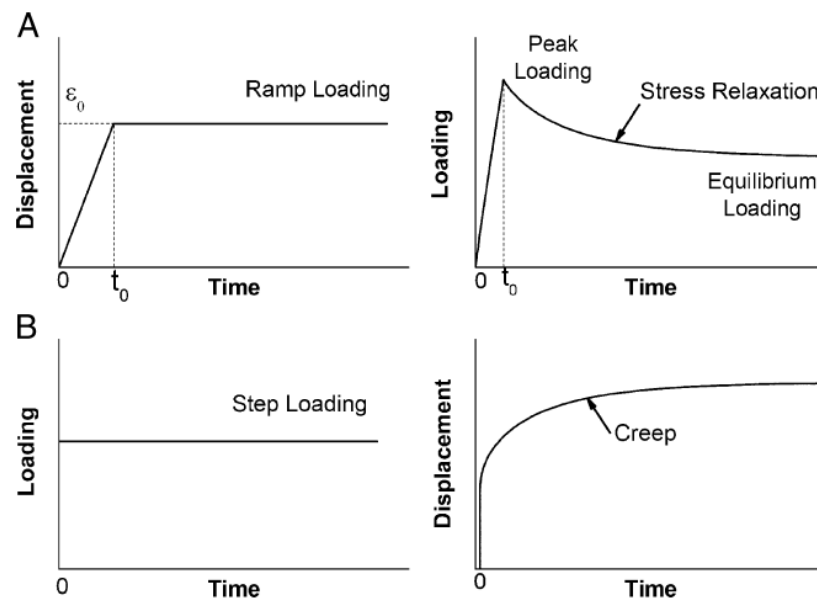
Figure 1.6: Stress-relaxation (top) and creep (bottom) testing protocols. With permission from (Lu and Mow, 2008).

In a stress relaxation test, a predetermined level of compressive strain is applied on the cartilage sample at constant rate and then kept constant while the tissue is left to relax until equilibrium is reached. Hence, stress relaxation can be described

as the reduction in reaction force observed from a constant deformation application. In a creep test, on the other hand, the tissue deforms under a constant force, usually applied in stepwise manner, until equilibrium is reached. Therefore, creep is the increase in strain under constant force or the tendency of the tissue to deform under a constant stress. These tests are frequently used to study the articular cartilage response to compression which in turn is used for estimating the material properties.

1.3.2 Tensile Testing

Tensile testing on cartilage is not as common as compression testing. However, these tests are useful for studying the tissue response to tensile forces. Tensile tests are conducted on samples with length that is greater than their width, length to width ratio no less than four, such that uniform strain can be assumed to occur through the specimen length (Woo et al., 1979). As with compression tests, tensile testing can be conducted in both creep and relaxation modes. Extensometers or optical techniques are used to measure the strain in the specimen and the results are plotted against the applied stress (Guilak et al., 1994b; Mow and Guo, 2002).

As illustrated in Figure 1.7, a region of non-linear relationship between the stress and strain with relatively high strain is observed early in the test. This region represents the straightening of the wavy-like collagen fibrils and its called the toe region. As the load increases, a linear relationship between stress and strain is seen due to the contribution of the collagen fibrils to the tensile stiffness. Tensile modulus is usually obtained from this linear region of the stress strain curve. The mechanical response of the tissue in this case is primarily due to the collagen fibrils although the proteoglycans also indirectly contribute (Mow and Guo, 2002).
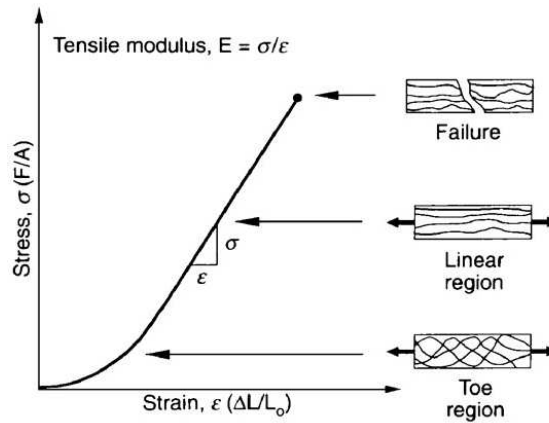
Figure 1.7: A stress-strain diagram for articular cartilage during tensile loading. With permission from Mow and Guo (2002).

1.3.3 Shear Testing

Cartilage shear tests are performed in unconfined compression configuration. Similar to unconfined compression, the first step in cartilage shear test is to assure full contact between the compression platen and the cartilage surface by applying a small tare load. The shear load can then be applied parallel to the surface using rotational (Stading and Langer, 1999) or translational displacement (Anderson et al., 1991). Ideally, the sample should change shape without any fluid flow that may be a result of compressive or tensile effects. Similar to tensile testing, the equilibrium shear modulus, G, is calculated from the linear region of the stress-strain curve.
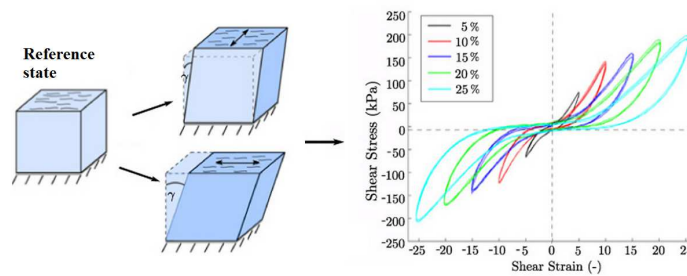
Figure 1.8: Cartilage shear test performed at differnt strain levels in two perpendicular directions. With permission from Maier et al. (2017).

1.4 FE Modeling of Articular Cartilage

Traditionally, finite element analysis (FEA) is used by engineers to solve complex problems where the analytical solution is not achievable. This method reduces the number of degrees of freedom of the domain of interest to a finite number by dividing it into a finite number of subdivisions/elements and solving the global matrix that combines all equations of the local element (Chandrupatla et al., 2002).

In the field of biomechanics, finite element analysis has been used, for decades, to study the biomechanics and, more recently, the mechanobiology of different biological structures. It is an attractive method as it allows for the non-invasive measurement of biomechanical parameters that are experimentally challenging such as fluid flow and fluid pressure within hydrated tissues (e.g. articular cartilage). Furthermore, using FEA, the parameters of interest (e.g. stress or strain) can be predicted throughout the system rather than a limited number of discrete locations as in experimental investigations.

Although articular cartilage was long recognized as a biphasic material that constitutes solid and fluid phases, early models of the articular cartilage were simplified single phased, linear elastic, isotropic, and homogeneous material (Roth and Mow, 1977). Hence, this model was only appropriate when the cartilage is loaded instantaneously or when the fluid flow has ceased as under such instances there is no fluid flow effects and the tissue behaves as an incompressible material (Mow et al., 1980; Ateshian et al., 1994; Soltz and Ateshian, 2000). When large strains are expected, the hyper-elasticity is favored. Hyper-elastic materials (e.g. NeoHookean and MooneyRivlin) use strain energy potential which makes them more accurate than linear elastic material at high strains and hence suitable for modeling rubber-like material.

1.4.1 Biphasic Models

As early generations of the cartilage models, single phased models, were not able to replicate the time dependent response of the tissue which results from the interstitial fluid exudation, biphasic model of cartilage was introduced (Mow et al., 1980). In this model, the articular cartilage was modeled as biphasic material that constitute both fluid and solid phases. Upon loading, the load is initially entirely carried by the fluid phase but gradually transferred to the solid phase due to fluid exudation over time. That results in gradual tissue consolidation and increased solid stresses/strains. At equilibrium, as the fluid flow ceased, the load is entirely supported by the solid phase. Hence, the total mechanical stress in simple biphasic model of cartilage is given by Equation 1.1:

$$\sigma = -pI + \sigma_S \tag{1.1}$$

where: p is the fluid pressure, σ_S is the stress in the solid phase, and I is the linear transformation tensor.

The fluid phase is modeled using Darcy's law:

$$\vec{w} = -k \cdot \nabla p \tag{1.2}$$

where w is the volumetric flux (fluid phase velocity relative to the solid phase), k is the permeability which describes the ease with which the interstitial fluid flows through the porous matrix and ∇p is the spatial gradient of pressure.

The permeability can be modeled as constant, independent of the tissue deformation, or strain-dependent where tissue permeability decreases with increased

strain. Lai et al. (1981) proposed a nonlinear relation for strain-dependent permeability that has been often implemented in the form of:

$$k = k_0 e^{M\varepsilon} \tag{1.3}$$

where k_0 is the permeability of the un-deformed tissue, ε is the strain, and M is the parameter that describes the strain dependence. Thus for compressive strains, $\varepsilon < 0$ and the permeability decreases.

As a biphasic mixture, the equations that govern the system are the law of conservation of mass (1.4) and the conservation of momentum (1.5).

$$\text{div}\,(v^s + w) = 0 \tag{1.4}$$

$$\text{div}\,\sigma = 0 \tag{1.5}$$

where v^s is the velocity of the solid phase which is related to the displacement u by $v^s = du/dt$. Note that Equations (1.4) and (1.5) couple the solid and fluid equations producing partial differential equations that can be solved for the unknowns p and u (Mow et al., 1980; Ateshian, 2009).

Fibril Reinforced Models

Although the isotropic biphasic models can capture the time dependent response of the articular cartilage, they fail to describe the tension-compression nonlinearity imparted by the collagen fibrils. Furthermore, the biphasic models could not describe the articular cartilage time dependent behavior in the short term when the cartilage is subjected to high strain-rate compression (Mow et al., 1990; Laasanen et al., 2003). Therefore, the biphasic theory was later extended by developing

fibril-reinforced models of the articular cartilage (Argoubi and Shirazi-Adl, 1996; Soulhat et al., 1999). In these models, the solid phase of the tissue is divided into a ground matrix that represents proteoglycans and fibril part that mimics the collagen fibrils network. The fibril components are modeled such that they support tensile forces only. Therefore, the solid matrix stress σ_S in Equation 1.1 is divided into non-fibrillar matrix stress σ_{nf} and fibril network stress σ_f as shown in Equation 1.6 (Soulhat et al., 1999).

$$\sigma_S = \sigma_f + \sigma_{nf} \tag{1.6}$$

In the literature, two types of fibril-reinforced models were extensively used, spring-based models and continuum fibril reinforced models (Julkunen et al., 2013; Wilson et al., 2005). In the spring-based type, the collagen fibrils were mimicked by linear spring between the nodes of the element in the element direction, see Figure 1.9. Spring-based type of fibril reinforced models were quickly improved to account for strain-dependent stiffness as given by equations 1.7 and 1.8.

$$E_f = E_f^0 + E_f^\varepsilon \varepsilon_f, \quad for \ \ \varepsilon_f > 0, \tag{1.7}$$

$$E_f = 0, \quad for \ \ \varepsilon_f \leq 0, \tag{1.8}$$

where, E_f^0 is the spring stiffness at the initial state, E_f^ε is the nonlinear spring stiffness and ε_f is the fibril strain. Since fibrils in spring-based models can sustain tension only, that was a great improvement over the transversely isotropic poroelastic models (Li et al., 1999, 2000).
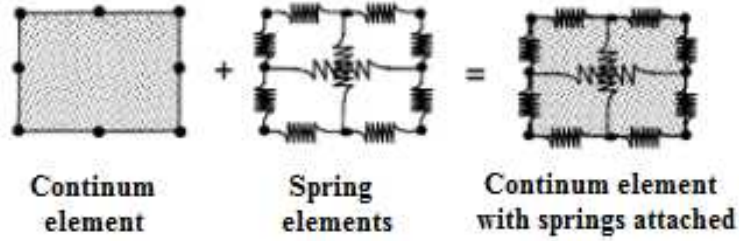
Figure 1.9: Spring elements in a porous continuum element.
   With permission from (Li et al., 1999).

Due to deformation incompatibility between fibril and non-fibril part of the spring-based fibril reinforced models, the continuum fibril models were later introduced (Li and Herzog, 2004). In these models, both the solid and the fiber parts of the solid phase were included in one continuum element. Therefore, a better representation of the collagen network can be achieved because the fibrils can run in any direction independent of the used mesh. The total fibril stress is calculated as the sum of the stress of each fibril (Wilson et al., 2005).

$$\sigma_f = \sum_{i=1}^{totf} \sigma_{f,all}^i, \tag{1.9}$$

1.4.2   Introduction To FEBio

Early finite element models of cartilage were commonly solved using the soil consolidation theory within ABAQUS (Dassault Systèmes, Waltham, MA, USA) (der Voet and Frank, 1992). Since soil consolidation analysis was not meant to solve biological tissues problems, researchers usually customize the program depending on their application with user-specified routines. This functionality allowed for modeling many complex problems of cartilage, (e.g. biphasic contact, fibers) (Federico et al., 2004; Pawaskar et al., 2007; Speirs et al., 2014).

In the last decade, FEBio, a freely available, implicit nonlinear finite element solver was developed specifically for biomechanical applications (Maas et al., 2012). FEBio supports transient quasi-static and dynamic analysis for deformable and rigid solids. It offers many isotropic hyper-elastic constitutive models as well as several transversely isotropic constitutive models that can be used to model many biological tissues such as cartilage, tendon, or ligament. The program also allows the user to compose more sophisticated material models (e.g. fibril reinforced model) by combining any number of built in models within the material library. FEBio also contains a rigid body constitutive model which is very useful for modeling structures whose deformation is negligible compared to the biological tissues (e.g. metallic indenter). FEBio was validated against two well established and verified FE codes, ABAQUS (Version 6.7, Simulia, Providence, RI) andNIKE3D(Ver-sion 3.4.1, Methods Development Group, Lawrence Livermore-National Laboratory, Livermore, CA)(Maker, 1995) or compared to analytical solutions. Also, many studies in the literature have produced identical results using FEBio and another FE codes (Meng et al., 2013, 2017; MacLeod et al., 2016).

FEBio consists of three separate software packages: PreView, FEBio solver, PostView, as well as the source code that are freely available to download for non-commercial use at http://febio.org/.

- **PreView** is a graphical user interface (GUI) that is used to create the input files of FE models. Pre-processing steps such as defining of material properties, prescribing the loads, and setting boundary conditions are performed in PreView. Mesh generation of some simplified geometries can be performed in Preview. However, PreView also allows for importing meshes from several other software packages (e.g., Gmsh, Abaqus, LSDYNA, Nike3D, etc.).

- **FEBio** is the finite element solver that solves the finite element equations based on an input file created in PreView. FEBio generates output files that can be visualized and analyzed in PostView.

- **PostView** is a GUI that visualizes and analyses the results.

In this thesis, unless specified otherwise, all FE models were solved using FEBio FEBio (Maas et al., 2012). Articular cartilage models were modeled as fibril reinforced biphasic material that is composed of a porous permeable solid matrix reinforced by fibrils and saturated with interstitial fluid using 8-node linear hexahedral shaped elements.

Hyper-elastic Neo-Hookean compressible material was selected for the ground matrix. it should be noted that the biphasic solid matrix is porous and the pores can lose or gain volume as fluid enters or leaves the matrix and hence compressible material is selected. Equation 1.10 describes the NeoHookean constitutive model (Maas et al., 2012, 2018):

$$\psi = \frac{\mu}{2}(I_1 - 3) - \mu \ln J + \frac{\lambda}{2}(\ln J)^2 \tag{1.10}$$

where ψ is the strain energy, I_1 is the first invariant of the Cauchy-Green deformation tensor, J is the determinant of the deformation gradient tensor, and μ and λ are the the Lame parameters from linear elasticity.

Inhomogeneous fiber distribution can be represented by the widely-used three-layered model where fibers are organized in three orthogonal directions X, Y and Z. This constitutive model displays mechanical behaviors similar to that of Conewise Linear Elasticity (CLE) model (Soltz and Ateshian, 2000).

The strain energy for each fiber bundle in the continuous fiber distribution constitutive model is described by a power law (Ateshian et al., 2009; Maas et al., 2018):

$$\psi_f = \frac{\xi}{\beta}(I_n - 1)^\beta, \quad \beta \geq 2, \quad I_n \geq 1 \tag{1.11}$$

where ψ_f is the fiber strain energy, ξ is the fiber modulus, I_n is the square of the fiber stretch, and β is a unitless material property.

At small strains and for $\beta = 2$, linear stress-strain relation can be considered and the tissue tensile stiffness reduces to:

$$H_{+A} \simeq 4\xi \tag{1.12}$$

For material parameters optimization, and to decrease the problem complexity, continuous fiber distribution (CFD) model that has been proven to predict many experimentally observed phenomena (Ateshian et al., 2009) was used. In continuous fiber distribution, an equal number of fibers or fiber bundles are oriented in all directions. This distribution is isotropic in the reference state and known as spherical fiber distribution. However, the combination of tensile-only behaviour, deformation, and material properties will result in anisotropic (or transversely isotropic) behaviour as soon as deformation occurs. The strain energy density function of the fibers is still given by Eq 1.11.

Specifying Fiber Orientation

In FEBio, to model materials that are transversely isotropic or orthotropic, or even inhomogeneous materials, ξ and β can be varied spatially. Therefore, specification of an initial fiber orientation is required. There are several ways to define the initial fiber orientation using a built in fiber generator. One way of specifying the fiber orientation is the use of spherical angles (azimuth and declination) relative to the local material axes or global coordinate system, as shown in Figure 1.10.
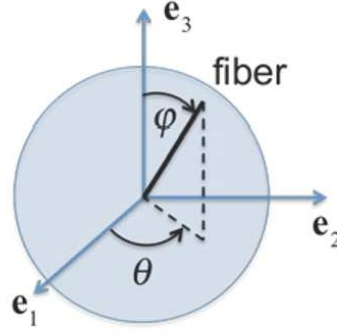
Figure 1.10: Specifying fiber orientation using spherical angles. Image from FEBio 2.5 User Manual.

Using angles θ and φ, the fiber is oriented along:

$$\sin\varphi\cos\theta e_1 + \sin\phi\sin\theta e_2 + \cos\varphi e_3, \qquad 0 \leq \theta < 2\pi, \ 0 \leq \varphi < \pi \qquad (1.13)$$

where (e_1, e_2, e_3) are orthonormal vectors representing the local element coordinate system (if specified), or global coordinate system.

Biphasic Contact

Among several contact implementations that are available in FEBio, the frictionless biphasic contact algorithm (sliding 2) is used to define the contact interface between the biphasic material and any other surface in finite element modeling in this thesis. The algorithm is implemented using the standard penalty method regularized with an augmented Lagrangian method (Ateshian et al., 2010). This algorithm enables the solver to smoothly accommodate finite deformation and sliding while enforcing the continuity of fluid flow and contact traction across the contact interface. In some cases where axisymmetric analysis is possible, a Tension-Compression Contact with large penalty factor is used between the symmetry plane and the angled back face of the tissue layer, see Appendix A.

1.5   The Pathology of Osteoarthritis

Osteoarthritis (OA) is a common disease that affects the biomechanical response of cartilage to loads, which can be studied experimentally and numerically with the models described above. OA affects the synovial joints and its major hallmark is the irreversible degradation of the articular cartilage. During osteoarthritis, degenerative changes to the articular cartilage are largely characterized by proteoglycan depletion and collagen fibrillation which leads to decreased cartilage stiffness and increased permeability and water content (Armstrong and Mow, 1982; Pearle et al., 2005; Sun et al., 2012). Osteoarthritis is strongly correlated with advanced age, obesity, joint abnormalities, and history of joint trauma. Hence, osteoarthritis has long been thought as degenerative condition that is caused by normal wear and tear process due to age-related high mechanical loads. However, decades of research have shown that osteoarthritis is a much more complicated disease and the chondrocytes may play a pivotal role in initiation and propagation of the disease process.

Chondrocytes comprise less than 5% of articular cartilage volume (Hu and Athanasiou, 2003); and they are responsible for the synthesis of the components that form the structurally well-organized ECM including the collagen fibrils and proteoglycans proteins. In healthy cartilage, the structural and functional integrity of ECM are maintained through a balance of anabolic and catabolic process. This function has long been believed to be greatly influenced by mechanical forces.

Hence, the chondrocyte response to mechanical stimuli has been a topic of an extensive research for decades. Different modes of mechanical loading have been applied to cartilage explants or to chondrocytes seeded in polymeric constructs, in

uniaxial (Quinn et al., 1998a; Buschmann et al., 1999) as well as biaxial compression (Smith et al., 1995; Frank et al., 2000; Di Federico et al., 2014). Whereas static compression has been proven to inhibit chondrocyte biosynthesis and induce cell death at high strains (e.g. 50%) (Guilak et al., 1994a; Sah et al., 1989), cyclic compression and dynamic shear were found to increase the synthesis of proteoglycan proteins (Kim et al., 1994; Buschmann et al., 1999; Fitzgerald et al., 2006). However, the synthesis of the collagen type II has always been lower in comparison (Bian et al., 2010).

Although these studies utilized a wide variety of loading modes, magnitudes, and frequencies, they have generally employed simplified loading protocols that result in a static contact area, i.e. unconfined compression, in which the compression tool covers the specimen surface during the entire test duration. This loading configuration does not reproduce the physiological loading conditions in the synovial joints where the contact location changes with joint motion. For example, the center of contact in the knee on both the femoral condyles and the tibial plateau shifts posteriorly with knee flexion angle (Boeth et al., 2013; Kaiser et al., 2017). In the hip joint, the orientation of the contact force varies throughout hip motions resulting in a migration of the center of contact pressure (Bergmann et al., 2001). Interestingly, tribological studies on cartilage have shown that migrating contact area or center of pressure are essential for sustained high interstitial fluid pressurization which promotes the low friction coefficient, 0.005-0.02 (Mow and Lai, 1980; Unsworth et al., 1975), during joint kinematics (Ateshian and Wang, 1995; Pawaskar et al., 2007; Caligaris and Ateshian, 2008; Bonnevie et al., 2011). In contrast, loading configurations with static contact area (e.g. dynamic unconfined compression) were proven to result in low fluid load support, over time, that was found to be insensitive to loading frequency (Krishnan et al., 2005). Moreover,

cyclic compression of articular cartilage was found to be associated with progressive tissue consolidation, i.e. increased ECM strains, which have an inhibitory influence on proteoglycan synthesis (Wong et al., 1999).

Furthermore, histological studies have shown that continuous passive motion (CPM) promoted the formation of healthy hyaline cartilage with strong anti-inflammatory properties (Knapik et al., 2013). CPM is a therapy frequently used following cartilage surgery to accelerate the healing process and promote the joint health. The interest in CPM was largely based on the principle that motion of the synovial joints enhances the cartilage metabolic activities, whereas prolonged immobilization was found to be detrimental (Salter et al., 1980). The biological mechanism of CPM enhancement of cartilage regeneration is still to be elucidated; however, it is widely accepted that fluid flow caused by joint motion provides the chondrocytes with the required nutrients and minerals and removes waste products (Maroudas, 1979). Interestingly, however, CPM yielded an outcome even superior to intermittent active motion (IAM) where a voluntary normal joint motion is restricted by pain only (Salter et al., 1980). Hence, the difference between CPM and IAM is in the amount of load transmitted through the joint. While CPM is performed at low constant contact force, the contact force in IAM is relatively high and differs over the cycle. For example, the contact force in the knee and hip joints during normal walking ranges from 25 - 250% BW (percent per body weight) (Bergmann et al., 2001; Damm et al., 2017).

The role of hydrostatic pressure in biosynthesis of matrix components was normally studied using isolated chondrocytes (Jortikka et al., 2000; Sauerland et al., 2003). These studies have shown that biosynthesis was increased by moderate cyclic hydrostatic pressure in the range of 0.5 - 5 MPa, whereas continuous high hydrostatic pressure (more than 15 MPa) decreased the biosynthesis. Moreover,

in a mechanobiological study conducted by Buschmann et al. (1999), unconfined cyclic compression resulted in an increased aggrecan synthesis at the radial peripheries of the cartilage explants, the region of high fluid flow. Hence, it could be reasonably hypothesized that joint motion/fluid flow is the dominant factor in the anabolism aspect of cartilage metabolism while the catabolism process could be mainly driven by contact forces/tissue deformation.

While these findings have confirmed the role of interstitial fluid flow in cartilage metabolism, it indirectly established the cartilage surface as the only free draining region that can ensure uniform tissue metabolism. Therefore, incorporating *in vitro* loading protocols that ensure fluid flow within the entire tissue and not only through the lateral boundaries would better reproduce the *in vivo* physiological condition as well as CPM condition. However, only a few *in vitro* studies have attempted to study cartilage mechanobiology under physiological loading conditions in which fluid flow is permitted through the entire cartilage surface (Correro-Shahgaldian et al., 2014; Schätti et al., 2015, 2016). Detailed discussion of these studies and the associated testing apparatuses is provided in Chapter 3.

Briefly, important aspects of the physiological conditions within the synovial joints such as strain level, stroke length, specimen source were ignored in those studies. For example, Correro-Shahgaldian et al. (2014) have investigated the effect of plowing on the biological response of cartilage using specimens harvested from bovine nasal septum (BNS) which is not a load-bearing cartilage. Also, Schätti et al. (2015, 2016) studied the effect of surface relative motion during sliding on the mechanobiology of cartilage using bovine condyles. However, the strain levels in these experiments were very high, 25% at the lowest and the sliding stroke length was also long $\pm$ 18 mm compared to physiological sliding distance in the knee joint (Monk et al., 2014).

Nevertheless, it is well documented that mechanical forces within the physiological range enhance chondrocytes metabolism and maintain cartilage integrity. On the other hand, non-physiological loading, whether joint overuse or disuse, can alter the metabolic response in chondrocytes and shift the balanced metabolism process toward catabolic activity triggering the degenerative process. Therefore, an important first step toward incorporating the physiological loading conditions in *in vitro* testing of cartilage biological response is defining those optimal loading conditions using certain mechanical parameters. Then, a mechanical testing approach can be developed and deeper analysis and understanding of interplay between cartilage physiological loading environment and chondrocytes metabolic activities can be achieved. The knowledge of chondrocytes response to physiological mechanical stimuli is vital for the development of tissue engineering approaches and therapeutic interventions for osteoarthritis.

1.6   Thesis Objectives

The main hypothesis of this thesis was that cartilage biomechanical and mechanobiological response to loading protocol that involves sliding with migrating contact area would be substantially different compared to uniaxial cyclic compression that is typically used in *in vitro* mechanobiological testing of cartilage. Therefore, the main objectives of this thesis are:

- To assess the fluid pressure, fluid flux, and tissue strains in articular cartilage model under sliding contact using finite element analysis and compare the results to uni-axial cyclic compression, the typical loading mode for *in vitro* mechanobiological testing of articular cartilage.

- To examine the effects of specimen surface curvature on cartilage biomechan-
  ical response under unconfined uni-axial cyclic compression.

- To design and construct a custom-made, load-controlled, testing device that
  is capable of reproducing the compression and sliding effects that the articu-
  lar cartilage is subjected to during normal activities of the synovial joints.

- To design and construct a custom-made, displacement-controlled, mechani-
  cal testing device to be used for uniaxial cyclic compression testing as well as
  cartilage thickness measurement by means of needle penetration test.

- Using the two loading devices, *in vitro* testing of cartilage will be performed
  in order to investigate the cartilage mechanobiological response under load-
  ing protocol that permits migrating contact area and compare the results to
  uniaxial cyclic compression.

1.7   Thesis Overview

Beside the introductory part, this thesis composes of four more parts:

In chapter 2, finite element analysis was performed to study the articular car-
tilage response to two different loading protocols, a sliding contact that promotes
migrating area of contact, and uni-axial unconfined cyclic compression, loading
configuration that is commonly utilized in mechanobiological testing of cartilage.
The effect of early osteoarthritic changes on cartilage biomechanical response un-
der both loading regimes was also investigated. In addition, the effect of the cur-
vature of the cartilage sample surface during unconfined cyclic compression was
also evaluated.

Chapter 3 presents the design and construction of two low-cost custom-made testing devices that are specifically made for biomechanical and mechanobiological *in vitro* testing of articular cartilage. The first is a load-controlled device that allows for static loading and sliding at the surface of articular cartilage. The second is a displacement-controlled device that was specifically made to be utilized for typical uni-axial cyclic compression of cartilage as well as for cartilage thickness measurement. The chapter starts with a literature review of *in vitro* testing devices used for mechano-biology experimentation of cartilage with a special focus on the most recent loading apparatus that used sliding contact. Then, it provides detailed description of both apparatus design and construction process.

Chapter 4, is designated for devices assessment and validation. Devices were used to estimate cartilage material properties from creep test. The fluid load support at the cartilage surface was assessed from sliding contact test. This chapter also includes finite element assessment of the fluid pressure and tissue recovery during sliding using specimen-specific FE models.

In chapter 5, mechanobiological *in vitro* testing of cartilage explants is carried out to study the effect of sliding contact proposed in Chapter 2 on cartilage metabolism. For the purpose of comparison, the experiment also considered the uni-axial cyclic compression loading protocol which is the most commonly used loading regime in cartilage mechanobiology.

Chapter 6, summarizes the overall conclusions of this work, contribution to area of research, and the planned future work.

Chapter 2

AC Biomechanical Response to Loads: FE Study

2.1 Introduction

As mentioned earlier, physiological loading conditions of the synovial joint are vital for promoting low friction at the articulaing surfaces and preserving the cartilage health. Physiological loading conditions involve the relative motion of the bearing surfaces which result in migrating the contact or center of pressure location (Bergmann et al., 2001; Boeth et al., 2013; Kaiser et al., 2017). Tribological studies have shown that the low friction coefficient is provided by high interstitial fluid pressurization that is sustained by migrating contact area (Ateshian and Wang, 1995; Pawaskar et al., 2007; Caligaris and Ateshian, 2008; Bonnevie et al., 2011). More recently, Moore and Burris (2017) have shown that sliding at physiological speeds could also provide tissue rehydration during stationary contact area or to non bearing regions of the tissue.

Although sliding motion was shown to be important in maintaining low friction, it is rarely considered in mechanobiological studies of cartilage. Physiological

loading conditions are also important for preserving the cartilage compositional and structural integrity. The chondrocytes that secrete the tissue components and maintain its structure and composition are highly responsive to their mechanical environment (Guilak, 2011). Hence, abnormal loading environment is expected to shift this function toward catabolic activities leading ultimately to chronic joint disease such as osteoarthritis (Grodzinsky et al., 2000; Julkunen et al., 2013). The initiating events and patho-mechanism of osteoarthritis are not well understood; however, rough loading conditions (Andriacchi and Mündermann, 2006; Ganz et al., 2008; Guilak, 2011; Anderson et al., 2011) as well as reduced joint activity level (Haapala et al., 1999; Kiviranta et al., 1994) have been long linked to the initiation and progression of the disease. On the other hand, continuous passive motion therapy (CPM) was found to enhance the generation of healthy cartilage matrix (Salter et al., 1980). CPM is a therapy that involves moving the contact area at low normal force and commonly used following cartilage surgery (Knapik et al., 2013).

Therefore, the chondrocytes response to mechanical stimuli has been a topic for extensive research. However, previous loading protocols used in mechanobiological *in vitro* testing of cartilage generally used simplified loading regimes that involves static contact area. Unconfined cyclic uni-axial compression was the most commonly employed loading regime as it was believed to reproduce the loading and unloading events that occur *in vivo* (Kim et al., 1994; Buschmann et al., 1999). Uniaxial cyclic compression is normally preformed in unconfined compression configuration where the tissue is compressed by means of a metallic platen using a predefined strain level while the tissue is free to expand laterally as shown in Figure 2.1.
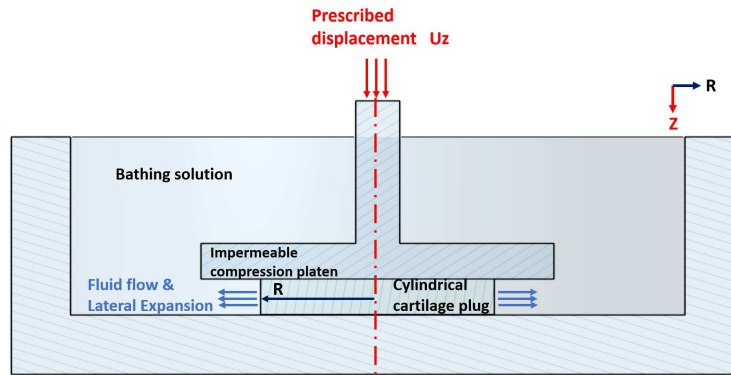
Figure 2.1: A sketch of the commonly used unconfined compression test applied to cylindrical articular cartilage disk.

During unconfined compression configurations, the compression platen is expected to cover the entire tissue surface, assuming a specimen with a flat surface and uniform thickness. However, this assumption is not always valid due the natural curvature of synovial joints. A common technique that has been used to work around that was the use of a small size specimen (e.g. 3 mm in diameter) at which the effect of surface curvature was assumed negligible. Moreover, in many studies, the top and/or the bottom layer were sliced off using sliding microtomes until parallel surfaces are obtained (Patwari et al., 2003).

While this assumption could be appropriate for static unconfined compression which is commonly used to estimate the material properties of cartilage zones separately, it many not be the case in mechanobiological testing where the chondrocytes from different depth layers are adapted to different mechanical environments. Furthermore, unconfined cyclic compression test is normally performed using displacement-controlled devices where the applied level of strain remains constant. However, synovial joints are subjected to cyclic loading in which the load amplitude depends on the activity and body weight of the person (Bergmann et al., 2001). Thus, *in vivo* the strain is a response to an applied load, and depends

on the material properties. In this load-controlled loading mode, most of the applied load is carried by high interstitial fluid pressure which has been shown to be maintained during daily activities by the relative motion of the articulating surfaces, e.g. sliding/rolling (Ateshian and Wang, 1995; Pawaskar et al., 2007; Caligaris and Ateshian, 2008; Bonnevie et al., 2011).

Therefore, an important first step for understanding the chondrocytes *in vivo* mechano-regulation would be to reproduce the relative surface motion that occurs during normal function of synovial joints, especially the high fluid load support and the associated fluid flow and tissue strains. Hence, using finite element analysis, the goal of this study is first to assess the fluid pressure, fluid flow, and tissue strains under sliding loading mode and compare the results to uniaxial cyclic compression; the typical loading protocol used in *in vitro* mechanobiological testing of cartilage. Second, to study the possible effect of cartilage surface curvature on the tissue behavior during cyclic compression. It was hypothesized that sliding that promotes a migrating contact area, will maintain lower tissue consolidation and constant fluid flow compared to uniaxial cyclic loading. The effect of simulated degenerative changes on cartilage biomechanics under both loading regimes will also be investigated by analyzing the resultant fluid pressure, fluid flow, and tissue strains compared to healthy cartilage models.

2.2 Method

Finite element models of cartilage were created with geometry within the range of the commonly used *in vitro* cartilage loading experiments. In the first model, uniaxial unconfined cyclic compression was simulated using a perfectly flat cartilage disk of 3 mm diameter and thickness of 2.0 mm (Ateshian et al., 1991). This disk

size is typically used in unconfined compression testing (Fitzgerald et al., 2006; Li et al., 2013). For the sliding model, a rigid impermeable spherical indenter of diameter 4.75 mm was made to slide over a flat cartilage disk that is 10 mm in diameter (Accardi et al., 2011; Bonnevie et al., 2011). To study the effect of surface curvature on cartilage biomechanical response during *in vitro* testing, similar models with convex shaped surface were employed to simulate samples with curved surface. The surface curvature radius was taken to be 25 mm. This value is within the range of humeral and femoral head radii (Milner and Boldsen, 2012; Monk et al., 2014). The analysis was run using the freely available finite element code, FEBio (Maas et al., 2012).

2.2.1 Model Geometry and Mesh

The cartilage models were created and meshed using freely available 3-D finite element mesh generator (Gmsh) (Geuzaine and Remacle, 2009) and then imported into a pre-processing software Preview (Maas et al., 2012) where the material properties, loads, and boundary conditions were prescribed. The mesh was biased in both axial and lateral directions to capture the rapid change in fluid pressure and displacement and to minimize the number of elements for computational efficiency. Mesh sensitivity analysis was performed to ensure there would be less than 5% change in the predicted fluid and contact pressure between the last two consecutive models. The mesh sensitivity analysis is presented in Appendix A. Due to rotational symmetry, 1° wedge model was used for the unconfined cyclic compression models whereas half of the model was considered for sliding contact analysis as shown in Figure 2.2. The final cartilage sliding contact model consisted of a total of 56160 linear hexahedral 8-node elements and 1440 linear pentahedral

6-nodes elements. The $1°$ cyclic compression model consisted of 1080 linear hexa-hedral 8-node elements and 45 linear pentahedral 6-nodes elements. Pentahedral elements are known to be stiffer than hexahedral elements which may affect the ac-curacy of the model. However, the biased mesh in the lateral dimension reduced the size of pentahedral elements at the center of the sample; and hence, the effect on the overall model accuracy.
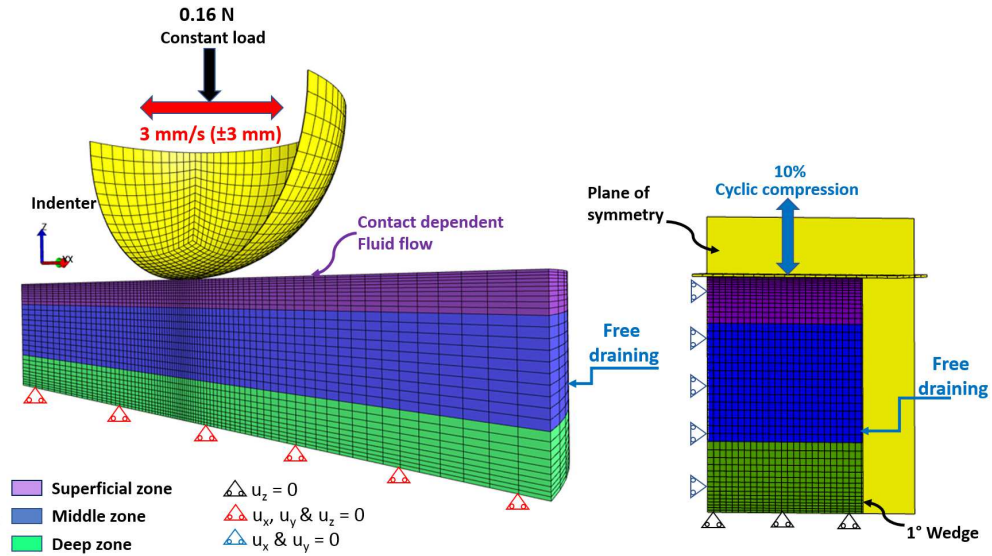
Figure 2.2: Symmetric 3-D model and boundary conditions of cartilage under sliding contact (Left) and uni-axial cyclic compression (Right).

2.2.2 Material Properties

Articular cartilage exhibits depth-dependent structure and composition which re-sults in depth-dependent material properties (Wilson et al., 2007; Shirazi et al., 2008). However, for simplification, this study considered only the in-homogeneity of the collagen fibers which is believed to have a great effect on the fluid pressure (Meng et al., 2017). Hence, the cartilage was modeled as fibril reinforced biphasic material using the well-known three layers structure where the superficial zone

(SZ), middle zone (MZ), and the deep zone (DZ) represented 20%, 50%, and 30% of the tissue thickness, respectively (Mow et al., 1992). This model produced fluid pressure distribution that was very close to FE model that used realistic collagen fiber orientation (Meng et al., 2017).

The ground matrix that mimics proteoglycan network was modeled as a neo-Hookean hyper-elastic solid which is governed by the equilibrium compressive modulus (H_{-A}) and Poisson's ratio (ν). The interstitial fluid transport was modeled using constant and isotropic hydraulic permeability since the applied and expected strains are relatively low ($\leq 10\%$), thus change in permeability is negligible (Buschmann et al., 1997; Reynaud and Quinn, 2006). The fluid fraction was taken to be 80%; however, the used constitutive model of permeability (isotropic and constant permeability) is independent of porosity. Material properties for the ground matrix and permeability for bovine cartilage were adapted from Athanasiou et al. (1991). Although permeability depends in part on tissue porosity, the implementation of the fluid phase in FEBio does not require porosity to be defined explicitly.

The collagen fibril network was simulated using transversely isotropic three tensile-only orthogonal bundles of fibers (Ateshian et al., 2009). The fiber modulus (ξ) in the unstrained condition was calculated from $H_{+A} = 4\xi$, where H_{+A} is the cartilage tensile stiffness. The tensile stiffness for MZ and DZ were taken to be 50% and 33%, respectively, of the SZ (Verteramo and Seedhom, 2004; Chegini and Ferguson, 2010; Meng et al., 2017). Material properties for bovine articular cartilage are given in Table 2.1. The compression platen and the plane of symmetry in the unconfined cyclic compression models as well as the indenter in the sliding contact models were all considered as rigid.

Table 2.1: Material properties of bovine articular cartilage with zonal and directional dependent tensile stiffness.

Layer	H_{+A} (MPa)	H_{-A} (MPa)	ν	k $(mm^4/N.s)$
SZ	x, y = 6			
	z = 2			
MZ	x, y, z = 3	0.47	0.24	0.0014
DZ	x, y = 2			
	z = 6			

Degenerative changes that occur in articular cartilage during osteoarthritis are largely characterized by proteoglycan depletion and collagen fibrillation which leads to decreased cartilage stiffness and increased permeability and water content (Armstrong and Mow, 1982; Pearle et al., 2005; Sun et al., 2012). Hence, cartilage material properties were altered to simulate the degenerative changes that occur in early stages of osteoarthritis. Equilibrium compressive modulus (H_{-A}) was reduced by 15% to simulate proteoglycan depletion while the permeability (k) was increased by 20% (Armstrong and Mow, 1982). It is believed that collagen fibrillation during early stages of osteoarthritis occurs mainly in the superficial zone. Therefore, collagen fibrillation was simulated by decreasing the fiber stiffness of the superficial zone by 50% (Mononen et al., 2011; Speirs et al., 2014).

2.2.3   Loads and BCs

In uniaxial cyclic compression models, the bottom side was assumed impermeable and allowed to expand laterally. 10% strain was prescribed to the top surface of the tissue by axially displacing the compression platen using haver-sine waveform (0.5 Hz, 40% duty cycle) (Li et al., 2013). A free draining condition was imposed at the lateral periphery and contact dependent flow condition was used at the tissue

surface. That was needed to allow for free fluid flow from surface regions that is not in contact with the compression platen in the case of curved surface model. For sliding contact model, the bottom side of the cartilage sample was fixed in all directions and no fluid flow was permitted out of this side to mimic the fixation of the cartilage to the impermeable subchondral bone. A free draining condition was imposed on the other boundaries that are not in contact with the indenter and no flow was permitted across the plane of symmetry. A frictionless biphasic contact, sliding-2 in FEBio, which accounts for sliding and large deformation was used for the indenter-cartilage interface (Ateshian et al., 2010).

Depending on type of activity, the load transmitted across the synovial joints could be several times of body weight (Bergmann et al., 2001) and the contact pressure could reach as high as 18 MPa (Hodge et al., 1989). Under moderate activities, such as normal walking, the contact pressure ranges from 1 to 6 MPa (Hodge et al., 1989; Park et al., 2004; Shirazi et al., 2008). However, in this study and for the assumption of low strain to be valid, the contact pressure was kept at the low end of physiological values, below 0.5 MPa (Wang et al., 2017). Hence, in a preliminary step, a vertical load of 0.16 N was applied to the indenter over a ramp time of 2 s.

Axial indentation testing suggested that the indentation effects are negligible at distance that is four times the contact width or more (Spilker et al., 1992). Hence, given the initial contact depth produced by this load and the sample diameter, the maximum stroke length is 3 mm. Therefore, a reciprocating sliding motion of $\pm$ 3 mm was applied to the indenter while the vertical load was kept constant. The simulation was run at a constant sliding speed of 3 mm/s.

Since the loading modes used in this study were very different (load-controlled mobile indentations compared to displacement-controlled unconfined cyclic compression), and for comparison justifications, a load-controlled cyclic indentation

at the center of the specimen was also performed. The load was applied to the indenter using haver-sine waveform (0.5 *Hz*, 40% duty cycle). The resultant total strain and maximum fluid pressure at the specimen center were compared to sliding contact model.

In all models, the simulation was run for 120 *s*. The articular cartilage biomechanical response to the different loading modes was investigated by analyzing the resulting spatial strains and fluid pressure distribution. Results were predicted in the middle of deep and superficial zones at the sample center and at distance of 60% of the specimen radius away from the center (0.6 *r*), which is the end of the sliding stroke in the sliding contact model.

2.2.4 Output Variables

Previous studies have shown that biological signaling response of chondrocytes is associated with tissue deformation (Sah et al., 1989; Kim et al., 1994; Urban, 2000) and fluid hydrostatic pressurization (Smith et al., 1996; Jortikka et al., 2000). Therefore, the resultant fluid pressure and the tissue strains under both types of loading were in the focus of this comparison.

2.3 Results

Results from comparisons of cyclic indentation to sliding (i.e. mobile indentation) are illustrated in Figure 2.3. Gradual reduction in fluid pressure was predicted by cyclic indentation model which resulted in maximum fluid pressure that was 40% lower than what was predicted during sliding. Similarly, tissue strain increased by 11% during cyclic indentation compared to 3.2% increase under sliding.
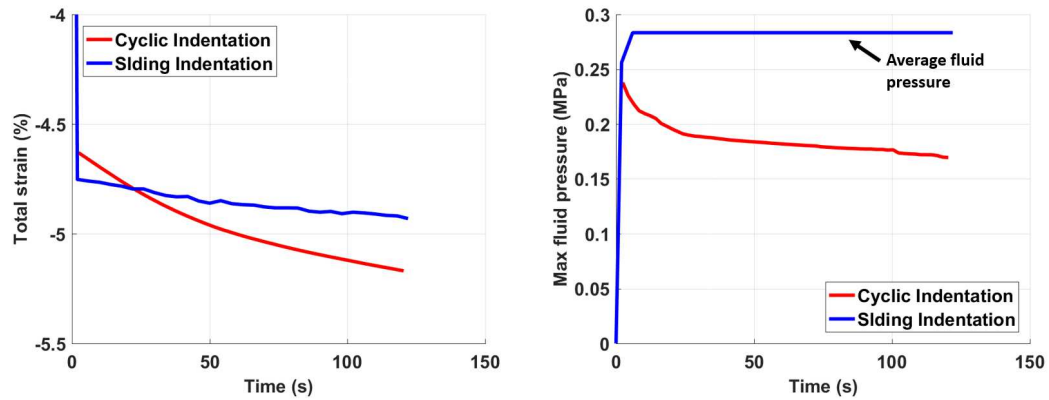
Figure 2.3: Total strain and maximum fluid pressure predicted at the specimen center during cyclic and sliding indentation. Maximum fluid pressure during sliding was a little noisy ranging (0.274 - 0.295 MPa), hence it was averaged at 0.283 MPa.

2.3.1 Uni-axial Cyclic Compression vs Sliding Contact

The general behavior of healthy articular cartilage under sliding loading and uni-axial cyclic compression is illustrated in Figure 2.4. Since cyclic compression was performed under displacement-controlled mode and sliding under load-controlled mode, the tissue response was compared by plotting the change in reaction force and total strain, respectively, over the same period of time.
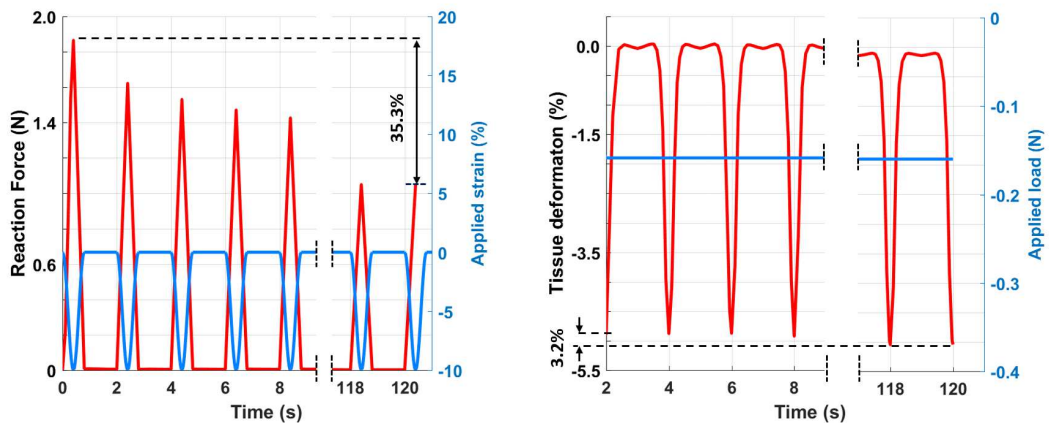
Figure 2.4: The mechanical response of cartilage (red graphs) to displacement-controlled uniaxial cyclic compression (left) and load-controlled sliding (right).

In the sliding contact model, tissue deformation caused by the prescribed load resulted in a fluid pressure in the superficial zone that was 65% higher than what was predicted in the deep zone, see Figure 2.5. Similarly, transverse and axial strains were higher, by 32% and 35% respectively, in the superficial zone compared to deep zone as shown in Figures 2.6 and 2.7. Slightly higher fluid pressure and lower tissue strains were predicted near the lateral peripheries compared to the sample center in the same zone; however, they remained constant throughout the simulation time.
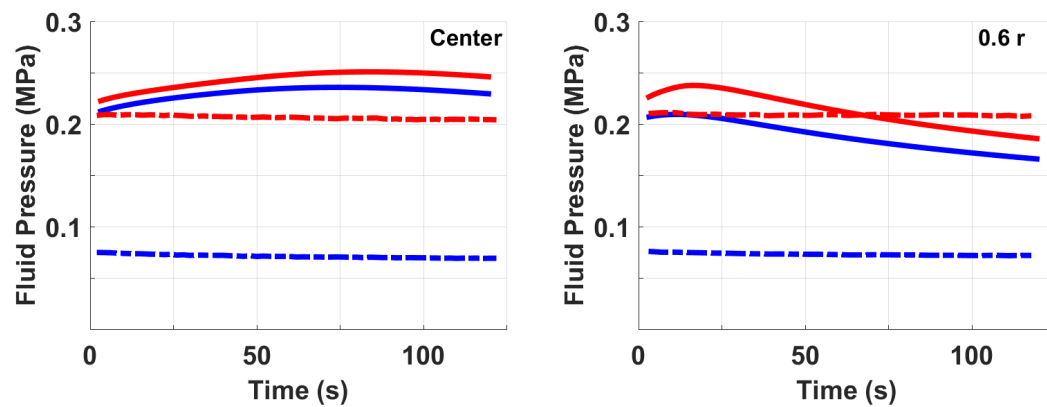
Figure 2.5: Per cycle, peak of the fluid pressure predicted at the center of sample (Left) and at 0.6 r (Right). SZ (Red) and DZ (Blue) from sliding contact model (dashed lines) and cyclic compression model (solid lines).

On the other hand, uniaxial cyclic compression predicted fluid pressure that is nearly uniform through the depth, although slightly higher in the superficial zone, by nearly 5%. The predicted transverse and axial strains were higher, by 54% and 49% respectively, in the deep zone compared to superficial zone. Near the lateral peripheries, the fluid pressure and transverse strain showed fast reduction over time, see Figures 2.5 and 2.6.
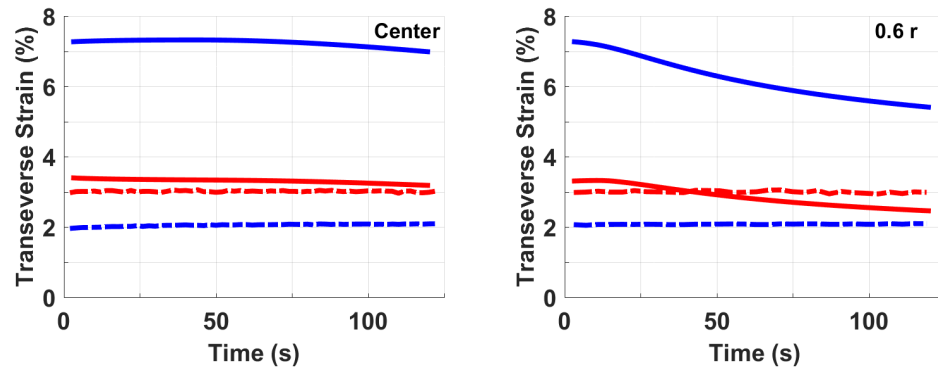
Figure 2.6: Per cycle, peak of the transverse strain predicted at the center of sample (Left) and at 0.6 r (Right). SZ (Red) and DZ (Blue) from sliding contact model (dashed lines) and cyclic compression model (solid lines).

By the end of simulation time, the fluid pressure and transverse strain were reduced by 19% and 26%, respectively. On the contrary, the axial strain remained constant in the deep zone; however, it slowly increased in the superficial zone, to reach 13% higher by the end of simulation, Figure 2.7. Through the depth, cyclic compression showed nearly uniform fluid pressure where the tissue strains were increasing through the depth. On the contrary, fluid pressure and tissue strains predicted by sliding model were highest in the superficial zone and decreased in depth-dependent manner.
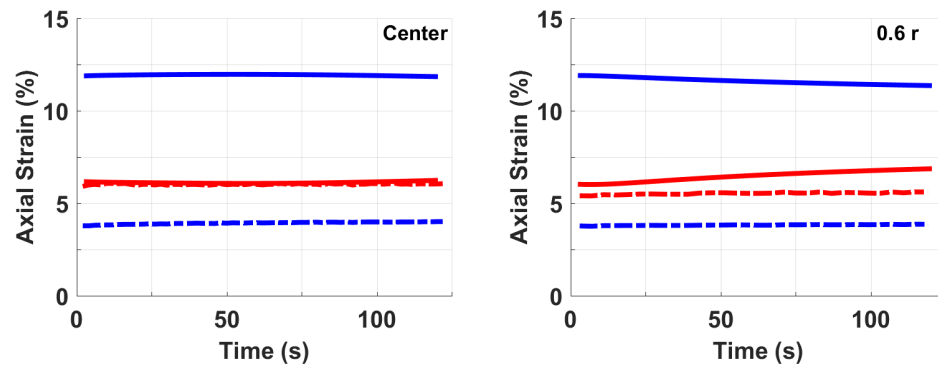
Figure 2.7: Per cycle, peak of the axial strain predicted at the center of sample (Left) and at 0.6 r (Right). SZ (Red) and DZ (Blue) from sliding contact model (dashed lines) and cyclic compression model (solid lines).

Figure 2.8 illustrates the peak of the fluid pressure and transverse strain predicted at the end of simulation at a line that passes through tissue thickness at the center and at 0.6 r distance from the sample center. Note that in sliding model, data was collected at the time when the indenter at the center and at the end of the stroke length (i.e. data was always collected at the center of contact). The normalized tissue depth is measured from the surface (0.0) to the tidemark (1.0).
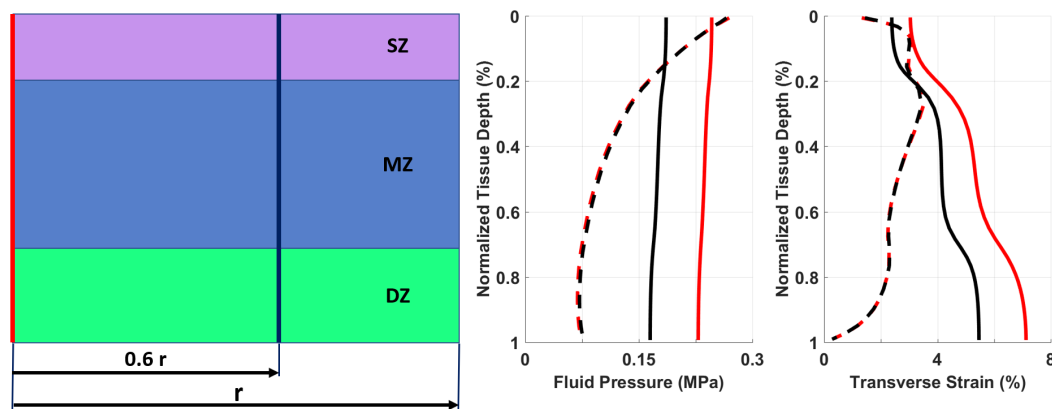
Figure 2.8: Last cycle, peak of fluid pressure and transverse strain predicted through the depth at two locations: The center of the sample (red) and at distance 0.6 r (black), sliding model (dashed lines) and uniaxial loading (solid line).

2.3.2 Healthy vs Degenerated Cartilage

In sliding model, OA changes caused reduction in the fluid pressure by 13.5% in the superficial zone while there was nearly no change in the deep zone. Similarly, transverse strain increased by 48.8% and axial strain increased by 38%. In the deep zone, transverse strain increased by 3.9% and and axial strain increased by 4.3%.
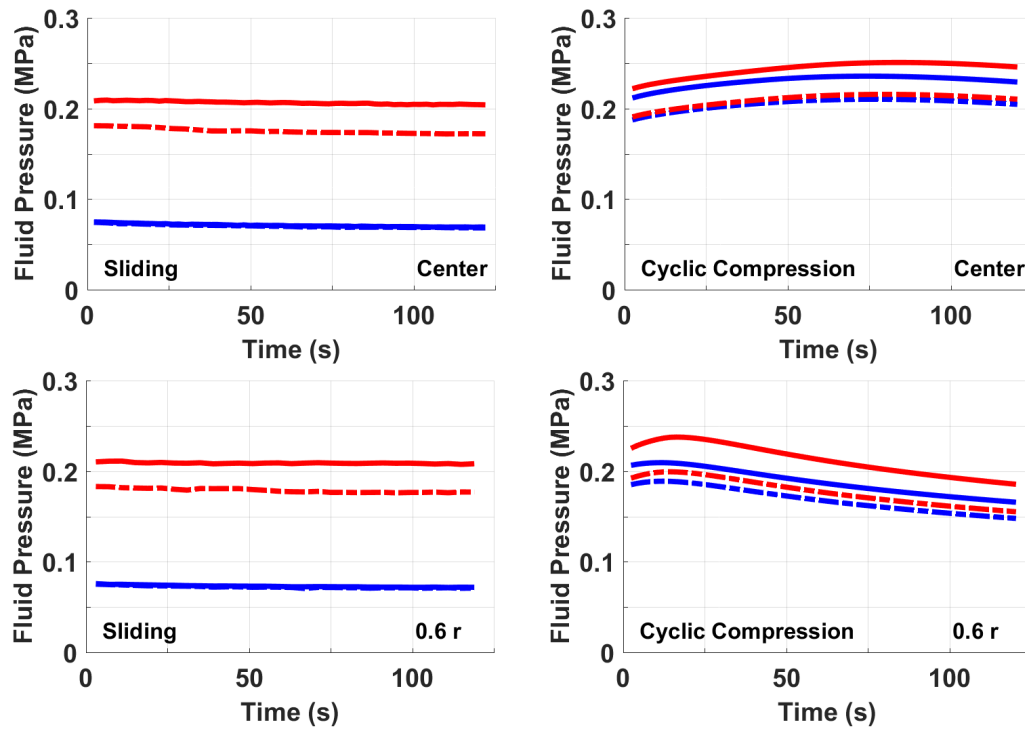
Figure 2.9: Per cycle, peak of the fluid pressure predicted at two locations in the SZ (Red) and DZ (Blue). Healthy cartilage (Solid lines) and degenerated cartilage (Dashed lines).

In cyclic compression model, at the center of the sample, OA changes caused reduction in the fluid pressure was by 14% while transverse and axial strains increased by 42.6% and 50.5%, in the superficial zone, respectively. In the deep zone, fluid pressure was also reduced by nearly 11% while transverse and axial strains were reduced by 8.35% and 7.0%, respectively. Near the radial periphery of the sample, the fluid pressure was reduced by 16% while transverse strain and axial strain increased by 52.0% and 37.4%, in the superficial zone, respectively. In the deep zone, fluid pressure was reduced by 10%, transverse strain and axial strain were also reduced by 7.4% and 5.7%, respectively.
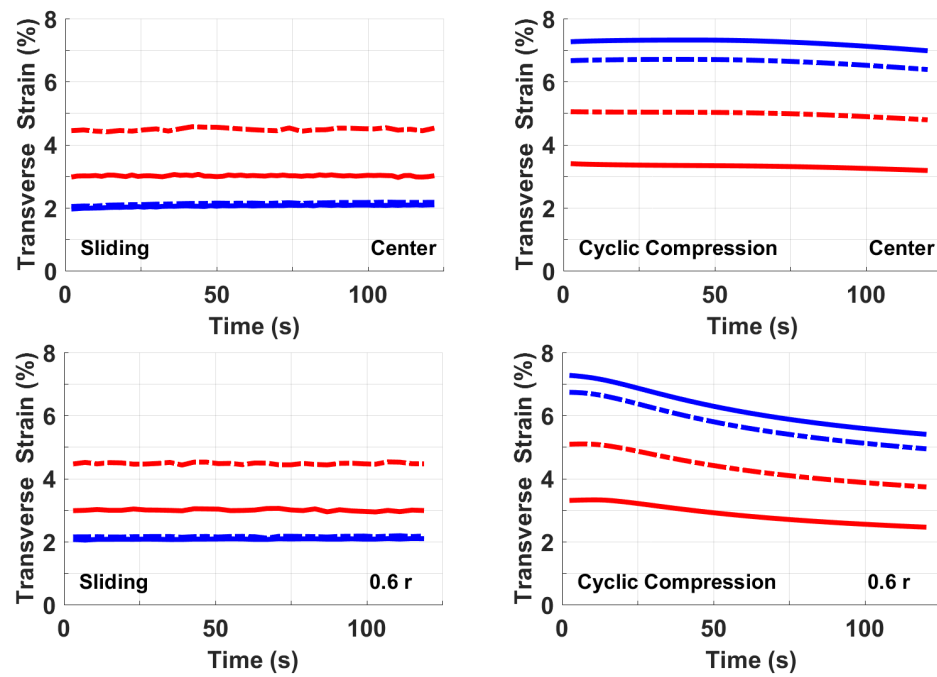
Figure 2.10: Per cycle, peak of the transverse strain at two locations in the SZ (Red) and DZ (Blue). Healthy cartilage (Solid lines) and degenerated cartilage (Dashed lines).
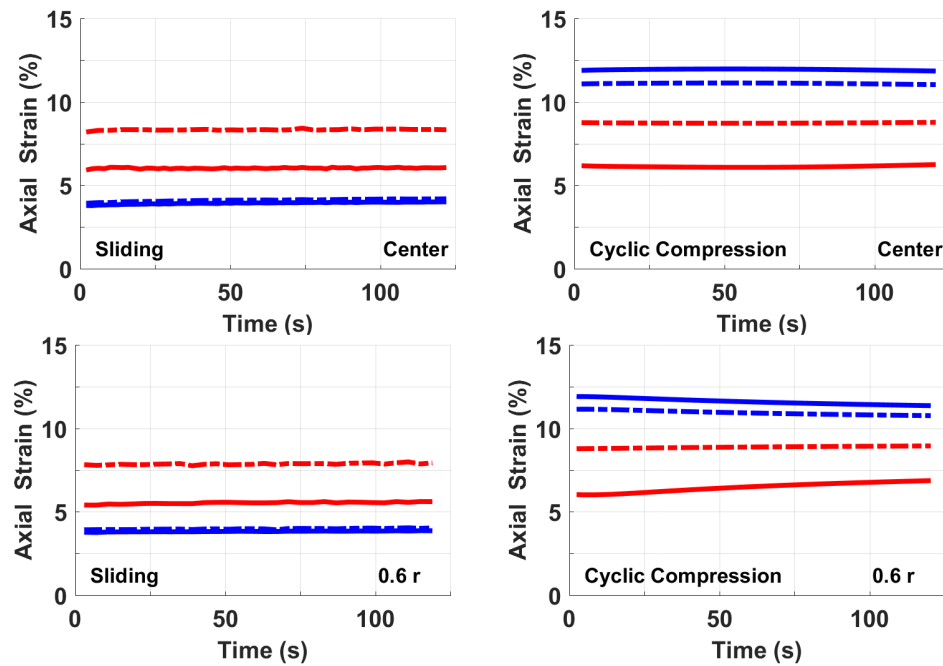
Figure 2.11: Per cycle, peak of the axial strain at two locations in the SZ (Red) and DZ (Blue). Healthy cartilage (Solid lines) and degenerated cartilage (Dashed lines).

2.3.3 Flat vs Curved Surface

As can be seen in Figure 2.12, the predicted fluid pressure in the deep zone was 10% higher in the curved model compared to flat models, near the radial periphery. Similarly, transverse and axial strains were 12% and 7.4%, higher in flat model than curved model in the deep zone, respectively. Minimal difference in tissue strains was predicted at the sample center, see Figure 2.13.
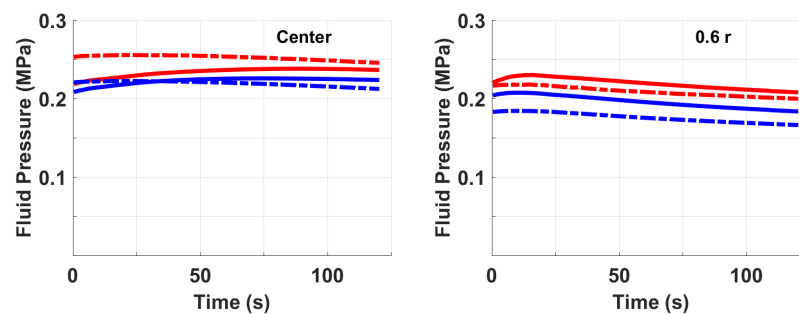
Figure 2.12: Per cycle, peak of the fluid pressure predicted by curved surface model (dashed lines) and flat surface model (solid lines). SZ (Red) and DZ (Blue).
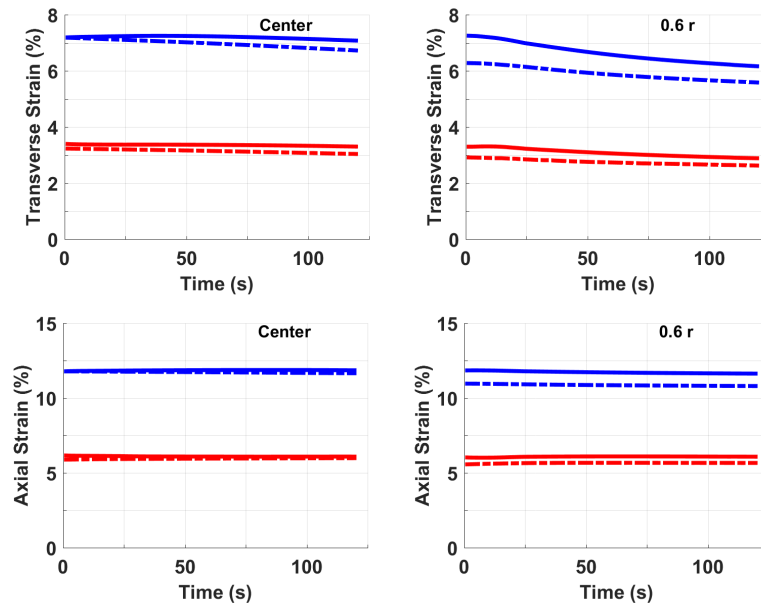
Figure 2.13: Per cycle, peak of the transverse and axial strains predicted by curved surface model (dashed lines) and flat surface model (solid lines). SZ (Red) and DZ (Blue).

2.4   Discussion

The results obtained from cyclic indentation are clearly showing that the differences in tissues response mainly caused by sliding and migrating contact area that maintained balanced fluid imbibition-exudation. while sliding caused increase in fluid pressure by 10% after the fist sliding cycle which was maintained for the rest of simulation, cyclic indentation resulted in gradual reduction in fluid pressure which ended 36% lower than the first cycle. Reduction in fluid pressure resulted in increased tissues strain in a trend that is similar to unconfined cyclic compression. Hence it can be concluded that the difference in tissues response between sliding contact and unconfined cyclic compression is greatly influenced by the tissue retardation maintained by migrating contact area.

However, number of limitations should be noted in this study. First limitation was related to models' geometries. Specimen size used in each model were different (diameter of 10 mm and 3 mm). The smaller diameter size, 3 mm, was commonly used in uni-axial mechanobiological testing of cartilage and hence was selected (Fitzgerald et al., 2006; Li et al., 2013). On the other hand, sliding required larger specimen size. Also, due to restrictions of the specimen size that can be used in in vitro testing, the indenter size that was used is much smaller than actual joint size (Milner and Boldsen, 2012; Monk et al., 2014). Second, the sliding speed used in this study was relatively low compared to physiological sliding speed in hip or knee joints (Fisher et al., 1994; Neu et al., 2008). Modeling high sliding speed is complex and often leads to solver errors such as collapsed elements. However, previous tribological studies have shown that interstitial fluid pressurization during sliding positively correlates with the sliding speeds (Bonnevie et al., 2011; Moore and Burris, 2014). Further, preliminary models, in this study, have shown that

fluid load support increased while tissue strain decreased when the sliding speed increased from 1 to 3 mm/s. Hence, it can be reasonably assumed that the difference in cartilage response to both types of loading will be more obvious at high sliding speeds.

Moreover, although this study considered the depth dependent orientation of collagen fibrils, a more accurate representation of cartilage would be the inclusion of depth-dependent properties of the solid matrix (Schinagl et al., 1997; Shirazi et al., 2008) which was found to further increase the fluid pressure near the cartilage surface (Krishnan et al., 2003) . Moreover, the cartilage permeability is known to be strain-dependent (Holmes and Mow, 1990) and depth-dependent (Federico and Herzog, 2008b). Since the focus of this study was to highlight the importance of the loading protocol in tissue mechanobiological functions, the above-mentioned factors were not considered.

Nevertheless, the results strongly suggest that implementing physiological loading protocols in *in vitro* testing may influence the mechanobiological response of articular cartilage. The state of the fluid pressure, fluid flow, and tissue strain predicted during sliding configuration that promotes migrating contact area were substantially different from those predicted under uni-axial cyclic compression, the typical loading mode in mechanobiological *in vitro* testing of cartilage explants. Moreover, using a small specimen size (e.g. D = 3 mm) does not completely alleviate the effect of surface curvature on cartilage biomechanical response. Further, results showed that joint curvature could be contributing to the fluid load support during stationary contact area.

Uni-axial Cyclic Compression vs Sliding

Sliding contact maintained constant interstitial fluid pressurization and tissue strains throughout the simulation by continuous tissue rehydration. As the indenter moves to a new location, the previously loaded location begins to recover its initial thickness driven mainly by tissue elasticity and fluid imbibition. This explains the higher fluid pressure and lower axial strain predicted near the radial periphery, as this region has longer recovery time compared to the sample center as shown in Figures 2.5 and 2.7.

These observations are important since cyclic cell stretching, compression as well as cyclic fluid pressurization and fluid flow are possible mechanobiological mechanisms in cartilage biosynthesis. Therefore, altered tissue deformation and fluid pressurization under sliding contact, compared to uniaxial cyclic loading configuration, may provide new insight into mechanobiological processes *in vivo*. Previous *in vitro* experiments on chondrocyte response to mechanical stimuli have demonstrated an increase in proteoglycan and protein synthesis in dynamic unconfined compression, depending on loading frequency and magnitude. However, as shown in this study, these loading protocols do not reproduce the pressure or strain distribution within cartilage under physiological sliding loads. Stimulation of PG synthesis has been reported to occur in the region of high fluid flow rate, i.e. greater than 0.25 $\mu m/s$, which occurs mainly at the radial periphery of the cartilage explants in dynamic unconfined compression (Buschmann et al., 1999). Although this study used intermittent loading, 40% duty cycle, with larger strain amplitude compared to the study of Buschmann et al. (1999), the maximum fluid flux at the radial periphery was decreased by 44% by the end of simulation which lasted only for 2 minutes. This consolidation rate is extremely high and could lead to a large reduction in the fluid flow and pressure after short period of time. The

loading period in *in vitro* mechanobiological testing of cartilage is typically long, ranging from 1 to 23 hours (Kim et al., 1994; Buschmann et al., 1999; Fitzgerald et al., 2006; Li et al., 2013), which suggests that the physiological pore pressure and the flow rate required for maintaining cartilage metabolism could be absent most of the time during a cyclic compression test. Hence, the PG synthesis process could be greatly impaired as the *in vitro* unconfined cyclic compression testing progresses.

Interestingly, sliding resulted in fluid pressure that was highest at the superficial zone and decreased through the depth. The predicted tissue strains were also depth dependent (see Figure 2.8) in a way that may resemble the depth dependent metabolism (Aydelotte and Kuettner, 1988; Coates and Fisher, 2010). The combination of compression and shear during sliding resulted in compressive and tensile strains that are more significant in the lower portion of the superficial zone, the same region of higher fluid pressure. Interestingly, cartilage matrix is known to exhibit depth dependent structure and composition which is mainly due to variations in cellular activity (Coates and Fisher, 2010). Studies on isolated chondrocytes have also suggested that superficial zone cells may be stimulated by tensile strain (Vanderploeg et al., 2008) while deep zone cells were more responsive to compressive strain (Lee et al., 1998).

Furthermore, fluid flow is very important for magnifying diffusion of nutrients, biochemical signals and waste exchange in articular cartilage since the tissue lacks both a vascular network and direct access to the lymph system (Hu and Athanasiou, 2003). This study showed that fluid imbibition from the lateral peripheries, during the unloading portion of the cycle in unconfined cyclic compression, was not sufficient to reach the sample center. In fact, fluid continues to flow out of that region during the unloading cycle. That suggests that the

chondrocytes at the center of the sample can not be provided whith the required oxygen and nutrient supply in this loading mode. That may explains the PGs stimulation only near the lateral peripheries observed by Buschmann et al. (1999). On the other hand, migrating contact area permitted cyclic fluid flow from the entire tissue surface at constant rate. That resulted in high fluid flow within the superficial zone, decreasing through the depth. However, chondrocytes in the middle and deep zones are well adapted to low oxygen environment while the cells of the superficial zone are metabolically more active and require more oxygen and nutrient supply (Hu and Athanasiou, 2003).

Healthy vs degenerated cartilage

As it was expected, softened solid matrix and increased permeability, due to early osteoarthritic changes, resulted in reduction of the fluid pressure and increased tissue strains in both models. Unconfined cyclic compression model predicted reduction in fluid pressure that was uniform through the depth, although slightly higher in the superficial zone. However, the increase in local strains seen in the superficial zone was compensated by reduction in strains of the deep zone, see Figure 2.14 and Figure 2.15. That is due to the fixed amount of compressive strain applied in displacement-controlled mode. That is very important as it questions the feasibility of using displacement-controlled configurations in *in vitro* testing of cartilage, especially in unconfined compression.

It is well documented that *in vivo* cartilage degradation during OA starts from the superficial zone and propagates through the depth as the disease progresses (Muir, 1978; Andriacchi et al., 2004; Madry et al., 2012). The initiation and propagation of OA has also been long linked to high stresses. Yet, as it can be seen in Figures 2.14 and 2.15, the chondrocytes in the lower zones, during unconfined
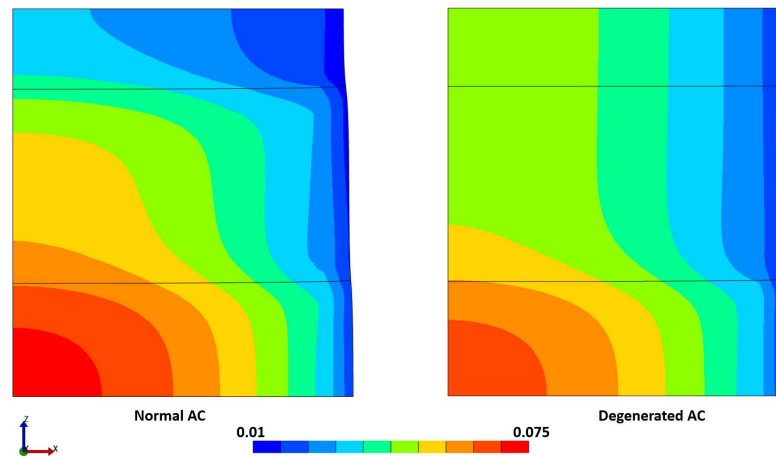
Figure 2.14: Peak of the transverse strain, predicted during the last cycle of cyclic compression, for normal cartilage (Left) and degenerated cartilage (Right)

cyclic compression, are subjected to higher transverse and axial strains compared to their counterparts in the superficial zone. Adding that to the uniform fluid pressure through the depth, OA changes are expected to start at the deep zone and propagates upward. Therefore, the assumption of correlating the OA propagation with the increased tissue strain seems invalid for unconfined cyclic compression.

On the other hand, results obtained from sliding contact model showed better agreement with *in vivo* degeneration patterns and the biomechanical concept of degeneration. Although changes in fluid pressure and tissue strains mostly occurred in the superficial zone, a slight increase ($\sim 4.0\%$) in tissue strains was predicted in the deep zone. That was also accompanied by slight reduction in fluid pressure and fluid flow rate. This disruption in the biomechanical environment of the chondrocytes residing in the lower zones could lead to depth dependent matrix remodeling. Over time, as the superficial zone vanishes, the matrix remodeling in the lower zone could accelerate with the increased stresses and strains. Furthermore, it is also documented that the cartilage stiffness decreases through the depth; however, the deep zone is prevented from lateral expansion by fixation to subchondral
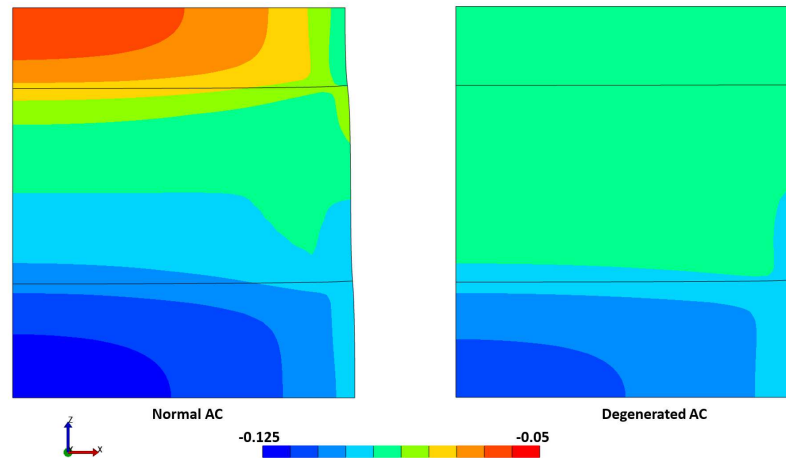
Figure 2.15: Peak of the axial strain, predicted during the last cycle of cyclic compression, for normal cartilage (Left) and degenerated cartilage (Right)

bone. Hence, the increased fluid pressure in this zone contributes to the overall stiffness of the tissue. As a result, tensile strain, caused by loading, mostly occurs in the superficial zone, regardless the high tensile stiffness of this zone. That is in line with mechanobiological studies on isolated chondrocytes which have shown that chondrocytes of the deep zone are stimulated by compressive strain (Lee et al., 1998) while superficial zone cells may be stimulated by tensile strain (Vanderploeg et al., 2008).

Flat vs Curved Surface

Early in the simulation, and due to fast compression rate compared to relatively long characteristic path, the distance that fluid travels to exit from a free draining region, added to the high tensile stiffness of the superficial zone, the fluid was trapped near the radial periphery which increased the fluid pressure in that location , see Figure 2.16 (top). In contrast, in curved surface model, the maximum fluid pressure was located at the center of the sample where most of tissue deformation occurred. Hence, fluid pressure predicted at the sample center in the superficial zone was higher in curved surface model compared to flat surface model.
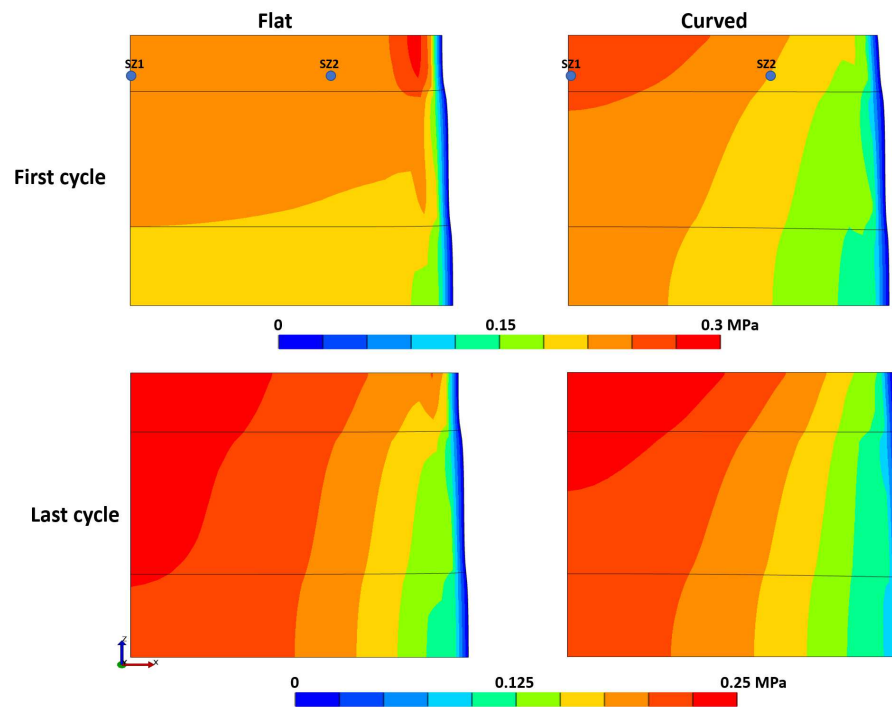
Figure 2.16: The fluid pressure distribution predicted at the first and the last loading cycles, flat surface model (Right) and curved surface model (Left).

Over time, the fluid pressure distribution becomes more uniform with depth in both models as can be seen in Figure 2.16 (bottom). Interestingly, the maximum fluid pressure remained nearly constant in the curved surface model with total reduction of only 2.7% compared to 17.6% in the flat surface model, by the end of simulation. That is mainly attributed to the availability of larger free-draining area in curved surface model. Increased free draining surface, in curved surface model, allowed for more fluid imbibition during the unloading cycle. That is very important as it suggests that the free-draining area available during typical unconfined compression seems to be insufficient for maintaining tissue hydration or providing the chondrocytes with the required oxygen and nutrients during mechanobiological testing. That could explain the frequency-dependent radial aggrecan stimulation observed by Buschmann et al. (1999).

Surface curvature could also be important from a tribological point of view as it is suggested by Moore and Burris (2017) who observed that lost fluid pressure could be recovered even with a static contact area, provided an opposing surface was sliding over the cartilage. This requires a convergent wedge and physiological sliding speeds, a phenomenon they called "tribological rehydration". *In vivo*, that could be very effective in joints where the contact location changes with limited sliding or rolling, e.g. within the spine.

The effect of surface curvature on tissue strains was greater in the deep zone and near the radial periphery compared to the superficial zone and the center of the sample. Due to the low tensile stiffness of the deep zone and the nature of unconfined compression, higher tissue strains were predicted by flat surface model in the deep zone and near the radial periphery, see Figure 2.13.

2.5   Conclusions

In conclusion, this study has clearly demonstrated the necessity of incorporating physiological loading conditions in mechanobiological *in vitro* testing of cartilage explants. In particular, the effect of sliding on the mechanical environment within cartilage tissue was demonstrated, which may be important for mechanobiological studies, especially in understanding the *in vivo* chondrocyte environment.

During sliding load in this study, low and constant tissue strains were sustained for the entire simulation time. On the other hand, unconfined cyclic compression, the typically used *in vitro* testing regime, caused continuous fluid exudation and quick reduction in the fluid pressure as a result. Furthermore, unlike the radially dependent distribution of fluid pressure and tissue strains, predicted in unconfined cyclic compression, sliding contact loading mode predicted depth dependent

distribution which is well correlated with the well know depth dependent structure and composition of cartilage.

Moreover, the increase in lateral strain in the lower zones observed under unconfined cyclic compression is non-physiological as the tissue is prevented from lateral expansion by fixation to subchondral bone. That is expected to result in non-physiological mechanobiological response of the chondrocytes of this zone as studies on isolated chondrocytes have shown that chondrocytes from the deep zone are stimulated by compressive strain (Lee et al., 1998) while superficial zone cells may be stimulated by tensile strain (Vanderploeg et al., 2008).

Moreover, using specimen with perfectly flat surface seems to reduce tissue rehydration under unconfined cyclic compression which could lead to radially uniform mechanobiological response in frequency-dependent manner (Buschmann et al., 1999). In addition, simulation of early osteoarthritis showed that cartilage response under unconfined cyclic compression violates the well documented depth-dependent propagation of the disease (Andriacchi et al., 2004).

Therefore, and since the function of a synovial joint involves changing the contact area or contact pressure for many common daily activities (Bergmann et al., 2001; Kura et al., 1998; Wong et al., 1999), *in vitro* testing of cartilage, such as chondrocyte response to load, should consider realistic loading conditions at the bearing surface. Most importantly, a migrating contact area could provide important information about cartilage mechanobiology and affect the development of tissue biomechanical properties in tissue-engineered cartilage constructs.

Chapter 3

Custom-made Devices for Cartilage Testing

3.1 Introduction and Literature Review

In healthy synovial joints, the integrity of articular cartilage matrix is maintained through a balanced interaction between anabolic and catabolic activities. In OA, this process might tilt toward the catabolic activity, by activating degrading enzymes such as metalloproteases (MMPs) and aggrecanases (Grodzinsky et al., 2000; Wang et al., 2004). The exact mechanism by which the chondrocyte shifts to this abnormal phenotype is still uncertain. However, clinical observations and animal studies have long linked this behavior to the chondrocytes' response to their mechanical environment (Haapala et al., 1999; Kiviranta et al., 1994). Therefore, the response of cartilage to mechanical stimuli has been an area of extensive research (Grodzinsky et al., 2000; Grad et al., 2011).

Providing valuable insights into the biological response of cartilage, *in vitro* experiments have used different loading protocols, modes, amplitudes, and frequencies (Sah et al., 1989; Kim et al., 1994; Guilak et al., 1994a; Buschmann et al., 1999; Quinn et al., 1998a; Ackermann and Steinmeyer, 2005). However, the loading

configurations used in these studies were always simplified and omitted the importance of physiological conditions (i.e. sliding, migrating contact area). As can be interpreted from Table 3.1, uniaxial unconfined compression which does not replicate the *in vivo* loading conditions in synovial joints was the most commonly used loading protocol. However, during daily activities, the articular cartilage is subjected to a combination of compression and sliding which result in velocity-dependent cyclic fluid pressure and shear forces. The relative motion of the articulating surfaces was also found to be vital for tissue load support during normal activities by protecting tissue matrix and chondrocytes from high strains and stress (Ateshian, 2009).

That makes incorporating physiological loading conditions in *in vitro* mechanobiological testing of cartilage seem rational. However, only a few studies have attempted to carry on experimentation where the relative surface motion was considered (Correro-Shahgaldian et al., 2014; Schätti et al., 2015, 2016). Correro-Shahgaldian et al. (2014) have investigated the effect of plowing on the biological response of cartilage and showed that plowing causes cell death at the cartilage surface and induces GAG release by activating catabolic enzymes, i.e. MMP-3 which degrade the tissue. However, while it is reasonable that harsh loading conditions such as plowing may cause cartilage surface damage, cell death, and activation of catabolic enzymes, the choice of the cartilage sample source in this experiment seemed questionable. The tested samples were obtained from bovine nasal septum which is a non-load bearing hyaline cartilage and known to contain higher GAGs and lower collagen content compared to articular cartilage (Ignat'eva et al., 2004; Correro-Shahgaldian et al., 2016). Tensile stiffness and shear strength of cartilage are provided by collagen content (Mow and Guo, 2002). Hence, the tissue's

ability to withstand in-plane forces such as plowing will be compromised. There-fore, inaccurate information may be obtained from *in vitro* mechanobiological test-ing that applies loading condition of articular cartilage to non-articular cartilage specimens.

In other recent *in vitro* studies, the effect of surface relative motion during slid-ing on the mechanobiology of cartilage was investigated (Schätti et al., 2015, 2016). The results of these studies showed that changes in gene expression associated with extracellular matrix proteins were correlated with the strain level in the tis-sue. The main advantage of the work of Schätti et al. (2016) was the use of a load-controlled system resembling the loading conditions in the synovial joint. How-ever, the minimal strain applied by the device was more than 25%. It should be noted that the equilibrium compressive strain in cartilage was estimated to be less than 20% (Armstrong et al., 1980), but during motion and due to the contribution of the fluid load support, the compressive strain is expected to be much lower (Bonnevie et al., 2011). High level of strain is well documneted to induce catabolic effects on cartilage metabolisim (Wong et al., 1999). This was proven by a more recent study of Schätti et al. (2018) which showed that even with sliding, increased ECM strain induces enzyme-mediated catabolic processes and results in signifi-cant PG loss. Therefore, mechanobiological testing of cartilage at lower strain level strains should be conducted.

Further, the loading duration of the test was extremely short, less than one hour. Unlike the cartilage mechanical response, the biological response is expected to re-quire long time to be detected. For example, aggrecan gene expression was found to increase during short duration, e.g. 1 hour, of compressive loading. However, it was reduced to normal level after 4 hours of testing (Valhmu et al., 1998).

Moreover, studies of Schätti et al. (2016, 2018) both used a whole bovine

condyles in their experiments. It is well documented that osteoarthritis involves subchondral bone remodeling which result in subchondral bone sclerosis, calcified cartilage thickening and duplication of the tidemark (Kawcak et al., 2001). Increased bone mineral density (BMD) was also observed in hip joints with morphological abnormalities (Speirs et al., 2013). That could suggest that the integrity of the articular cartilage and initiation of osteoarthritis highly depends on the mechanical properties of the underlining bone plate. As the role of subchondral bone and other joint components in enzymes release is still uncertain, de-coupling the subchondral bone's contribution to the pathophysiology of OA is critical to understanding the disease process. Hence, the development of an *in vitro* model that allows isolated observations of the articular cartilage under physiological conditions is vital.

In the first study of this thesis, Chapter 2, it was shown that maintaining high fluid load support by relative surface motion could alter cartilage biomechanical behaviour which may enhance the tissue's mechanobiological response. Therefore, this study aimed to develop a testing apparatus that allows for biomechanical and mechanobiological *in vitro* testing of articular cartilage with and without subchondral bone under well controlled conditions. For comparison purposes, uniaxial loading apparatus will also be constructed. Hence, there were two devices developed in this study. The first device is to apply compression and sliding contact with a migrating contact area. The device should produce fluid pressure, fluid flow, and tissue strains within the physiological level. The second is to perform uniaxial compression tests at various strain and strain rates. The uniaxial apparatus will be described in Section 3.5.

Table 3.1: Summary of testing configurations used for mechanobiological testing of cartilage explants.

Loading Configuration	Species/Age	Sample Size	Key Findings	Reference
Static and dynamic compression/Latterly Unconfined	Bovine/Immature Human/Adult	D = 2-5 mm h = 0.5-1 mm	Oscillatory strains can modulate chondrocyte biosynthesis but not static compression.	(Sah et al., 1989; Guilak et al., 1994a; Kim et al., 1994, 1995; Quinn et al., 1998b; Wong et al., 1997, 1999; Buschmann et al., 1999; Jeon et al., 2012)
Dynamic shear/Latterly Unconfined	Bovine/Immature	D = 3 mm	Macroscopic shear deformation increased the synthesis of proteoglycan and some other proteins	(Frank et al., 2000; Jin et al., 2001; Fitzgerald et al., 2006)
Injurious compression/Latterly Unconfined	Bovine/Immature	D = 3 mm	At low-amplitude cyclic mechanical loading, injuriously compressed cartilage loses its characteristic anabolic response.	(Kurz et al., 2001, 2004; Patwari et al., 2003, 2004, 2007; Loening et al., 2000; Li et al., 2013)
Plowing-sliding/Cylindrical indenter (D = 25 mm)	Bovine/Mature	Cartilage strips (60 × 17 × 2mm)	Cell death near the surface, GAG loss, and activation of catabolic enzymes such as MMP-3.	(Correro-Shahgaldian et al., 2014; Schätti et al., 2015)
Sliding/Spherical indenter (D = 25 mm)	Bovine/Mature	Femoral condyle head	Changes in gene expression of extracellular matrix proteins are correlated with strain and contact stress.	(Schätti et al., 2016, 2018)

3.2 Sliding Contact Load-Controlled Apparatus

Over the course of the day, the synovial joints support large dynamic loads and permit a wide range of motions at an excellent performance. During walking cycle, for example, the sliding velocity ranges from $0 - 60 \ mm/s$ in the hip joints (Fisher et al., 1994) and up to 300 mm/s in the knee joints (Neu et al., 2008), high velocity occurs during the swing phase. During the loading phase, joint motion usually involves sliding (translational) and/or rolling motion. Hence, different modes of lubricating mechanism are believed to come into play during a daily activity (Murakami, 1990). Biphasic lubrication is widely accepted mode of lubrication in the synovial joints which is produced when the interstitial fluid pressurizes to support most of the applied load. Tribological studies have shown that biphasic lubrication can be sustained for long period of time when the contact area migrates at a speed that is much higher than characteristic velocity of interstitial fluid flow in articular cartilage, also called diffusive velocity (Ateshian and Wang, 1995; Pawaskar et al., 2007; Caligaris and Ateshian, 2008; Bonnevie et al., 2011). The relationship between the sliding velocity and diffusive velocity is represented by Peclet number (Pe) (Soltz and Ateshian, 2000).

$$Pe = \frac{vh}{H_{+A}k} \tag{3.1}$$

where v is the sliding speed, h is the cartilage thickness (diffusion distance), H_{+A} is the tensile equilibrium aggregate modulus, and k is the hydraulic permeability.

Therefore, knowing the cartilage material properties and thickness, the characteristic fluid velocity can be estimated to be within the range of $0.5 - 20 \ \mu m/s$. That corresponds to $Pe \gg 1$ for any sliding speed that is greater than 200 $\mu m/s$. In fact,

it has been experimentally verified that high interstitial pressurization can be sustained for long period at sliding speeds as low as 50 $\mu m/s$ (Caligaris and Ateshian, 2008). That was also reproduced by number of tribological studies, listed in Table 3.2, using smaller indenter sizes and shorter sliding distance.

Table 3.2: Number of tribological experimentation that confirmed biphasic lubrication in articular cartilage during sliding contact.

Reference	Sliding speed (mm/s)	Stroke length (± mm)	Indenter radius (mm)	AC specimen diameter (mm)
(Caligaris and Ateshian, 2008)	$0.5 - 5$	10	6.5 & 18	Full tibial plateau
(Bonnevie et al., 2011)	$0.05 - 5.0$	1.5	3.2 & 0.8	10
(Accardi et al., 2011)	$2.5 - 20$	$0.25 - 2.0$	3.0	10
(Moore and Burris, 2014)	$0.05 - 4.5$	1.5	3.175	12.7

Depending on type of activity, the load transmitted across the synovial joints could be several times of body weight (Bergmann et al., 2001) and the contact pressure could reach as high as 18 MPa (Hodge et al., 1989). However, under moderate activities, e.g. normal walking, the contact pressure ranges from 1 to 6 MPa (Hodge et al., 1989; Park et al., 2004; Shirazi et al., 2008). Hence, the range of contact pressure was kept at the low end of moderate level to minimize wear damage (Carter et al., 2007). The maximum contact pressure (σ_c) is given by Jaffar (2006):

$$\sigma_c = \frac{2.W}{\pi.a^2} \tag{3.2}$$

where (W) is the applied load and (a) is the contact radius which relates the sphere radius (R) to the contact depth (δ) by Hertzain theory of a sphere and half-space contact (Johnson and Johnson, 1987): $a = \sqrt{\delta.R}$

Axial indentation testing suggested the sample radius need to be at least four times the contact width as the indentation effects should negligible at such distance (Spilker et al., 1992). Given moderate contact pressure, cartilage deformation during sliding is expected to be less than 10%. Hence, given this contact depth, sample radius ($r = 5\ mm$), thickness ($h = 2\ mm$), added to sliding distance of $d = 3\ mm$, the maximum spherical indenter diameter can be calculated and was found to be the range of 5 mm. That is in agreement with tribological studies that used similar sample size (table 3.2). Hence, form Equation 3.2, the applied load should be within the range of $0.5 - 2.5\ N$.

The fluid load support in articular cartilage during sliding could be calculated from Bonnevie et al. (2012) analytical model based on Hertz's contact solution.

$$\frac{W^p}{W} = \frac{(E_d - E_s)}{E_d} \tag{3.3}$$

where E_d is the contact modulus during sliding (dynamic) and E_s is the equilibrium contact modulus under static loading (equivalent to H_{-A}). Hertz theory defines the contact modulus by:

$$E_C = \frac{3}{4} \frac{W}{R^{0.5}.\delta^{1.5}} \tag{3.4}$$

Under load control configuration, the load is prescribed, and contact depth is measured. Hence, the fluid load support measured by Equation 3.3, becomes a function of the contact depth alone.

$$\frac{W^p}{W} = 1 - (\frac{\delta_d}{\delta_s})^{1.5} \tag{3.5}$$

where δ_s and δ_d are the contact depths in static and dynamic equilibrium, respectively.

3.3   Apparatus Design and Construction

The developed apparatus, illustrated in Figure 3.1, main components are: a spherical-end indenter that slides over the specimen surface, at user-specified sliding speed and stroke length. A ball screw, operated by a stepper motor, that provides the reciprocating motion. Two transmissive optical encoders that record the indenter positions in axial and transverse directions.
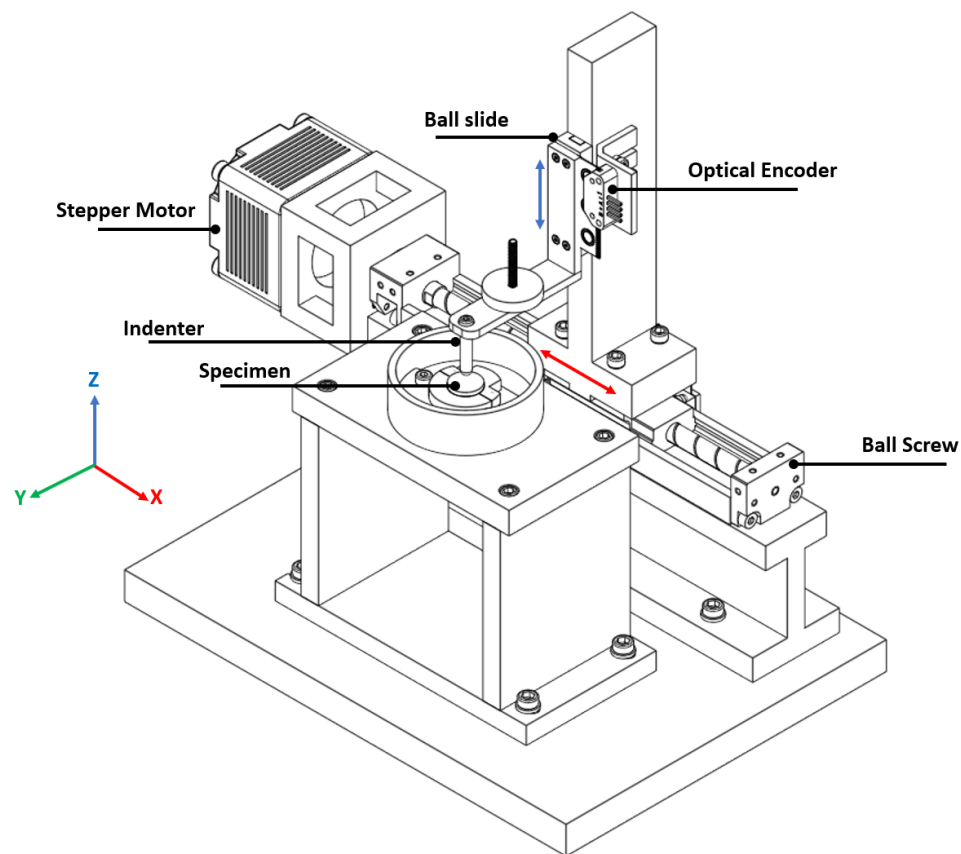
Figure 3.1: Illustration of the custom made apparatus and its main components.

3.3.1 Specimen Bath & Clamping Mechanism

In the natural synovial joint, the articular cartilage lubrication and rehydration is provided by synovial fluid that fills the joint capsule. However, *in vitro* testing of cartilage typically involves the use of substitutes for the synovial fluid such as phosphate-buffered saline (PBS) solution in tribological testing (Lakes et al., 2015) or culture media in mechanobiological experiments (Fitzgerald et al., 2006). Therefore, a stainless-steel cylindrical bath was made to have the cartilage specimen submersed in the substitute during the experiment. Under sliding, the specimen will be subjected to horizontal as well as vertical forces; thus, a specimen holder was necessary to keep the specimen in position during the test. For this purpose, a small adjustable stainless-steel clamp was designed and manufactured. The clamp was made to be removed from the specimen bath for easier placing and removing the sample as well as cleaning the system. The specimen clamp was designed to fit a specimen up to 15 *mm* in diameter. Small plastic rings of various sizes, inner diameters of 10, 11, 12, 13, and 14 *mm*, were made for the clamp to accommodate smaller specimens.
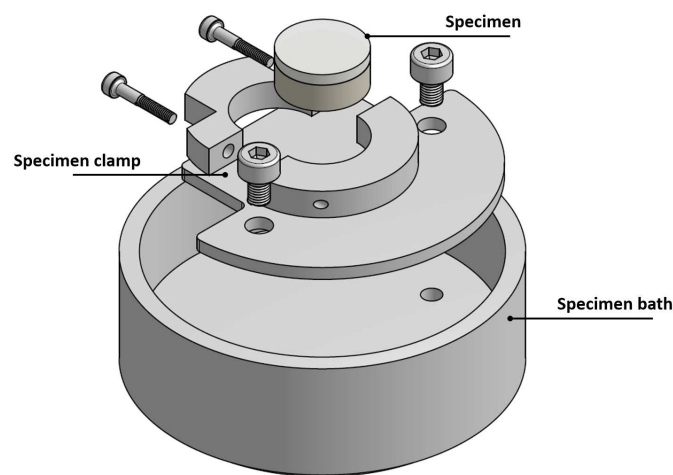
Figure 3.2: Illustration of the stainless steel specimen bath and the clamp.

3.3.2 Spherical Probe & Linear Guide

The articular cartilage specimen is loaded using a stainless-steel hemispherical probe. A truncated and threaded stainless-steel ball of diameter 4.75 *mm* was used as the spherical end of the probe. The ball was made from 440 *C* hardened stainless steel, mean surface roughness 78.75 *nm*, which provides a smooth and clean working surface. The sphere radius is much smaller than a typical radius of a bearing surface, e.g. $22 - 30$ *mm* for femoral condyle. However, this was necessary to allow fluid flow across the surface and practical limitations of specimen size as has been discussed in Chapter 2. Also, as can be interpreted from Table 3.2, tribological experiments on cartilage used indenters within this range to reproduce the biphasic lubrication promoted by migrating contact area.

The probe was attached from the other end to the cantilever beam and firmly secured using a small bolt. This allows for easy replacement of the probe by different probe type or size when needed. For example, the system will be used in this thesis to assess the cartilage material properties from typical creep tests using a cylindrical flat-end indenter. It is also possible to attach a flat platen to perform confined or unconfined compression tests. The cantilever beam is attached to a linear ball slide (DA-2, Del-Tron Precision Inc. Bethel, CT, USA), travel length of 25 *mm*. That allows it and the indenter in turn, to move in the vertical direction. The linear slide is fixed to the vertical stand which is mounted on the main base of the ball-screw, so the indenter can slide over the cartilage surface with the motion of the ball-screw. According to manufacturer specifications, the coefficient of friction of the linear ball slide is approximately 0.003; thus, it should allow for an extremely low friction motion.

Figure 3.3: Spherical and flat-end indenters.

3.3.3 Ball Screw Mono-carrier

The indenter reciprocating motion is provided by a single axis mono-carrier (Model No: MCM03010H12K, NSK Ltd, Tokyo, Japan) which converts the rotary motion of the stepper motor to a linear motion (Figure 3.4). The used mono-carrier integrates a ball screw, linear guide, and support bearing in one structure. The nominal stroke length of the ball screw is 100 mm and the lead is 12 mm. The ball-screw provides high rigidity, less than 4 μm in the radial direction, at forces as high as 500 N. Since the load carried by the linear guide of the mono-carrier in the intended experiments was calculated to be less than 2.5 N, the mono-carrier load deformation can be assumed negligible. However, measurement of the compliance in the whole system will be carried out to ensure that any load deformation is to be subtracted from the raw data before analysis.

Figure 3.4: Illustration of the mono-carrier. http://www.nsk.com.

3.3.4 Stepper Motor

The motion source of this system is a NEMA 23 high torque stepper motor (Model No: 23Y002D-LW8, Anaheim Automation Inc. Anaheim, CA, USA). Stepper motors produce high torque and a precise control over the speed and position. In stepper motors, digital pulses are converted into rotational motion and the motor can be moved through a defined angle for each pulse. For example, the stepper motor used in this apparatus has a step angle of 1.8 *degree* or 200 *steps/rev*. That means, the motor is rotated by 1.8 degree with every pulse. The lead of the attached ball-screw is 12 *mm* which means it travels 12 *mm/rev*, or 60 *µm/step* or pulse. Finer resolution, up to 0.6 *µm*, can be achieved when micro stepping functionality in the stepper motor drive is used.

Running the stepper motor:

To run a stepper motor correctly, a stepper motor driver that generates the correct sequence of signals for the step and direction as well as a signal source, usually micro-controller, are needed. A stepper motor drive (STR4, Applied Motion Products Inc., Watsonville, CA, USA) was used to drive the linear motion system. This stepper motor driver allows for high step resolution, as high as 20000 steps/rev which provides theoretical linear resolution of 0.6 *µm* with the used ball-screw. Micro-stepping is useful for smoothing the motion of the stepper motor and to avoid mechanical resonance that can occur at certain speeds. The drawback of using micro-stepping is that the time stepping must be reduced which is limited by the motor and the micro-controller minimum time step. Therefore, micro-steeping is useful at low speeds.

The selected stepper motor maximum rotational velocity is 400 RPM. Hence ideally linear speed of 80 *mm/s* cab be achieved. As the rotational velocity of the motor is proportional to pulse frequency or the time step, it is not possible to

achieve high speed with micro-stepping as it requires high pulse frequency which is limited by the minimum time step of the stepper motor and the micro-controller as well. Micro-stepping also reduces the torque provided by the stepper motor, but that should not be an issue, given the high torque of the used stepper motor. Please refer to Appendix A for stepper motor calculations.

A micro-controller (Arduino Uno, Arduino, Turin, Italy) was used to send the step and direction pulses to the stepper driver at a frequency proportional to the desired motor speed. This apparatus was intended to run at constant sliding speed; however, it is straightforward to produce smooth motor acceleration or deceleration by smoothly ramping up or down the step speed using the micro-controller. More information on the sliding speed and the achieved linear resolution will be provided in Section 3.3.1.

3.3.5 Displacement Sensors

Two optical incremental encoders (EM2 Transmissive Optical Encoder, US Digital, Vancouver, Washington, USA) along with high resolution (2000 lines/inch) linear strips were used to record indenter vertical and horizontal displacements. The indenter vertical displacement represents the indenter contact depth while the horizontal displacement is the measure of the indenter position as it travels over the cartilage surface.
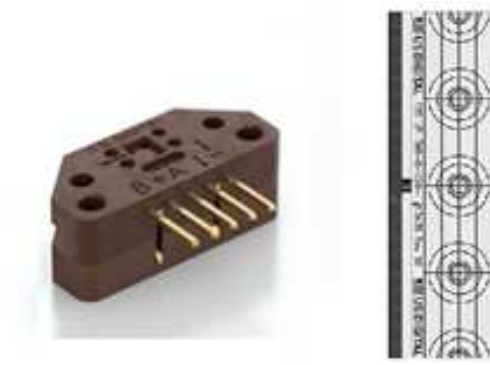
Figure 3.5: EM2 transmissive encoder with linear strip. https://www.usdigital.com.

The EM2 encoder consists of a light emitting diode (LED) on one side and a light detector on the opposite side. In between the light emitter and detector, the linear strip passes. Therefore, when the encoder is used as the moving part the linear strip must be stationary and vice versa. In this apparatus and to minimize the load of the indenter on the cartilage specimen, the linear strip was attached to the cantilever beam while the encoder was fixed on the vertical stand as shown in Figure 3.1. Thus, vertical deformation of the tissue surface can be recorded by vertical displacement of the linear strip attached to the indenter. The second encoder, that was used to track the horizontal displacement, was attached to the moving part, the vertical stand, while the linear strip was fixed to the stationary mono-carrier body. Using EM2 in quadrature mode with the chosen linear strip provides a position resolution of 3.175 μm.

To make position measurements, a counter click board (Counter Click, MikroElektronika D.O.O., Belgrade, Serbia), shown in Figure 3.6, was used. The board carries LS7366R 32-bit quadrature counter and pinout for receiving A and B signals from incremental encoders. Table 3.3 shows the pinout table of the EM2 incremental encoder and their corresponding input on the counter click board.
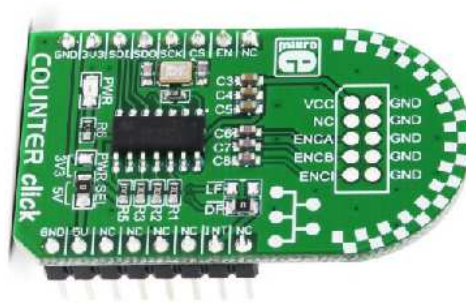
Figure 3.6: Counter click board.

Table 3.3: Pins connections between EM2 encoder and counter click board.

Pin on EM2 encoder	Signal	Pin on click board
1	GROUND	GND
I	INDEX	ENCI
A	Channel A	ENCA
+	+5V DC Power	VCC
B	Channel B	ENCB

On the other side, the counter click board communicates with the microcontroller via SPI (Serial Peripheral Interface). Lastly, the counted pulses, or the encoder reading, are converted to displacement using the following formula:

$$Displacement \; [in] = (n/X.CPI)$$

where CPI = counts per inch (2000 for the used linear strip), X = encoding type (4X for quadrature), and n = total number of counts.

3.3.6 Indenter-Cartilage Surface Contact

The apparatus was designed to apply a static load to the cartilage explant by allowing the indenter to freely sit on the cartilage surface. A small servo motor

(TOWERPROSG-90 Micro Servo, Shenzhen Industrial Product Exhibition, Shenzhen, China) was used to bring the indenter in contact with the specimen surface at the start of the test and off-contact when the test is completed. The servo motor (not shown in apparatus image) was attached to the vertical stand, below the cantilever beam. At the start of a test, the servo arm is slowly lowered from (90°) position to (0 °) position. The indenter-cartilage contact should occur before the servo arm reaches (0 °) position. To remove the indenter off the cartilage surface, the servo arm is rotated back to (90 °) position, as shown in Figure 3.7.
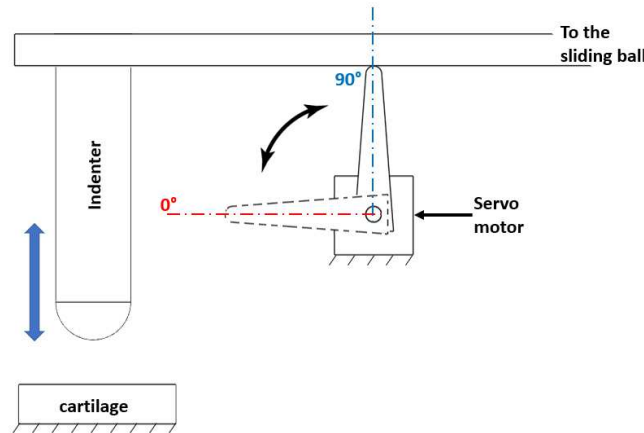
Figure 3.7: The mechanism of lowering and lifting the indenter, synchronized with initiating and ending the test.

Due to the difference in specimen heights, the vertical displacement of the indenter at which the contact with specimen occurs varies. Therefore, a force-sensing resistor (FSR) (Model No: 406, range $0.2 - 20\ N$, and resolution of $\pm 2\%$), was placed underneath the specimen bath to detect the change in the total bath weight caused by indenter cartilage contact. When the initial contact is detected, the micro-controller begins recording the indenter vertical (Z) and horizontal (X) positions using the optical encoders. The first recorded readings form vertical and horizontal encoders will be (Z_0) and (X_0), respectively. The indenter displacement

in (Z) and (X) are taken relative to (Z_0) and (X_0), as shown in Figure 3.8. The sliding motion can be synchronized to initiate upon load application or after a predefined pure compression period.
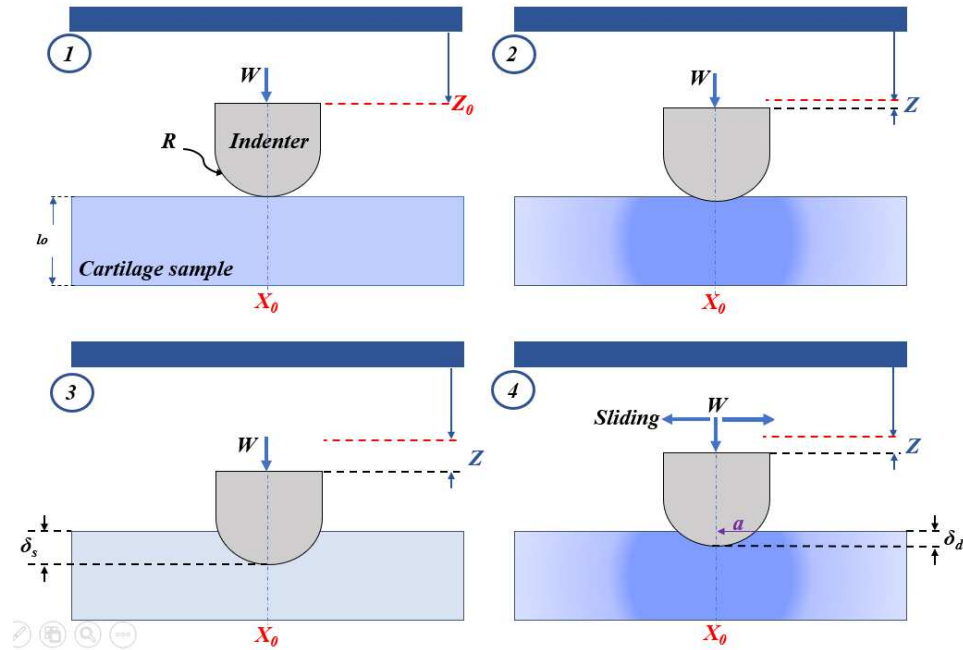
Figure 3.8: Sliding test procedure. 1: Contact, 2: Penetration, 3: Static equilibrium, and 4: Dynamic equilibrium. Z & X are the readings of the vertical and horizontal encoders, respectively.

3.3.7   Sliding Contact Apparatus Estimated Cost

Commercial mechanical testing devices come at very high cost. For example, MTS uniaxial test system was quoted nearly at $100,000.00 USD. Besides, commercial devices are made for testing a wide range of engineering materials which markedly exceeds articular cartilage testing requirement. Hence, a significant cost saving could be made if the apparatus was a constructed in-house as can be seen from Table 3.4. The cost of the developed apparatus was extremely low, less than 1000

CAD. As noted, some of the main components were inherited from Robotic analysis, design, and control lab in the Mechanical and Aerospace Engineering Department, Carleton University, thanks to Prof. Mojtaba Ahmadi. However, these parts or similar can be found at low cost, as noted in the last column. Hence, the total cost of the developed apparatus is still under $1000.00 CAD.

Table 3.4: Estimated cost of the sliding contact apparatus components.

Item No.	Quantity	Description	Price (CAD)	Notes
1*	1	Nema 23 Stepper motor	–	Current price ($75)
2*	1	Ball screw	–	Price of similar product ($200)
3*	1	Stepper-motor drive	–	Current price ($140)
4	2	EM2 optical encoder	$160	Including the linear strip
5	1	Ball slide	$100	–
6	1	Stainless steel truncated ball	$45	Used as indenter tip
7	2	Micro-controller	$40	Arduino UNO
8	1	Counter click board	$20	–
9	–	Miscellaneous	$100	(wires, screws, metals, etc..)
		Apparatus total cost	$465	

*: Parts were donated by Robotic analysis, design, and control lab.

Mechanical and Aerospace Engineering Department, Carleton University.

3.4 Sliding Contact Apparatus Assessment

To evaluate the apparatus performance, a series of tests and measurements were performed. Before using the apparatus for testing actual cartilage specimens, the accuracy of the sliding speed, position measurement, applied load, and compliance in the system were evaluated. The apparatus was then validated by using it for assessing cartilage behaviour under both static and mobile loading conditions. Indentation creep tests were performed to assess the material properties of bovine articular cartilage. Under dynamic conditions, the apparatus was used to estimate the fluid load support during sliding in healthy bovine cartilage. Results from both static and dynamic tests were compared against data from the literature.

3.4.1 Loading the Sample and Compliance in The System

Although the friction in the linear slide is very low (~ 0.003) as per the manufactures' information, measurement of the possible effect of the friction on the applied load was performed using high precision scale, from Taylor Digital Precision Diet Scale Maximum capacity of 500 g and 0.01 g increments. The measurement was conducted by placing the indenter tip on the scale and increasing the load while recording the scale reading. As mentioned earlier, the apparatus was designed to apply a static weight to the cartilage surface using small metallic weights shown in Figure 3.9. Therefore,

Figure 3.9: Metallic weighs.

the minimum load that can be applied by the apparatus is the load caused by the cantilever beam with indenter weight without any additional loads. The loads can be added as needed by placing small weights on the cantilever beam as shown in

Figure 3.10, Right. During sliding added weights are secured using a small bolt to minimize noise in the system. The load was then increased slowly by placing more weight on the cantilever beam while recording the scale reading each time. After the total of 100 g was reached, the added weighs were removed one by one and the scale reading was again recorded. The average of the two scale readings of each load was taken to be exact value. Figure 3.10 shows the linearity of the loading mechanism of the system.
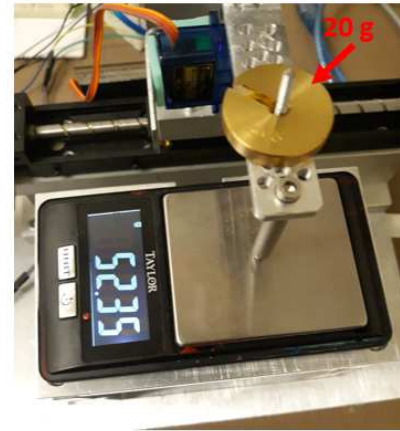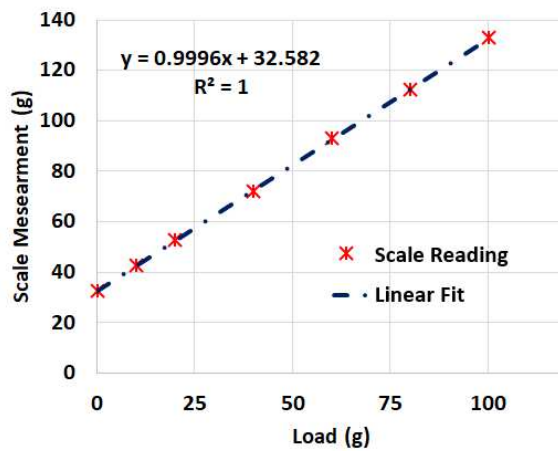
Figure 3.10: Load vs scale reading, Left. The indenter as loaded by additional 20 g, Right.

As mentioned in Section 3.3.5, the encoder resolution is 3.175 μm. That makes it difficult to measure the deflection of the apparatus. However, measurement of the compliance in the system was carried out by lowering the flat ended indenter onto a rigid metallic plate while increasing the load by 10 g up to 100 g. Meanwhile, the load and vertical displacement were continuously recorded. Only one encoder reading (3.175 μm) was recorded as the load exceeds 100 g. Therefore, in the actual test and due to high rigidity of the system compared to the cartilage sample stiffness add to the load-control nature of the system, compliance in this apparatus can be neglected, especially in the range of loads used by this apparatus $0.5 - 2.5\ N$.

3.4.2   Encoder Calibration

To ensure the encoder reading is precise and repeatable, the encoder was calibrated using gauge blocks (L.S Starrett model number RS92A1). To perform the calibration, the specimen bath was removed and replaced by a large gauge block. The flat end indenter was lowered onto the large gauge block, the point which is taken as reference. Several blocks were used to cover displacement range of $0.05 - 0.5\ in$. Each gauge block was inserted between the large block and the indenter, as shown in Figure 3.11. Thus, the reading of the vertical encoder corresponding to the size of the used gauge block is recorded. The measurement was repeated three times with each gauge block.
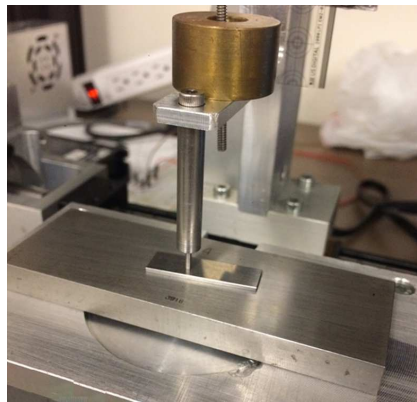
Figure 3.11: Encoder calibration procedure.

Table 3.5 lists the each gauge block size and the corresponding encoder reading. Readings 1, 2, and 3 refer to the encoder counts recorded against the used gauge block each time. The total number of counts (n) is then converted into distance as shown in Section 3.3.5. The percentage error and the stranded deviation of the three readings is shown in the last column. Since both encoders used in the vertical and horizontal directions are identical, calibration of the vertical encoder was considered sufficient.

Table 3.5: Optical encoder calibration results. Readings are given in counts (see Section 3.3.5)

Block size (mm)	Reading 1	Reading 2	Reading 3	Error (%)
1.27	401	403	400	$0.33\% \pm 0.31$
3.81	1202	1199	1199	$0.0\% \pm 0.12$
6.35	2001	1998	2001	$0.0\% \pm 0.07$
8.89	2800	2799	2801	$0.0\% \pm 0.03$
12.7	3998	3996	3998	$-0.06\% \pm 0.02$

From the calibration results, maximum percentage error occurs at the smaller distance. However, given encoder resolution, 3.175 μm which corresponds to an expected error of 0.25%, this error is within the acceptable range. Optical encoders were selected for this design due to cost-effectiveness considerations. In future, both encoders can be replaced by linear variable displacement transformers (LVDT), if necessary.

3.4.3 Sliding Speed Accuracy

As discussed in Section 3.2, high fluid load support was maintained at sliding speeds as low as 0.05 mm/s. Therefore, to evaluate the apparatus position accuracy and repeatability, a series of tests were performed by moving the indenter in the X direction with linear motion profile while the horizontal encoder tracks the probe X-position at sampling rate of 0.5 kHz. Various sliding speeds (0.1, 0.5, 1, 3, 5, and 10 mm/s) were prescribed while the stoke length was kept constant at $\pm$ 3 mm. Due to the minimum time step in the system, micro-stepping was used to smooth the ball-screw motion only at low speeds. The actual sliding speed was calculated as the derivatives of the probe X-position signal. Table 3.6 lists the prescribed, actual sliding speed, and the achieved system resolution.

Table 3.6: Prescribed sliding speed and system resolution.

Ideal Speed [mm/s]	Step time [ms]	Steps/Rev	Actual Speed [mm/s]	System Resolution [μm]
10	3	200	9.01	60
5	3	400	4.52	30
3	5	400	2.8	30
1	3	2000	0.90	6
0.5	6	2000	0.46	6
0.1	6	20000	0.09	0.6

As can be seen in Table 3.6, the measured sliding speed was found to be 10% lower than prescribed speed. That could be due to actual voltage provided to the stepper motor or the time step. Since the error value is constant, the time step can be adjusted to achieve the required sliding speed. Also, lower number of steps per revolution reduces the system resolution as the indenter will travel longer distance with each step. For example, at 10 mm/s the indenter travels 60 μm/step or 3 ms. Finally, the backlash, which occurs as the motor switches to rotate in the opposite direction, was found to be less than 20 μm. Hence, it should not have an impact on the test or on the data collected at the center of the specimen as it can be controlled to occur at the specimen radial edge.
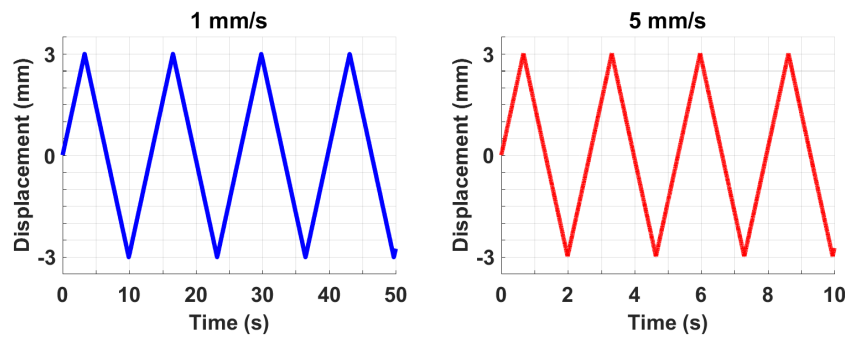
Figure 3.12: Indenter position when sliding at 1 and 5 mm/s and stroke length of ± 3 mm.

Measurement of indenter positions in vertical and horizontal direction allows for precise determination of tissue deformation during sliding at any chosen location along the sliding path. Using the minimum load, the apparatus gives the possibility of determining the specimen surface topography allowing for generating 2D geometry of the specimen if needed, as shown in Figure 3.13. Also, specimen was clamped across its diameter from the subchondral bone which prevented any specimen movement during the test. Further, visual inspection did not find any damage or crack in the bone layer which was expected given relatively low contact force applied during cartilage testing. A small gap remained between opposing clamped surfaces (where bolts cross, see Figure 3.2) resulting in rigid clamping of the specimen across the diameter. Since sliding occurred across this diameter with very low friction, motion of the specimen was assumed negligible compared to the sliding distance. Although this wasn't measured, no motion could be observed during tests.
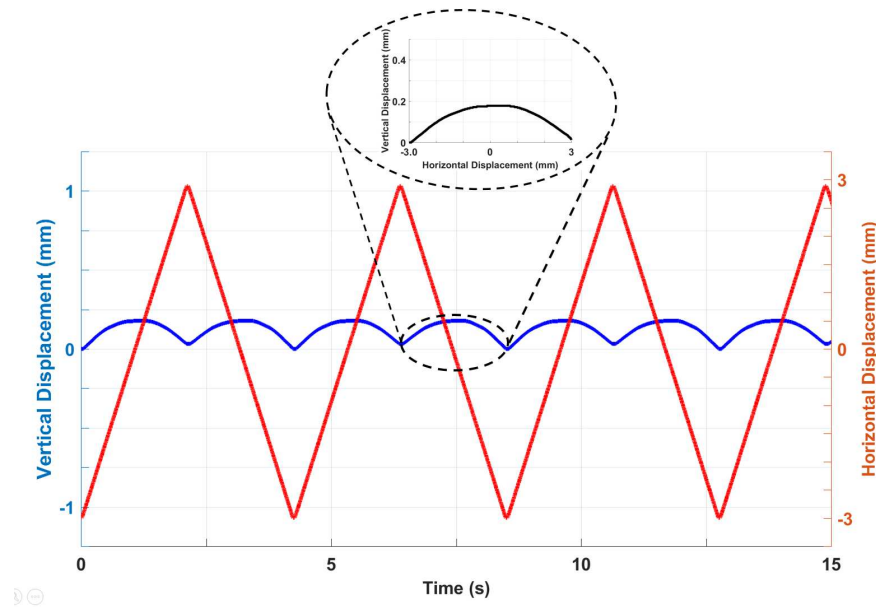
Figure 3.13: Vertical and horizontal indenter position during sliding over cartilage specimen, sliding speed = 1 *mm/s* and stroke length of ±3 *mm*.

3.5 Uni-axial Displacement-Controlled Apparatus

As discussed previously in Section 3.1, uniaxial displacement-controlled devices are commonly used for uniaxial cyclic compression in mechanobiological testing of cartilage (Sah et al., 1989; Kim et al., 1994; Buschmann et al., 1999; Ackermann and Steinmeyer, 2005). Displacement controlled devices are also used for cartilage thickness measurement by means of a needle penetration test (Jurvelin et al., 1995; Weber and Waldman, 2017) as well as material properties characterization (Laasanen et al., 2003; Speirs et al., 2017). Therefore, a displacement-controlled testing device was designed and constructed to be used for *in vitro* mechanobiological testing of cartilage by applying unconfined cyclic compression as well as cartilage thickness measurement.

3.5.1 Design and Construction

Briefly, the device consisted of a micro-stepper linear actuator (Model No: 35H4N-2.33-907, AMETEK Advanced Motion Solutions, Kent, OH, USA) that is mounted on an overhanging cantilever beam. The linear actuator provides a stroke length of 19.05 *mm* at resolution of 3.048 *µm/step*. Finer resolutions can be achieved using the micro-stepping functionality of the stepper motor drive as discussed previously in Section 3.3.4. Hence, the micro-stepper linear actuator can be used to apply user-specified strain and strain rate to the cartilage surface using a compression tool, e.g. compression platen. S-type load cell (model: JRS1, capacity 10 N, non-repeatability 0.05% and non-linearity 0.1%) was directly attached from one end to the threaded end of the actuator shaft. The compression tool or the needle can be attached to the lower end of the load cell using a small holder. An amplifier (HX711, SparkFun Electronics, Niwot, CO, USA) was used with the load cell to

measure the change in contact force due to compression of the cartilage surface. EM2 transmissive optical encoder (EM2 Transmissive Optical Encoder, US Digital, Vancouver, Washington, USA) along with high resolution linear (2000 lines/inch) strips were used to measure the position of the load cell which represents the displacement of the needle or the compression tool. The encoder strip holder was attached to the load cell to travel with the motion of the actuator while the encoder was fixed on the actuator base, see Figure 3.14. A small container was made to host the sample during the test. Since a uni-axial compression is applied to the specimen, lateral confinement of the specimen was not required. Instead, the specimen was allowed to freely sit at the bottom of the container. The displacement-controlled apparatus and its main components are illustrated in Figure 3.14.
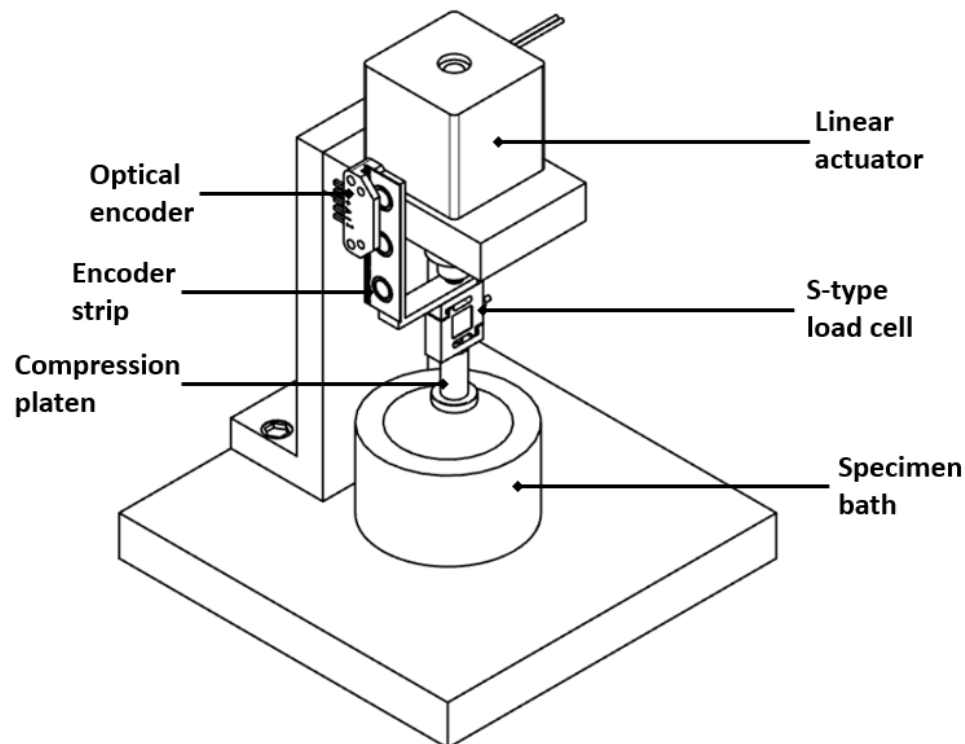
Figure 3.14: Apparatus designed and constructed for displacement-controlled testing of articular cartilage.

3.5.2   Estimated Cost

Table 3.7: Estimated cost of the uniaxial loading apparatus components.

Item No.	Quantity	Description	Price (CAD)	Notes
1	1	Linear actuator	$230	–
2	1	Load cell	$390	–
3	1	Stepper-motor drive	$25	–
4	1	EM2 optical encoder	$80	Including the linear strip
5	2	Micro-controller	$40	Arduino UNO
6	1	Counter click board	$20	–
7	–	Miscellaneous	$100	(wires, screws, metals, etc..)
		Apparatus total cost	$885	

3.5.3   Uni-axial Apparatus Assessment and Validation

As mentioned earlier, the needle penetration test is commonly used to measure the thickness of articular cartilage. In this test, the reaction force and displacement are monitored as the needle makes its way through the cartilage matrix until it reaches the subchondral bone layer which is marked by sudden and dramatic increase in the reaction force.

Therefore, the accuracy and repeatability of the displacement-controlled device were assessed by using the system to measure the thickness of a rubber block. A rubber block, nominally 6.5 *mm* thick, was first measured using an electronic digital caliper (Glowgeek, Shenzhen Sunyuan Technology Co. Ltd, Shenzhen, China). Then, the rubber block was mounted on a piece of wood of 20 *mm* high , as shown in Figure 3.15.

Figure 3.15: Measurement of rubber block thickness by digital caliper (Left) and by needle penetration test (Right).

The needle was then lowered toward the rubber block at constant speed of 0.005 mm/s while its displacement and the resultant reaction force are simultaneously recorded. The measurement was repeated three times at three different locations on the same block. The needle displacement was plotted against the reaction (Figure 3.16) and the results are presented in Table 3.8.
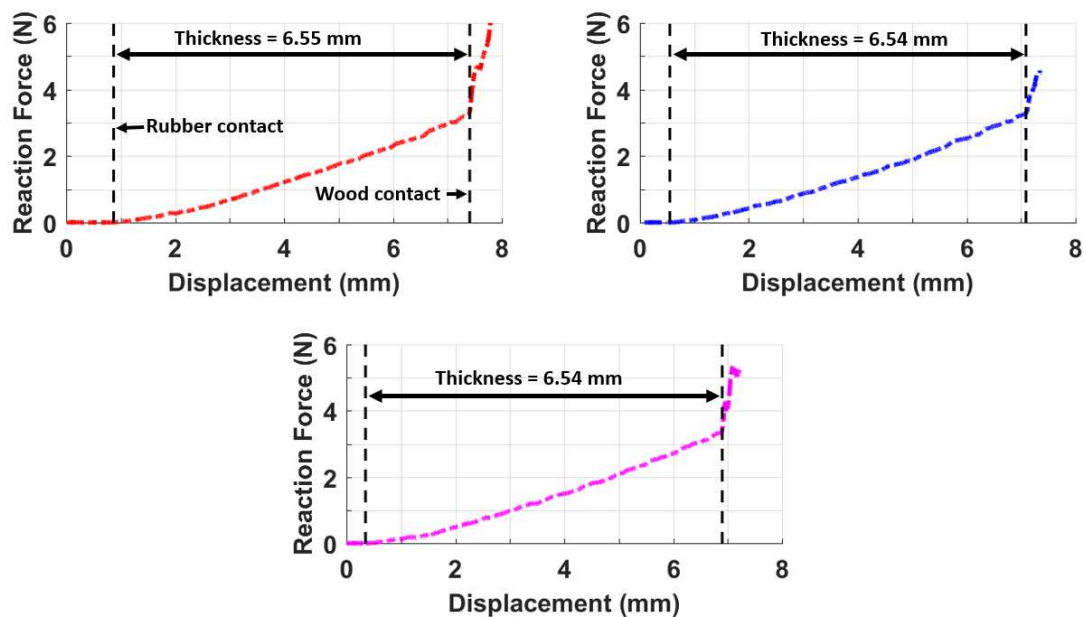
Figure 3.16: Results from needle penetration test performed on rubber block. Measurement was performed on three different locations on the same block.

Table 3.8: Rubber block thickness measured by means of using needle penetration test. Error is based on manual measurement

Test	Device Measurement (mm)	Measurement Error (%)
1	6.55	+ 0.46
2	6.54	+ 0.30
3	6.54	+ 0.30

As seen in Figure 3.16, the reaction force slowly increases as the needle makes its way through the rubber block. The sudden increase in the reaction force indicates the needle-wood contact which mark the bottom side of the rubber piece. Reaction force increases by 1 mN/μm, hence a threshold of 10 mN/μm was set as an indicator of the wood contact. The wood was chosen to avoid any damage to the needle or the device that may occur if a stiffer material was used (e.g. metals). The results presented in Table 3.8 clearly shows that the device allowed for measurement of the thickness of the rubber block with high accuracy and repeatability with error margin of $\pm 10\mu m$. The rubber block thickness obtained by the device was 0.3% higher than that obtained manually. The difference could be the result of the pressure applied by caliper on the rubber block. Therefore, the measurement of the needle penetration test device can be considered sufficiently accurate.

Chapter 4

Apparatus Validation

4.1 Sliding Contact Apparatus Validation

To validate the sliding apparatus, it was used to assess the cartilage behaviour under both static and mobile loading conditions. First, indentation creep tests were performed on bovine cartilage plugs harvested from tibiofemoral joints. The data obtained from creep tests were then used to estimate material properties of bovine articular cartilage and compare the results to values form the literature. An optimization routine available in FEBio package (Maas et al., 2012) was used to fit the creep data to a biphasic fibril reinforced finite element model.

Then the apparatus was used to study the cartilage response to dynamic loading that promotes migrating contact area. A spherical-end indenter was made to slide over the cartilage surface after a period of pure compression. Tissue deformation was recorded during both loading conditions. Finite element analysis was also performed to reproduce tissue behavior observed during *in vitro* experiments, using specimen-specific FE models.

4.1.1 Material Properties Determination

Creep Test

Indentation testing is one of the most commonly-used methods to determine the mechanical properties of articular cartilage. For simple constitutive models, (e.g. porous linear elasticity), several theoretical solutions of the indentation problem exist (Hayes et al., 1972; Mow et al., 1980; Mak et al., 1987; Mow et al., 1989; Li et al., 2015). However, articular cartilage mechanical behavior exhibits significant tension-compression non-linearity imparted by collagen fibrils orientation (Athanasiou et al., 2009) which need to be considered to accurately predict experimental outcomes (Soulhat et al., 1999). Continuous fiber distribution, proposed by Ateshian et al. (2009), one of many fibril reinforced models available in the literature, was used here to fit experimental data from indentation creep testing.

Seven osteochondral plugs, of 10 *mm* in diameter and approximately 5 *mm* thickness, were harvested from regions with relatively flat surface of freshly slaughtered, 24 month-old bovine tibial plateaus obtained from local butcher. Joints were visually inspected for signs of damage or disease. During the cutting process, the tissue was maintained hydrated by continuous flow of PBS solution. If not tested immediately, each sample was placed separately in a sealed vial filled with PBS solution and kept frozen at $-20°C$ until the day of the test. No changes in cartilage biomechanical properties were detected after a single freeze-thaw cycle at this temperature (Changoor et al., 2010). For more details on samples preparation procedure, please refer to Appendix A.

Before testing, specimen was thawed for at least 2 hours at room temperature in PBS solution. All tests were performed in air-conditioned room temperature of $23°C$; the mechanical stiffness of cartilage was found to be affected only at high

temperature, e.g. $60°C$, (June and Fyhrie, 2010). The specimen was then placed and firmly secured in the specimen bath and mounted on the testing device as described previously in Section 3.3.2. During the test, the specimen was submerged in saline solution (0.067M PO4 PBS, 1X concentration, pH 7.0-7.2, without Calcium and Magnesium, from GE Healthcare Life Sciences). Each sample first underwent a creep test using a rigid flat-end indenter of 1.6 mm diameter. A 275 mN step load was applied by the indenter to the cartilage surface for 1 h to generate the creep data. Preliminary tests showed that the applied load produces a maximum strain below the indenter at equilibrium that is less than 20% which ensures tissue deformation everywhere in the sample is sufficiently small as required by biphasic theory used for finite element analysis (Mak et al., 1987; Mow et al., 1989). Finally, the tissue was left to equilibrium for period of 30 min before cartilage thickness measurement was performed by means of needle penetration test using uniaxial displacement-controlled device developed in Section 3.4. The cartilage is assumed to restore its full thickness after this time (Athanasiou et al., 1994; Speirs et al., 2017). The cartilage thickness measurement was performed at the center of the specimen where the indentation creep test was performed

Figure 4.1: Indentation test performed on osteochondral bovine disk.

Parameters Optimization

Finite element models were created and meshed using freely available 3-D finite element mesh generator (Gmsh) (Geuzaine and Remacle, 2009) to reproduce the geometry of the 1.6 mm flat-ended indenter and cartilage specimen of 10 mm diameter with exact thickness, that was measured using the needle penetration test. The subchondral bone was omitted from the model as it has negligible effects on the cartilage response at the surface (Spilker et al., 1992; Bonnevie et al., 2012). Instead, the bottom of the cartilage was fixed in all directions and assumed impermeable to mimic the fixation to the impermeable subchondral bone plate. Free draining condition was imposed at the lateral side of the sample and the surface that is not in contact with the indenter. Due to axisymmetric nature of the creep test, only a one-degree wedge with proper boundary conditions was sufficient for the analysis, Figure 4.2.
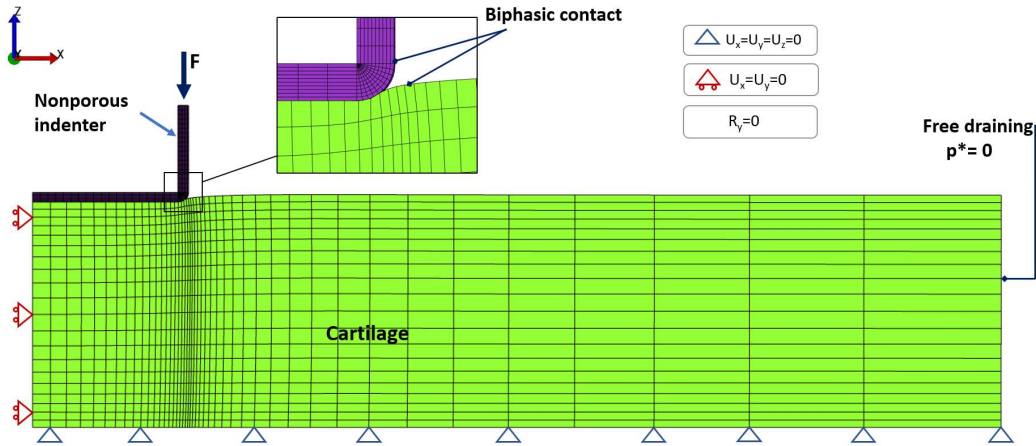
Figure 4.2: Geometry and BCs of symmetric model of indentation creep test.

The porous ground matrix was modeled as a Neo-Hookean hyper-elastic that is governed by Young's modulus E and Poisson ratio ν and reinforced by spherical continuous fiber distribution (Ateshian et al., 2009). As discussed earlier, in Section

1.4.2, the strain energy of each fiber bundle is described by a power law function that is governed by two main parameters: ξ which is the fiber modulus and β which is a unitless material property. Lastly, the interstitial fluid within the porous matrix was modeled with an isotropic and constant permeability, k.

The curve-fitting procedure was performed on three of the five fitting parameters (Aggregate modulus H_{-A}, Fiber modulus ξ, and Permeability k). The remaining two parameters (β and ν) were preset. The fiber material property β was preset for 2 to produce an almost linear tensile response at small strains (Ateshian et al., 2009). Optical measurements have shown that Poisson's ratio of the articular cartilage is extremely small due to high tensile stiffness that resists the tissue's lateral deformation (Jurvelin et al., 1997; Wang et al., 2002). Furthermore, previous sensitivity studies performed on the effect of Poisson's ratio ranging from 0 to 0.15 have shown that it has negligible effects on the determined material properties (Huang et al., 2012; Chen et al., 2016). Therefore, Passion's ratio ν was preset for 0 in which case the aggregate modulus (H_{-A}) is equal to the Young's modulus (E).

The parameters optimization analysis was started with initial guesses based on bovine cartilage material properties found in the literature. The constraints were later tightened, depending on each parameter, to reduce the simulation time. The estimated material properties are compared to other results from the literature (Moore and Burris, 2015; Chen et al., 2016)

Results

Accurate fitting was obtained for all experimental data, producing coefficient of determination $R^2 = 0.995 \pm 0.002$. The optimization time required to fit data of each specimen was approximately 40 min. As illustrated in Figure 4.3, experimental indentation creep curve is well reproduced by FEBio optimization technique using

continuous fiber distribution over the entire time frame.
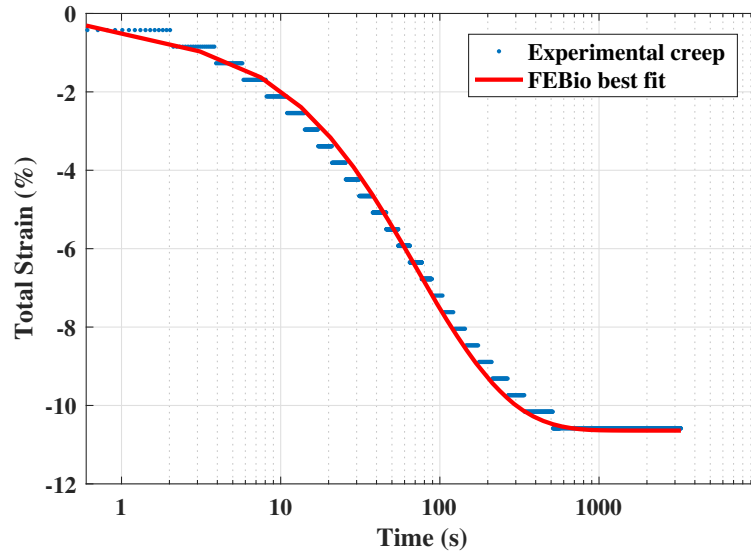
Figure 4.3: An indentation creep curve of articular cartilage from bovine tibia fitted by non-linear biphasic model.

The mechanical properties determined from the optimization process from the 7 specimens were (mean $\pm$ standard deviation): $E = 0.395 \pm 0.142\ MPa$, $\xi = 0.188 \pm 0.131\ MPa$, and $k = 3.668 \pm 1.362\ 10^{-3} mm^4/Ns$. The results are presented in Table 4.1 along with other results taken from the literature, indentation testes performed on bovine cartilage, for the purpose of comparison.

Table 4.1: The mean and standard deviation of the estimated material properties of bovine cartilage in the current study compared to others from the literature.

	Material properties		
	Aggregate modulus (MPa)	Fiber modulus (MPa)	Permeability ($10^{-3}mm^4/Ns$)
Current Study	0.395$\pm$ 0.154	0.188 $\pm$ 0.141	3.668 $\pm$ 1.471
(Moore and Burris, 2015)	0.48 $\pm$ 0.14	3.4 $\pm$ 1.0*	3.8 $\pm$ 3.3
(Chen et al., 2016)	0.415 $\pm$ 0.248	0.288 $\pm$ 0.209	5.041 $\pm$ 2.154

*: The reported value is different from the fiber modulus (ξ) in FE model.

Discussion

The estimated material properties from the creep tests were all within the typical range of adult bovine stifle joint cartilage (Moore and Burris, 2015; Chen et al., 2016). The data obtained from Chen et al. (2016) creep tests were also best-fit to the same fibril reinforced finite elemnt model using FEBio; thus, comparison can be directly performed. As can be seen in Table 4.1, the estimated aggregate and fiber moduli were lower than the result of Chen et al. (2016) by 4.8% and 34.7%, respectively. The estimated permeability was also lower by 27.2%. It is important to note that experimental data used by Chen et al. (2016) was obtained from creep tests performed on cartilage samples harvested from bovine femoral condyle which is known to exhibit compressive and tensile properties that are higher than those of the tibia (Arokoski et al., 1999; Laasanen et al., 2003). In addition, experiments of Chen et al. (2016) were also performed using a porous flat indenter which could affect the estimated permeability.

Therefore, properties obtained using this apparatus were closer to the results of Moore and Burris (2015) in which they characterized the material properties of cartilage harvested form bovine tibial plateau. Aggregate modulus and permeability differed by 17.7% and 3.5%, respectively. Since Moore and Burris (2015) fit their experimental results to an analytical solution, their reported value for the tensile modulus is different from fiber modulus ξ obtained by FEBio continuous fiber distribution models. Hence, to compare the tensile modulus obtained from this study to the tensile modulus of Moore and Burris (2015), tensile test FE simulation was performed on biphasic bar modeled using the estimated material properties from the creep test. Maximum 5% strain was linearly applied to one end of the bar over ramp duration of 2 s while the other end was fixed. The tensile modulus was taken as the slope of the stress-strain curve (Figure 4.4).
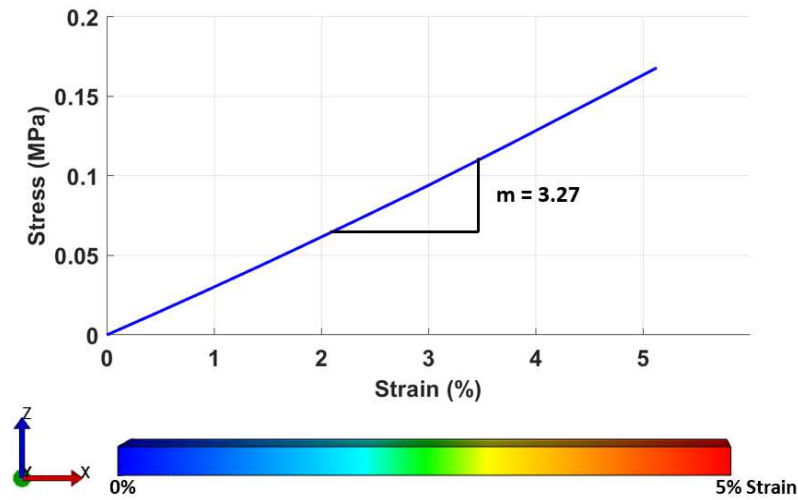
Figure 4.4: Stress-strain diagram produced from finite element tensile testing performed using material properties extracted in this study (Table 4.1.

Interestingly, tensile modulus resulted from FE simulation of the tensile test was 3.27 MPa which is only 3.9% lower than that of Moore and Burris (2015). Due to the well-known site-dependence cartilage biomechanical properties, the differences between the current results and the results of Moore and Burris (2015) are within expected experimental error and biological variability (Athanasiou et al., 1994; Froimson et al., 1997). Furthermore, the apparatus was found to be very repeatable, given the small standard deviation in all measured parameters regardless of the small sample size (n=7). That could be mainly due to the simplified design of the apparatus. The fact that only one parameter, the contact depth, is measured in the experiment, reduces the error margin to minimum and thus increases the accuracy of the results. In most of creep test, the measurement of both contact depth and the applied force are required.

4.1.2 Fluid Load-Support Measurement

As mentioned earlier in Chapter 2, the cartilage behaviour under dynamic load-
ing that involves sliding with migrating contact area is completely different from
that under static loading or dynamic with stationary contact area. That is mainly
attributed to the high interstitial fluid pressurization maintained over time due
to a migrating contact area. Previous experimental studies have shown that high
fluid load support, nearly 90%, is present when a spherical-end indenter was slid
over the cartilage surface at sliding speeds in the range of 0.5-10 mm/s, see Table
3.2. Hence, similar experiments will be conducted to examine the apparatus func-
tion under dynamic loading conditions by measuring the fluid load support at the
cartilage surface of the bovine osteochondral plugs used to estimate the material
properties in Section 4.1.1.

After the creep test was completed, the flat-end indenter was replaced with a
4.75 *mm* diameter spherical-end indenter to perform a sliding test in order to as-
sess the fluid load support in each sample as previously described in Section 3.2.
After a recovery time of 30 minutes, the sample was statically loaded for period
of 30 min to determine the static equilibrium contact depth (δ_s). Based on the first
test, the time required for samples to reach equilibrium under static loading was
in the range of 30 min. Hence, 0.275 N load was applied to the cartilage surface
using the spherical-end indenter and held constant during the entire test. The test
protocol consisted of pure indentation-compression with a constant load of 0.275
N for 1800 *s* followed by reciprocating sliding motion with a triangular wave for
a distance of ±3 *mm* at 1 *mm/s*. The sliding motion was continued for 15 min-
utes at which dynamic equilibrium should be reached. Using the optical encoders,
the indenter vertical and horizontal displacements were recorded during the test.
Hence, the indenter contact depth could be extracted after each sliding cycle at

the initial contact location. The test was repeated at sliding speed of 3 mm/s after another recovery period of 30 min. The fluid load support during sliding was estimated using Equation 3.5 and the results were compared with the results from the literature (Bonnevie et al., 2011; Moore and Burris, 2014). The cartilage layer thickness of each specimen was measured using the uniaxial compression device by means of needle penetration test at the specimen center. Thickness measurement was performed after sliding tests are completed to avoid any possible effect from tissue damage caused by needle penetration. Such effect is very likely since tissue deformation is evaluated at the same location of the needle penetration test.

Using FEBio (Maas et al., 2012), finite element analysis was performed to reproduce the cartilage response to sliding contact using specimen-specific models. Due to high computation cost of the sliding contact analysis, only two specimens were modelled. Specimen-specific geometry and material properties were modeled using preprocessor PreView. A rigid spherical-end indenter of 4.75 mm diameter was made to slide over the specimen surface. Cartilage tissue was modelled using fibril reinforced biphasic model with constant permeability. The subchondral bone was not considered in the model. Due to symmetry, half of the problem was modelled. The fibrils part of the model was modelled using spherical continuous fiber distribution (Ateshian et al., 2009), while the ground matrix was modelled as a Neo-Hookean hyper-elastic that is governed by Young's modulus E and Poisson's ratio ν.

The bottom side of the cartilage sample was fixed in all directions and no fluid flow was permitted out of this side to mimic the fixation of the cartilage to the impermeable subchondral bone. A free draining condition was imposed on the lateral peripheries and no flow was permitted across the plane of symmetry. Contact dependent flow condition was imposed at the specimen surface by a frictionless

biphasic contact, sliding-2 in FEBio, which accounts for sliding and large deformation (Ateshian et al., 2010). As in the experimental procedure, the tissue underwent pure compression period of 1800 s followed by sliding contact for 500 s, sliding speed 1 *mm/s* and sliding distance of ±3 *mm* while a load of 0.275 *N* was kept constant. The fluid load support, predicted by FE models, was calculated by integrating the fluid pressure over the contact area and the fluid load support ratio is given by $\frac{W^p}{W}$, where W is the applied load (Krishnan et al., 2004).

Since the indenter used in sliding test differs from that used in creep test, cartilage response and the estimated material properties will also vary (Korhonen et al., 2002; Simha et al., 2007). Hence, the material properties of each specimen were extracted by fitting the cartilage response during pure compression period, the first 1800 seconds, to fibril reinforced biphasic model similar to Section 4.1.1. The estimated material properties were then used for sliding contact models. However, another simulation was performed using martial properties estimated from flat-end indenter.

Results

The average fluid load support measured in all 7 samples was 87.7% and 89.4% at sliding speeds of 1 *mm/s* and 3 *mm/s*, respectively. Results are presented in Table 4.2 along with results from (Moore and Burris, 2014) for comparison.

Table 4.2: The fluid load support determined in bovine tibial cartilage in the current study compared to Moore and Burris (2014).

	Sliding Speed	
	1 (mm/s)	3 (mm/s)
Current Study	87.7%	89.4%
(Moore and Burris, 2014)	83.5%	84.8%

The tissue recovery, measured experimentally, averaged around 80% after 600s of sliding. However, the tissue recovery predicted by specimen-specific finite element models by the end of simulation was around 52% in both FE models, See Figure 4.5. The fluid load support predicted by specimen-specific FE models by the end of simulation was 95%. The fluid load support in the same specimen that was estimated experimentally was around 88%, as shown in Figure 4.6.
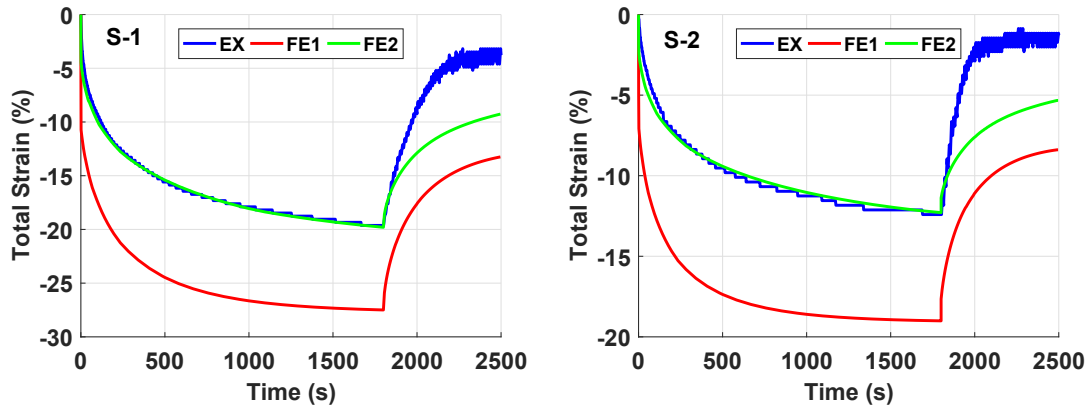
Figure 4.5: Illustration of the articular cartilage response from two specimens (S-1 and S-2) to sliding contact experimentally (EX) and by specimen-specific FE models using material properties from creep response to flat-end indenter (FE1) and spherical-end indenter (FE2).
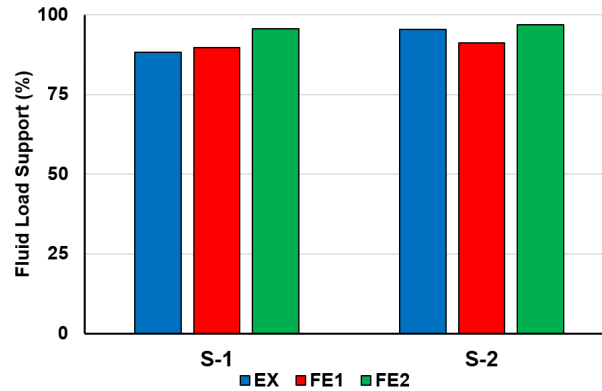
Figure 4.6: Fluid load support assessed experimentally using Equation 3.5 and by specimen-specific FE models at the end of simulation.

The estimated material properties extracted from fitting the pure compression curve of the spherical indenter resulted in higher Young's modulus (E) by 55% while the fibril modulus (ζ) was one order of magnitude higher and the predicted permeability (k) was one order of magnitude lower that those of the flat-end indenter. Material properties of the two specimens are presented in Table 4.3.

Table 4.3: Best-fit material properties of two bovine articular cartilage specimens predicted from best-fit of creep curve obtained using different indenter geometries.

Specimen	Indenter	$E\ (MPa)$	$\zeta\ (MPa)$	$k\ (10^{-3}mm^4/Ns)$
S-1	Flat-end	0.32	0.08	3.12
	Spherical-end	0.46	0.7	0.55
S-2	Flat-end	0.57	0.17	1.5
	Spherical-end	0.95	2.0	0.16

Discussion

Results obtained from sliding experiments clearly demonstrated the apparatus capability of measuring the cartilage response to dynamic loading. Measurements of the indenter's vertical and horizontal positions, over time, allowed for monitoring tissue deformation at any chosen location along the indenter travel path. At the center of contact, the location of maximum static deformation, the tissue recovery during sliding was captured with a great accuracy. That enabled measurement of the fluid load support at the center of contact below the indenter, using Equation 3.5. The fluid load support measured at dynamic equilibrium was in the range of 85%, in agreement with previous study of Moore and Burris (2015). Also, higher fluid load support was measured at higher sliding speed.

This experiment also allowed for measurement of the time required for tissue

recovery from static to dynamic deformation. Interestingly, the time required for the tissue to reach dynamic equilibrium, the recovery time, was relatively short (1/3 of static loading time) and at the same range in all specimens. To the best of our knowledge, this is the first reported in-situ measurements of tissue recovery time from static to dynamic deformation using a load-controlled device. Bonnevie et al. (2011) have observed similar behavior; however, the device used in their experiment, stress-relaxation, and the amount of the applied strain, 50 *μm*, did not allow for measurement of this recovery time. Therefore, since the synovial joints, *in vivo*, effectively function under load-controlled condition during normal activities (Bergmann et al., 2001), results obtained from the current apparatus are more relevant to physiological conditions.

Moreover, this study provided the numerical assessment of the fluid load support measurement at the bearing surfaces of the synovial joints using specimen-specific FE models. Estimating the material properties from the creep data of the spherical-end indenter resulted in higher stiffness and lower permeability compared to properties estimated using flat-end indenter in Section 4.1.1. That is mainly attributed to simplified fibril reinforced finite element model, used to estimate the material properties and the uniform modulus of the non-fibrillar (PG) component with depth.

Normally, in engineering materials, the increase in contact area with spherical-end indenter correlates with the increase in contact depth, in indentation test. That results in faster tissue deformation, early in the test, due to smaller contact area compared to flat-end indenter. Therefore, spherical-end indenter induces larger total tissue deformation compared to flat-end indenter. However, in cartilage, experimentally, the contact area with spherical-end indenter, increases very quickly due to the low stiffness of the most top layer of articular cartilage (Teshima et al.,

1995; Fujioka et al., 2013). That slows down the deformation rate, see Figure 4.7. Since the fibril reinforced model used to fit the material properties does not reproduce the behavior of this very thin surface layer, the increased stiffness and the low permeability compensated for the smaller contact area in FE model and hence slow down the deformation rate.
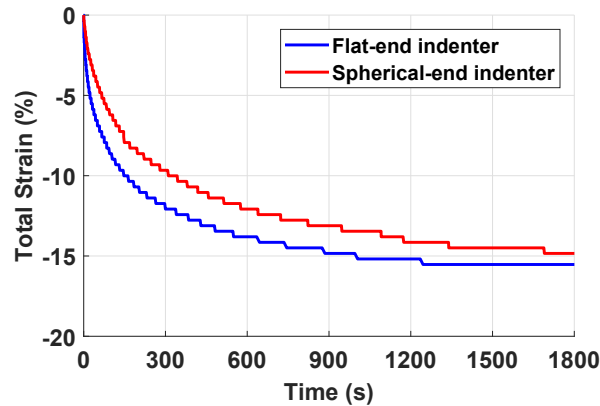
Figure 4.7: Cartilage creep response to step-wise 0.275 N load applied using spherical-end indenter ($D = 4.75\ mm$) and flat -end indenter ($D = 1.8\ mm$).

Nevertheless, the homogeneous fibril reinforced biphasic model reproduced the articular cartilage response to sliding to some degree. The results showed that the duration of sliding simulation (500 s) was not sufficient for the tissue to achieve dynamic equilibrium as it was the case experimentally. However, the predicted fluid load support as the ratio of the fluid pressure to the contact pressure was slightly higher than that measured experimentally, although the tissue recovery was much slower. That clearly indicates the contribution of other parameters, e.g. osmotic and swelling properties caused by fixed charge density, to dynamic cartilage function. The negatively charged proteoglycans cause an imbalance between interstitial and the external fluid which gives the articular cartilage the ability to imbibe water from the outside medium during unloading cycle (Lu and Mow,

2008; Han et al., 2011). Donnan osmotic pressure is thought to contribute to tissue's equilibrium stiffness by 30-50% (Flahiff et al., 2002) which should accelerate the recovery process. Hence, more sophisticated finite element model (e.g. triphasic theory (Lai et al., 1991)) are required to account for Donnan osmotic pressure effects.

4.1.3 Cartilage Thickness Measurement

In this section, the goal is to demonstrate how uniaxial displacement-controlled device was used to measure the thickness of an actual cartilage specimen. An osteochondral plug was cut from the bovine tibial plateau, obtained from freshly slaughtered 2.5 years old cow, as described in Appendix A. Needle penetration test was performed as described in Section 3.5.3, and the resultant reaction force was plotted against the needle displacement (Figure 4.8).
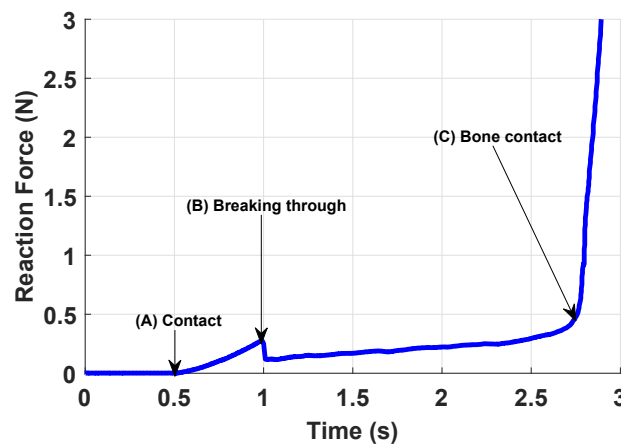
Figure 4.8: Cartilage thickness determined by needle penetration test.

As can be seen from Figure 4.8, no change in reaction force was detected early in the test. That represents the distance the needle travels before making its contact with cartilage surface. Upon contact, marked by increase in reaction force for more

than 10 mN, Point (A), the reaction force slowly continues to rise, by 1 mN/μm, as the needle deforms the cartilage surface. The force suddenly drops marking the Point (B) where the needle breaks through the cartilage surface and the reaction force begins to rise again as the needle makes its way through the cartilage matrix. Finally, a sharp rise in the force response by more than 10 mN/μm is detected which indicates that subchondral bone plate has been reached, Point (C).

The cartilage thickness is then determined by computing the difference between the two points A and C. However, the slow increase in the reaction force around point C indicates the region of calcified cartilage. The thickness of the calcified cartilage region is known to correlate with the thickness of the above cartilage layer (Müller-Gerbl et al., 1987). Hence calcified cartilage zone thickness can be approximated based on the first estimate of the total cartilage thickness. Finally, the cartilage thickness systematically varies between joints and across the same articular surface (Li et al., 2005). Hence, knowing the anatomical position of the specimen is important to trust the measurement is within the typical range.

4.2   Conclusions and Limitations

In this thesis, two cost-effective testing devices were developed to be utilized for biomechanical as well as mechanobiological research on cartilage explants. Given the results obtained from both static and dynamic tests, clearly demonstrate that the apparatus are extremely repeatable and sufficiently accurate. Hence, with high level of confidence, both devices can be used to perform biomechanical as well as mechanobiological experiments on cartilage explants. However, number of limitations should be noted that could be overcome in future.

First, both devices are now designed to process a single specimen at a time

which might be a big limitation, especially in mechanobiological testing. While processing multiple specimens, simultaneously, is good for preserving test conditions and saving time, it might be difficult to perform due to many other reasons other than device capability. The main reason for developing both devices was to test the effect of sliding contact on cartilage mechanobiology. Hence a device was required that allowed a sliding distance in the physiological range. However, the number of specimens that can be harvested from one joint at the size required for sliding tests will be limited by the joint size. Large joints, e.g. tibia femoral joint, may give the possibility for obtaining more than one specimen from the same surface; however, variations in thickness and material properties between specimens are still expected (Athanasiou et al., 1994; Froimson et al., 1997).

On the other hand, due to variations in cartilage thickness, the amount of strain applied will be different in each specimen in displacement-controlled uniaxial cyclic compression. Researchers usually work around that by cutting specimens in equal thicknesses which may compromise the biomechanical properties of the tissue (Ruggiero et al., 2015) which could severely affect chondrocytes mechanical environment. In fact, in our opinion, that could be a huge drawback to the use of displacement-controlled loading mode in cartilage mechanobiological testing.

However, both devices can be modified to process a few more samples by adding the required number of compression tools and specimen baths. For example, a few baths and indenters can be added in linear pattern on both sides of the ball-screw in mobile loading device. Similarly, specimen baths and compression platen can be added in circular pattern to the uniaxial loading apparatus.

Another limitation could be the low resolution of used displacement sensors used in both devices, 3.175 μm. This resolution is very good for cartilage thickness measurement as it represents about 0.15% of cartilage thickness, estimated at 2 mm.

However this resolution may be low for cartilage deformation measurement, 1.5% for typical cartilage deformation, 10%, during creep or stress relaxation tests. This can be improved in future by using encoders with higher resolutions or LVDTs.

There were a few other limitations concerning finite element models used to estimate the material properties and the fluid load support. Although the used fibril reinforced models result in anisotropic (or transversely isotropic) behaviour as soon as deformation occurs, three-layer structured fiber models similar to the model of Chapter 2 with depth- dependent compressive stiffness (Wilson et al., 2007; Shirazi et al., 2008) would be more realistic. Also, models used constant permeability although the compressive strain turned out to be in the range of 20%. The effect of these parameters on the accuracy of the model could be studied in future studies. However, for this study, simplifications were necessary to reduce the number of optimized parameters.

Finally, samples were frozen before testing which may cause formation of ice crystals within tissue may disrupt the protein network of the ECM. However, a single freeze thaw cycle does not substantially affect the measured properties as it was shown by Changoor et al. (2010).

Chapter 5

AC Mechanobiological Response to Sliding

5.1 Introduction

Articular cartilage structure and composition are maintained through a constant remodeling process that is regulated by chondrocytes. Chondrocytes function, in turn, is influenced by the expression level of various mediators such as cytokines, growth factors, matrix metalloproteinases (MMPs), tissue inhibitor of metalloproteases (TIMPs), and aggrecanase (Goldring and Marcu, 2009). Low levels of most of these mediators are present in normal cartilage and required for normal synthetic and degenerative activity. In healthy tissue there is a balance between anabolic (tissue synthesis) and catabolic (tissue destruction) activity. During OA, however, the expression level of these mediators shifts toward the degenerative activities which accelerates the tissue matrix destruction.

Some of these mediators such as interleukin (IL)-6 and IL-1α are considered catabolic while others such as bone morphogenetic protein (BMP-2) and transforming growth factor (TGF)-β belong to the list of anabolic factors (Goldring, 2000). At the cellular level, binding of a catabolic cytokine to a cell receptor can induce the production of proteinases such as MMPs that destroy the tissue ECM.

On the other hand, interaction with growth factors may induce production of ECM components. The specific effect on the cell can depend on the presence of other cytokines, growth factors or metabolic mediators. Hence, cartilage matrix degradation is linked to imbalance in MMPs and TIMPs. MMP-1 and MMP-13, for example, are involved in type II collagen cleavage while MMP-3 was linked to degradation of aggrecan (Nicodemus and Bryant, 2010). Increased level of MMPs is usually associated with increased level of TIMPs as an attempt to block cartilage destruction (Goldring, 2000; Goldring and Goldring, 2004). Table 5.1 presents the classification of cytokines and growth factors based on their role in cartilage metabolism.

Table 5.1: Cytokines involved in cartilage metabolism as classified by Goldring (2000).

Catabolic	Regulatory	Inhibitory	Anabolic
IL-1β	IL-6, 8	IL-4, 10, 11, 13	IGF-1
TNF-α	LIF	IL-1ra	TGF-β1, 2, 3
IL-17, 18	OSM	IFN-γ	FGF-2, 4, 8
			BMP-2, 4, 6, 7, 9, 13

The synthesis of catabolic or anabolic mediators by the chondrocytes is influenced by many factors that are related directly or indirectly to their biochemical and biomechanical microenvironment. Factors produced by the synovial lining cells or the subchondral bone could alter the chondrocytes production of certain catabolic enzymes. For example, transforming growth factor (TGF)-β produced by cells in subchondral bone could induce the synthesis of matrix proteins by the chondrocytes. This migration of signals across tissue boundaries is known as crosstalk and is becoming an active area of research, especially in peri-articular tissues.

The mechanical microenvironment of the chondrocytes is also thought to have

a great effect on chondrocyte function and cartilage metabolism. The ability of chondrocytes to alter their metabolic activities in response to changes in their micromechanical environment has long been recognized (Sah et al., 1989). A great number of *in vitro* studies were carried out to investigate the chondrocytes response to mechanical loads on the cartilage surface using different loading regime, magnitudes, and frequencies (Grodzinsky et al., 2000; Julkunen et al., 2013).

In contrast to static compression (Kim et al., 1994; Wong et al., 1997), dynamic uniaxial compression resulted in up-regulating the synthesis of cartilage matrix proteins, mainly proteoglycan (Buschmann et al., 1999; Jeon et al., 2012). Therefore, this loading regime was extensively used in mechanobiological testing of cartilage as discussed in Section 3.1 and listed in Table 3.1 . Interestingly, most of *in vitro* mechanobiological experiments of cyclic compression have reported upregulating in matrix proteins, although various load magnitude and frequencies were employed. That could mean the employed loading conditions are far from realistic as the production and remodeling of the matrix components is very low in physiological conditions (Maroudas et al., 1998; Verzijl et al., 2000).

Moreover, tribological studies on cartilage have shown that unconfined cyclic compression failed to maintain high fluid load support, the well-accepted lubrication mechanism for synovial joints. The fluid load support mechanism in articular cartilage depends on migrating contact area as it was confirmed by many tribological studies (Ateshian and Wang, 1995; Pawaskar et al., 2007; Caligaris and Ateshian, 2008; Bonnevie et al., 2011).

In the first study of this thesis, Chapter 2, we have shown that the fluid flow in uniaxial cyclic compression was limited to regions near the radial peripheries but decreased over time. On the other hand, sliding loading, that involves sliding with migrating contact area, could alter cartilage biomechanical response compared to

uniaxial loading. In this loading regime, constant fluid pressure and tissue strains were maintained during the entire simulation and tissue consolidation was much lower compared to uniaxial cyclic loading. That was also supported by experimental study, Section 4.1.2, where sliding resulted in deformation recovery after creep due to increased interstitial fluid pressure. Furthermore, high and continuous fluid exudation and imbibition were provided through the specimen surface reaching the mid zone of the tissue in sliding loading regime. That could be vital for cartilage metabolism since the cartilage lacks vascular network and depends on mass transport enhanced by fluid flow for oxygen and nutrition supply.

Therefore, it is hypothesized that loading protocol that promotes migrating contact area will induce a different metabolic profile than uniaxial loading with static contact area. Therefore, the goal of this study was to assess chondrocyte metabolism under such loading profiles and compare the resultant levels of various cytokines, growth factors, and TIMPs to unconfined uni-axial cyclic compression.

5.2 Experimental Procedures

5.2.1 Cartilage Explantation

Osteochondral samples were cut out of femoral heads taken from patients undergoing total hip arthroplasty due to femoral neck fracture (FNF) or osteoarthritis at the Ottawa General Hospital. The study was reviewed and cleared by both the Ottawa Hospital and Carleton University Research Ethics Boards. Samples were obtained from 9 femoral heads (3 OA and 6 FNF). If not processed immediately, samples were kept refrigerated until they are tested on the following day. In all

cases, samples were collected right after the surgery and tested "fresh" within 24 hours of the surgery time. Specimen donor demographics are presented in Table 5.2.

Table 5.2: Specimen donor demographics.

Group	Specimens	Age (mean, range)	Gender (M:F)
FNF	6	70.0 (60,77)	2:4
OA	3	63.3 (43, 90)	1:2

On the day of the test, samples were washed using PBS solution and the cartilage layer with most of the thickness was carefully removed off the subchondral bone using a surgical scalpel. Then, a single use biopsy-punch was used to harvest cylindrical cartilage disks of 10 mm of diameter, (Figure 5.1). The cartilage layer thickness was measured by means of electronic digital caliper (Glowgeek, Shenzhen Sunyuan Technology Co. Ltd, Shenzhen, China) at four points on the radial periphery.
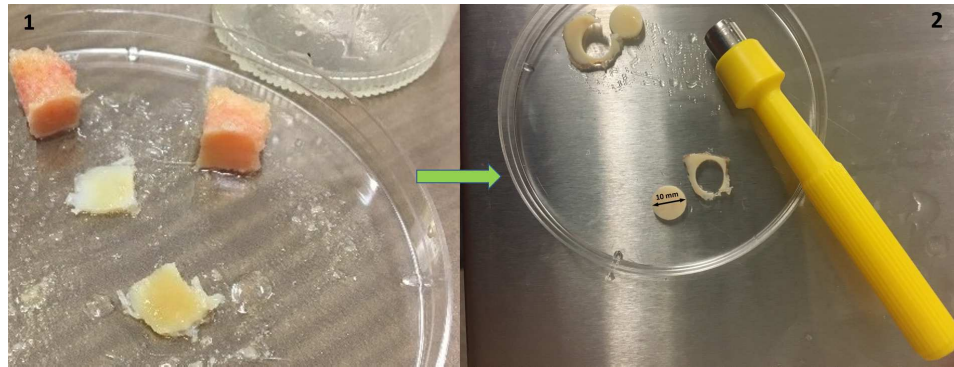
Figure 5.1: Samples preparation procedure. 1: Slicing the cartilage layer off the bone. 2: Cutting out the cylindrical disks using biopsy-punch ($D = 10\ mm$).

From each femoral head sample, four specimens were obtained for each specimen to be subjected to different loading environment. Thus, the obtained specimens were divided into four groups (A, B, C, and D). Group A specimens were immediately frozen at -80°C using liquid nitrogen (Kiefer et al., 1989). This group resembles the biological state of the tissue at the time of the surgery and were Labelled "Fresh". Specimens of Group B were submerged in culture media and left unloaded in a small vial in a free swelling condition and were Labelled "Control". The other two groups, C and D, were subjected to different types of mechanical loading. Group C specimens were loaded using typical unconfined cyclic compression whereas specimens of group D were subjected to sliding loading that permits migrating the contact area as illustrated in Figure 5.2. The last two groups, C and D, were Labelled "Cyclic" and 'Sliding", respectively.

During testing specimens were submerged in low glucose Dulbecco's modified essential medium supplemented with 10% fetal bovine serum, 10 mM Hepes buffer, 0.1 mM nonessential amino acids, 20 μg/ml ascorbate, 100 units/ml penicillin, 100 μg/ml streptomycin, and 0.25 μg/ml amphotericin (Fitzgerald et al., 2006).
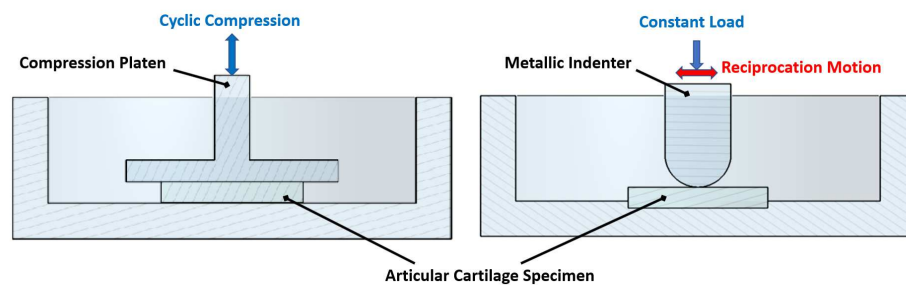
Figure 5.2: Illustration of the two loading protocols, note the circular indentation in the sliding loading (Right).

5.2.2 Mechanical Loading

For detailed description of the devices used for the two types of loading, please refer to Chapter 3. However, a small change was made to the sliding apparatus as the experiments were performed on cartilage disks without the subchondral bone layer, it was not possible to use the specimen clamp described in Section 3.3.1. Therefore, a small specimen bath with circular indentation at the center, shown in Figure 5.3, was made to host the cartilage disk during sliding testing mode. The circular indentation has a diameter of 10 *mm* and depth of $\sim$ 0.5 *mm*; hence, prevents the cartilage disk movement in the lateral direction during sliding test.
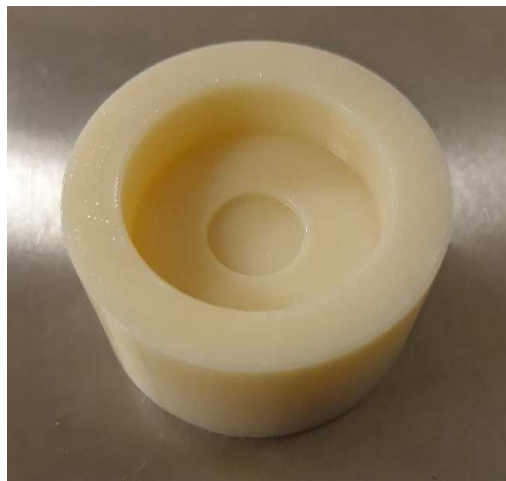
Figure 5.3: Container that host the cartilage disk during sliding loading experiment.

Displacement-controlled unconfined cyclic strain was applied to the cartilage specimen using micro-stepper motor. To ensure contact, the compression platen was slowly lowered until contact is detected by change in the reaction force measured by the load cell. The specimen was then allowed to equilibrate, for period of 20 min, before 10% axial dynamic strain was superimposed. The intermittent dynamic strain was applied using haversine waveform (0.5 *Hz*, 40% duty cycle) (Li et al., 2013).

As for the sliding contact experiments, a constant load of 0.5 N was applied to the articular cartilage specimens using spherical-end stainless steel indenter, sphere diameter is 4.75 mm. The indenter was slowly lowered and let to freely set on the cartilage surface. Upon contact, the indenter was commanded to slide back and forth over the cartilage surface at 5 mm/s over a stroke length of 6 mm. Both mechanical tests were intermittent in which the tissue was continuously loaded for 1 hour, sliding or uni-axial loading, followed by 5 hours of rest. Experiments were performed in room temperature and continued for 48 hours (Li et al., 2013). After the completion of 48 hours testing period, cartilage disks were removed from the culture media and frozen at -80°C before metabolic analysis is performed.

5.2.3 Chondrocyte's Molecular Signals Measurement

The procedure described in this section was performed at The Storey Lab, Department of Biology, Carleton University by Christine Lynn Childers.

The Millipore Magnetic Cytokines/Chemokines HCYTOMAG-60K-12C kit (R&D Systems) was used to measure expression levels of multiple cytokines in the interleukin family and growth factors (IL-1α, IL-Ira, (IL-4, 6, 10, 18) CCL2/ MCP-1, CCL7/ MCP-3, and VEGF-A). A Human TIMP Magnetic Luminex Assay (R&D Systems: LKTM003) was used to measure four TIMPs: TIMP1, TIMP2, TIMP3, TIMP4. Human Magnetic Luminex Performance Assay Base Kit, MMP Panel (R&D Systems: LMPM000) (MMP-1, MMP-3, MMP-9, MMP-13). In addition, the expression of the growth factors (BMP-2 and TGF-β) was assessed using Enzyme-Linked Immunosorbent Assay (ELISA; Abcam).

The frozen cartilage specimens were homogenized using 1X lysis buffer (EMD Millipore; 43–045) with a 1:3 (w/v) ratio using a Polytron 1200 homogenizer. Homogenates were then subjected to intermittent vortexing (every 10 min) at room

temperature with a 10 second sonication performed after the second vortex to maximize cell lysis. The samples were then centrifuged at 14,000$\times g$ for 30 min at 4 °C and the soluble liquid layer, which contains the soluble proteins, was collected and frozen at -80 °C until use. For the Cytokines/Chemokines, TIMP and MMP kits were performed as per the manufacturer's instructions with 30 μg, 25 μg and 25 μg of protein was loaded with 50 mul of their respective microparticles.

The assays are conducted in 96-well microplate in which up to 100 different targets can be measured in each well. Each well contained the extracted soluble protein from one specimen, representing a unique combination of patient and loading mode (Fresh, Cyclic, Sliding, Control). Expression levels of each target are measured by fluorescence in the reaction mixture from the wells using a Luminex 100/200 and associated software (Luminex Corp). Magnetic beads will attach to specific analytes (e.g. TIMP-1, TIMP-2) through an attached antibody; another antibody attaches to the analyte with Streptavidin-PE (Phycoerythrin is a fluorophore often used in flow cytometry). Two LEDs with distinct wavelengths are used: one identifies which analyte is being measured, the other excites the fluorophore. The fluorophore emission intensity is measured as the fluorescence index and the median Fluorescence Index (MFI) was measured from each well and the background MFI measured from an empty well was subtracted.

To account for inter-patient variability, the relative target levels were calculated from the background-subtracted MFI, normalized by the MFI of the control sample. This relative target level was used to assess changes in target levels due to loading mode. Any value of the background-subtracted MFI below 1.0 was considered to be below the detectable limit and the measurement of the target from the corresponding patient was omitted.

5.2.4 Statistical Analysis

Since Control, Cyclic, and Sliding specimens were available from each patient, paired t-tests were performed on the normalized MFI values to test differences in target levels due to the loading mode. The number of specimens was too low to conduct an omnibus multivariate analysis of variance.

5.3 Results

Among the total of 10 soluble mediators measured in both FNF and OA cartilage tissues, TNF-α, IL-10, and IL-18 were below the detectable range in both FNF and OA specimens. In addition, CCL7/MCP-3 was below the detectable range in OA specimens. All other detectable cytockines in all specimens are presented in Figure 5.4, by their relative expression normalized to control specimens.

In all specimens, the level of all detectable cytockines was relatively lower in specimen subjected to sliding contact. However, a pair t-test of all specimens showed that only one target was significantly different, CCL7 ($p < 0.05$ marked by **) while another approached significance, IL-1α ($p < 0.1$ marked by *). Sliding contact loading mode also resulted in lower expression level of TIMPs compared to uniaxial contact mode. However, they were not statistically significantly different (Figure 5.5). Measured cytokines and TIMP in FNF and OA separately are provided in Appendix A.
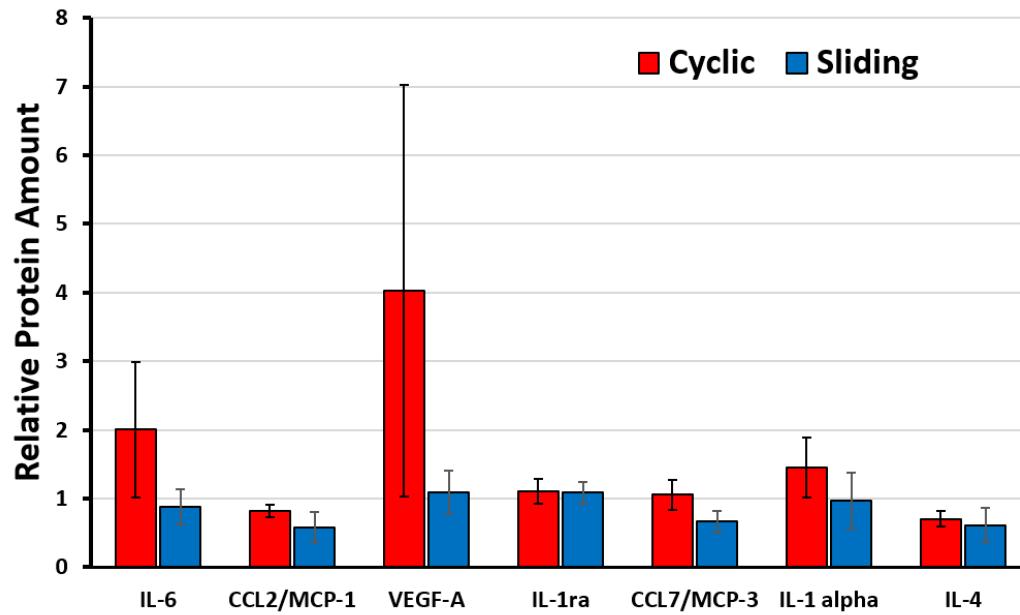
Figure 5.4: The relative level of cytokines in all specimens, normalized to control specimens. The mean of levels of each target is represented by colored bars while the error bars are the standard errors.
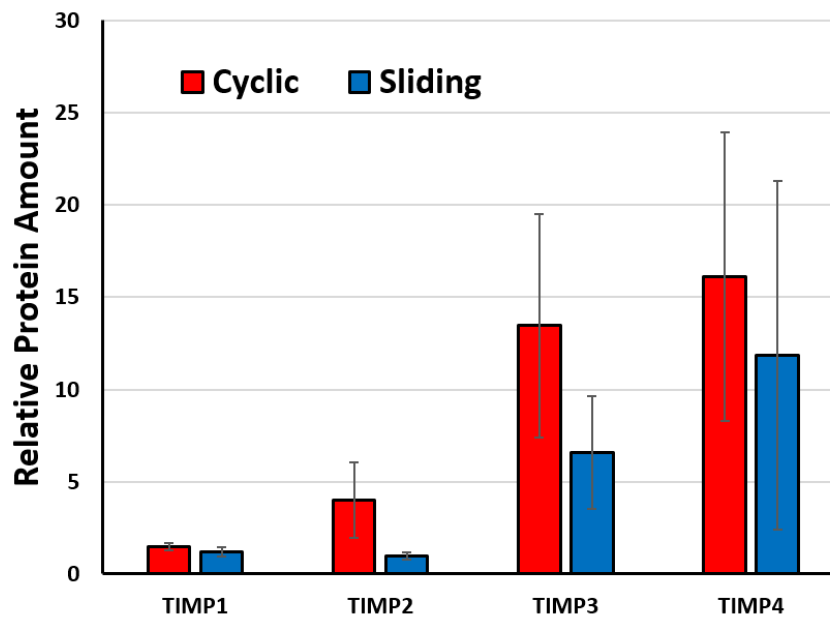
Figure 5.5: Normalized to control, the relative level of TIMPs in all specimens.

The level of TGF-β in all samples was significantly greater ($p < 0.05$) in sliding loading mode. Interestingly, the differences appear to be larger in the OA than the healthy (Figure 5.6); however, there were insufficient specimens to test this statistically.. There was only (n=3) samples left with enough soluble protein to run measure BMP-2 level which seemed larger in sliding mode. Results are not shown due to extremely low number of specimens.
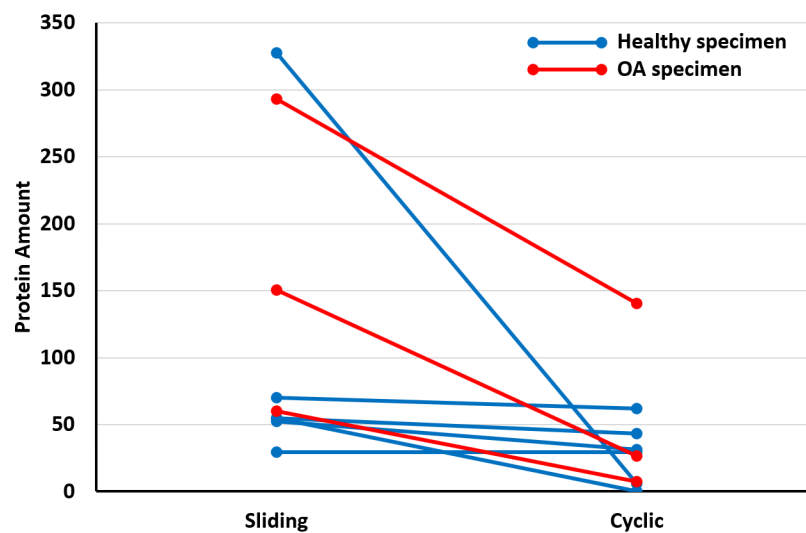
Figure 5.6: TGF-β Protein amount in all (n = 9) specimens in sliding and cyclic compression modes.

5.4   Discussion

In this study, two loading modes were applied to surgically-retrieved cartilage specimens and the levels of number of cytokines and growth factors were measured. Results obtained from this study suggest that the loading modes, using equal amount of strain/stress, does have an effect of the level of biochemical signals in cartilage explants. It seems that uniaxial compression, although at low strain, increased catabolic activities compared to sliding contact. The increased

level of expression of TIMPs in uniaxial cyclic compression could be due to increased expression of MMPs. However, our results are not statistically significant, likely due to low specimen numbers. The effect of sliding contact loading mode seemed to be more obvious on the level of growth factors (TGF-β and BMP-2) which were significantly greater in specimens subjected to sliding compared to uniaxial compression. It should also be noted that difference appeared to be larger in OA specimen compared to healthy specimens.

There was a number of difficulties encountered during this experiment which affected the obtained results. Given the low number of specimens (n = 9), limitations of this study are primarily statistical. It is possible that the difference in the protein level of the targets of interest measured in this study was affected by other factors aside from the loading protocol which would constitute a type I error.

Healthy specimens were obtained from subjects who suffered femoral neck fracture in which case the surgery was performed within a very short time. That made the patient's recruitment process and communication with the surgeon very complicated. Besides, the FNF specimens that were collected successfully, have come from older patients, mean age of 70.0 years. This could affect the measured level of biochemical signals as the chondrocytes are known to exhibit an age-related decline in their metabolic activities (Loeser, 2009).

OA specimens, on the other hand, were more accessible and easier to obtain, since they were retrieved from patients undergoing hip replacement surgery for OA. However, most of the received specimens were severely degenerated and not testable. That was expected as OA is radiographically diagnosed by narrowing of the joint space as indication of cartilage degeneration. By the time, joint replacement becomes necessary, most of the cartilage is worn away. Therefore, only 3 samples were obtained which were taken from non-degenerated region of the

femur head, which could also be non-articulating region.

Cartilage is known the exhibit location dependent material properties where the variations are higher between bearing and non-bearing regions (Moore and Burris, 2015). Therefore, difference in mediator's protein levels are expected between samples depending on the specimen anatomical site. While the information of the anatomical locations of the retrieved sample was not available, we assumed that the effect of ECM material properties on targets protein level would be lower compared to the effect of loading protocol, especially that spatial variation of cartilage material properties in hip joint is lower than that in knee joint (Athanasiou et al., 1994; Moore and Burris, 2015). All of the above mentioned limitations could be overcome by enlarging the sample size, which would increase the statistical power and allow for testing the effect of different mechanical parameters such as stress/strain level, sliding speed, strain rate, and duration of the test on gene expression was not studied in this experiment.

As shown in Figure 5.7, the load applied in both loading modes was at the low end of the moderate physiological limits of strain and contact pressure, 10% maximum strain and contact pressure less than 2 MPa. It is well documented that the turnover of the cartilage solid matrix is very low under physiological loading conditions and in the absence of inflammation (Goldring, 2000). Therefore, it might not be surprising that the differences in this experiment were not significant. Perhaps, more aggressive loads or longer duration would produce larger differences between loading modes especially with respect to cytokine levels.
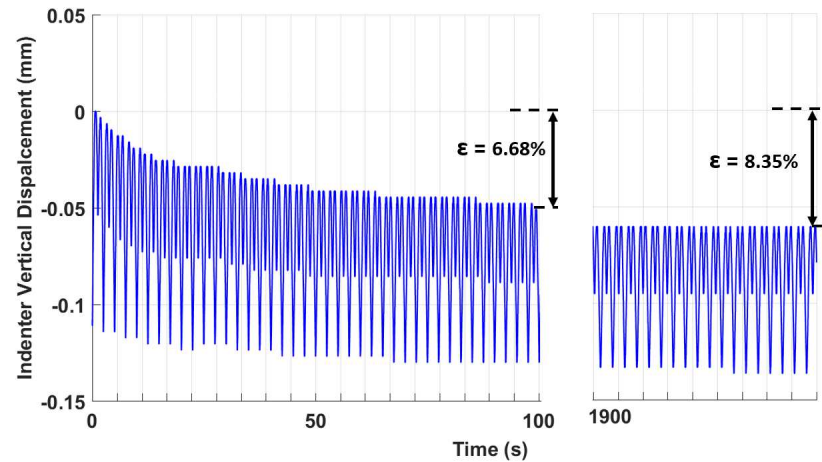
Figure 5.7: Total strain measured at the specimen center measured by the vertical indenter position over time during sliding test.

Further, the biochemical signals studied in this chapter are produced by chondrocytes, but also by other cell in other joint tissues, e.g. lining cell in the synovium. During OA, other joint tissues are also affected which alter the expression level of gene produced by cell of those tissues. In one study that compared the several mediators' profiles in synovial fluid (SF) and articular cartilage from healthy and OA joints showed that most difference were seen in SF, with only one target that was different in AC (Tsuchida et al., 2014). That may suggest that alteration in mediators expressed by chondrocytes alone are hard to measure, especially over short loading duration. Interestingly, significant difference was measured in two mediators in this study and most target levels were reduced compared to the fresh specimens, after only 2 days. Thus, longer testing duration or higher loads may amplify the observed differences.

Moreover, in Chapter 2, it was shown that the two loading modes induced depth-dependent differences in tissue mechanical response. In sliding mode, it was shown that cyclic fluid pressure and tissue strain were mostly localized in the

superficial zone. Chondrocytes in the superficial zone are known to be metabolically more active than chondrocytes in the middle and deep zones (Coates and Fisher, 2014). Furthermore, continuous passive motion in which low contact force is applied promoted the formation of healthy cartilage (Salter et al., 1980) which could suggest that the synthesis of solid matrix proteins is mostly credited to the chondrocytes of the superficial zone.

However, the measured target levels in this experiment were done using soluble protein obtained from cartilage specimen of full thickness; hence, they represent biochemical environment from the full thickness. Measurement target level in each zone will allow for isolating the depth dependence and could provide a better understanding of zonal differences in chondrocyte metabolism (Fukui et al., 2008) and the resulting composition variation. However, that is difficult due to the low amount of soluble protein available in a sample.

Another limitation was the limited number of targets that could be measured based on specimen size. Targets measured in this study were chosen based on those reported in cartilage literature. However, that was constrained by what is available in the multiplex panels and the amount of soluble protein obtained each specimen. Additional targets would be measured e.g. using ELISA if more soluble protein was available.

Nevertheless, in this study, lower levels of most of the cytokines were seen in specimens subjected to sliding compared to axial cyclic loading, although statistical significance was obscured by the low number of specimens. With exception was IL-1ra which appeared similar in both loading modes, the increased expression of other molecules in specimens subjected to cyclic compression, may indicate catabolic activities. For example, IL-6 and IL-1α are classified as major catabolic cytokines. IL-6 is known to downregulate aggrecan and link protein. IL-6 may

also indicate the presence of a very well documented catabolic cytokine (IL-1) (Goldring and Goldring, 2004; Goldring et al., 2008).

Increased expression of chemokines, CCL2 and CCL7 ($p < 0.05$) was also measured in specimens subjected to cyclic compression. Although the main role of these chemokines is not directly linked to catabolic activities, their receptor, CCR2, is strongly involved in IL-6 induced cartilage catabolism (Latourte et al., 2017). Similarly, vascular endothelial growth factor (VEGF) is a key factor in the articular cartilage in human OA (Yamairi et al., 2011). Results also indicated up-regulation of all TIMPs, with a lesser degree for TIMPs 1 and 2, in specimens subjected to cyclic compression compared to sliding. That may indicate increased levels of active MMPs as the TIMPs role is to reduce the MMPs effects (Goldring, 2000).

5.5 Conclusion

Cytokines exert their biological activities as a network and do interact with other enzymes and cytokines that are not necessarily from the same family. That makes concluding information from measuring limited number of targets challenging.

However, the trend seen in the results of this experiment could suggest that uniaxial cyclic compression, even at low strain level, triggered catabolic activity in cartilage. In contrast, sliding reduced the expression of number of mediators that are known effect cartilage metabolism and increased growth factor TGF-β. Hence, future work could examine duration and intensity for both loading modes, as well as optimizing loading protocols for cartilage with mild degeneration that could halt or reverse degeneration, similar to continuous passive motion (Salter et al., 1980).

Chapter 6

Conclusions and Future Directions

6.1 Conclusions

In the last decades, our knowledge of articular cartilage tribological function has been greatly enhanced by many *in vitro* experimental studies, where the relative motion of the articulating surfaces received a great deal of attention. It is now well accepted that high interstitial fluid pressure maintained by relative surface motion is the main lubricating mechanism within the synovial joints. However, mechanobiological studies still employ loading protocols involving uniaxial cyclic compression or sliding with stationary contact area. There have been a few attempts to consider the sliding motion that promotes a migrating contact area; however, knowledge of the state of fluid load support or the coefficient of friction at the bearing surfaces was absent in most of these studies. Therefore, this thesis introduced a more physiological loading protocols that promotes migrating contact area at the bearing surfaces to study the chondrocyte's molecular signals expression under sliding contact loading conditions.

In the first study, finite element analysis has shown that sliding with migrating contact area could maintain high interstitial fluid pressurization for long period

which resulted in low, but physiologically relevant, tissue strains. High fluid flow across the tissues surface, which is required for oxygen and nutrient supply, was also maintained. On the other hand, unconfined cyclic compression, the typical method for mechanobiological *in vitro* testing of cartilage, resulted in continuous tissue consolidation and increased local strains. Fluid flow in cyclic compression mode was limited to regions near the radial peripheries which could lead to radially uniform mechanobiological response in frequency-dependent manner. However, the consolidation rate was greatly reduced by surface curvature, suggesting that surface curvature could play a role in tribological as well as mechanobiological function of cartilage. Hence, these results strongly suggest that incorporating physiological loading conditions could have a great potential for mechanobiological studies on cartilage explants, especially in understanding the *in vivo* chondrocyte environment.

Therefore, two low-cost devices were custom designed and constructed to be utilized for *in vitro* testing of cartilage explants. The first device was a load-controlled indentation with sliding that can apply sliding contact with a migrating contact area. This apparatus gives the possibility of applying physiological contact pressure and measuring the resultant tissue strains and thus the existing fluid load support using various sizes of cartilage explants with or without subchondral the bone layer. The second device was a displacement-controlled device that can perform uniaxial compression (static or dynamic) tests at various strain and strain rates. Both devices can be used for mechanobiological or biomechanical testing of cartilage, e.g. material properties determination and cartilage thickness measurement.

The last chapter of this thesis presents the mechanobiological testing that was

performed on healthy and degenerated cartilage explants using two different loading modes, sliding contact and uniaxial cyclic compression. Various biochemical signals that control the chondrocyte functionality and the articular cartilage metabolism were measured. Lower levels of most of the cytokines were seen in specimens subjected to sliding compared to uniaxial cyclic loading, although statistical significance was obscured by the low number of specimens. The expression level of TIMPs was also increased in specimen subjected to uniaxial cyclic loading compared to sliding. Results obtained from this experiment could indicate the presence of catabolic activities under uniaxial cyclic compression loading mode.

Results obtained from this thesis demonstrate the importance of incorporating realistic loading conditions at the bearing surface in *in vitro* mechanobiological testing of cartilage. The findings of this work should contribute to the ongoing research on the interactions between chondrocyte biosynthetic activities and loading conditions toward developing therapeutic interventions and tissue engineering approaches for cartilage disorders.

6.2 Contributions

This thesis contributed to the ongoing research on cartilage and attempted to bridge the gap between tribological and mechanobiological research of cartilage in three major steps:

- Numerical investigation was performed to study the potential effect of sliding, that promotes high fluid load support, on the chondrocyte biomechanical environment, compared to uniaxial cyclic compression. This study showed that the fluid pressure and tissue strain distribution profiles are completely different between the two loading mode. Therefore, micro mechanical

environment of chondrocytes is expected to be different under both loading regime at the same level of stress/strain.

- Motivated by results form the first study, two testing devices were custom-made and validated to be used for mechanobiological testing of cartilage explants. I showed that tissue properties could be determined using a combination of experiment and finite element simulation; these properties were then applied to simulated sliding which produced results that agreed with experiment. Furthermore, the capabilities of these devices are more suitable for cartilage testing and are much cheaper than most commercially-available devices.

- Mechanobiological experiments were performed to examine the effect of sliding on various biochemical signals that are believed to control cartilage metabolism and compared to uniaxial cyclic compression. Although statistical significance was obscured by the low number of specimens, results suggest that the loading mode does have an effect on the level of biochemical signals in cartilage explants.

6.3 Future Directions

Although this work has introduced a more physiological loading protocol for mechanobiological *in vitro* testing of cartilage, experimental testing was mostly restricted by the sample availability. Therefore, future work will focus on enlarging the sample size to allow for testing wide range of loads, sliding speeds, stroke length, as well as indenter sizes.

Moreover, the role of subchondral bone in the degenerative process is still uncertain. Therefore, mechanobiological testing will be performed on samples of cartilage with and without subchondral bone should explain the subchondral bone contribution to the disease process and provide new insights toward osteoarthritis initiation and progression. Furthermore, multi-scale models were extended from this work (Abdul Khan, MASc thesis) that allowed a better understanding of the micromechanical environment of the chondrocyte. These can be used with the biochemical response to gain more detailed insight into chondrocyte mechanobiology in situ.

Bibliography

Mario Alberto Accardi, Daniele Dini, and Philippa M Cann. Experimental and numerical investigation of the behaviour of articular cartilage under shear loading—interstitial fluid pressurisation and lubrication mechanisms. *Tribology International*, 44(5):565–578, 2011.

B Ackermann and J Steinmeyer. Collagen biosynthesis of mechanically loaded articular cartilage explants. *Osteoarthritis and cartilage*, 13(10):906–914, 2005.

J Winslow Alford and Brian J Cole. Cartilage restoration, part 1 basic science, historical perspective, patient evaluation, and treatment options. *The American journal of sports medicine*, 33(2):295–306, 2005.

D Ron Anderson, Savio L-Y Woo, Michael K Kwan, and David H Gershuni. Viscoelastic shear properties of the equine medial meniscus. *Journal of orthopaedic research*, 9(4):550–558, 1991.

Donald D Anderson, Susan Chubinskaya, Farshid Guilak, James A Martin, Theodore R Oegema, Steven A Olson, and Joseph A Buckwalter. Post-traumatic osteoarthritis: Improved understanding and opportunities for early intervention. *Journal of orthopaedic research*, 29(6):802–809, 2011.

Thomas P Andriacchi and Annegret Mündermann. The role of ambulatory mechanics in the initiation and progression of knee osteoarthritis. *Current opinion in rheumatology*, 18(5):514–518, 2006.

Thomas P Andriacchi, Anne Mündermann, R Lane Smith, Eugene J Alexander, Chris O Dyrby, and Seungbum Koo. A framework for the in vivo pathomechanics of osteoarthritis at the knee. *Annals of biomedical engineering*, 32(3):447–457, 2004.

M Argoubi and A Shirazi-Adl. Poroelastic creep response analysis of a lumbar motion segment in compression. *Journal of biomechanics*, 29(10):1331–1339, 1996.

CG Armstrong and VC Mow. Variations in the intrinsic mechanical properties of human articular cartilage with age, degeneration, and water content. *J Bone Joint Surg Am*, 64(1):88–94, 1982.

CG Armstrong, AS Bahrani, and DL Gardner. Changes in the deformational behavior of human hip cartilage with age. *Journal of biomechanical engineering*, 102 (3):214–220, 1980.

Jari PA Arokoski, Mika M Hyttinen, Heikki J Helminen, and Jukka S Jurvelin. Biomechanical and structural characteristics of canine femoral and tibial cartilage. *Journal of Biomedical Materials Research: An Official Journal of The Society for Biomaterials, The Japanese Society for Biomaterials, and The Australian Society for Biomaterials*, 48(2):99–107, 1999.

GA Ateshian, LJ Soslowsky, and VC Mow. Quantitation of articular surface topography and cartilage thickness in knee joints using stereophotogrammetry. *Journal of biomechanics*, 24(8):761–776, 1991.

GA Ateshian, WM Lai, WB Zhu, and VC Mow. An asymptotic solution for the contact of two biphasic cartilage layers. *Journal of biomechanics*, 27(11):1347–1360, 1994.

Gerard A Ateshian. The role of interstitial fluid pressurization in articular cartilage lubrication. *Journal of biomechanics*, 42(9):1163–1176, 2009.

Gerard A Ateshian and Huiqun Wang. A theoretical solution for the frictionless rolling contact of cylindrical biphasic articular cartilage layers. *Journal of biomechanics*, 28(11):1341–1355, 1995.

Gerard A Ateshian, Vikram Rajan, Nadeen O Chahine, Clare E Canal, and Clark T Hung. Modeling the matrix of articular cartilage using a continuous fiber angular distribution predicts many observed phenomena. *Journal of biomechanical engineering*, 131(6):1–34, 2009.

Gerard A Ateshian, Steve Maas, and Jeffrey A Weiss. Finite element algorithm for frictionless contact of porous permeable media under finite deformation and sliding. *Journal of biomechanical engineering*, 132(6):061006, 2010.

KA Athanasiou, MP Rosenwasser, JA Buckwalter, TI Malinin, and VC Mow. Interspecies comparisons of in situ intrinsic mechanical properties of distal femoral cartilage. *Journal of Orthopaedic Research*, 9(3):330–340, 1991.

KA Athanasiou, Animesh Agarwal, and FJ Dzida. Comparative study of the intrinsic mechanical properties of the human acetabular and femoral head cartilage. *Journal of Orthopaedic Research*, 12(3):340–349, 1994.

Kyriacos A Athanasiou, Eric M Darling, and Jerry C Hu. Articular cartilage tissue engineering. *Synthesis Lectures on Tissue Engineering*, 1(1):1–182, 2009.

Margaret B Aydelotte and Klaus E Kuettner. Differences between sub-populations of cultured bovine articular chondrocytes. i. morphology and cartilage matrix production. *Connective tissue research*, 18(3):205–222, 1988.

Daniel L Bader, Geoffrey E Kempson, John Egan, Wendy Gilbey, and Alan J Barrett. The effects of selective matrix degradation on the short-term compressive properties of adult human articular cartilage. *Biochimica et Biophysica Acta (BBA)-General Subjects*, 1116(2):147–154, 1992.

Elizabeth M Badley and Peizhong Peter Wang. Arthritis and the aging population: projections of arthritis prevalence in canada 1991 to 2031. *The Journal of rheumatology*, 25(1):138–144, 1998.

EM Badley. The effect of osteoarthritis on disability and health care use in canada. *The Journal of rheumatology. Supplement*, 43:19–22, 1995.

G Bergmann, G Deuretzbacher, M Heller, F Graichen, A Rohlmann, J Strauss, and GN Duda. Hip contact forces and gait patterns from routine activities. *Journal of biomechanics*, 34(7):859–871, 2001.

Liming Bian, Jason V Fong, Eric G Lima, Aaron M Stoker, Gerard A Ateshian, James L Cook, and Clark T Hung. Dynamic mechanical loading enhances functional properties of tissue-engineered cartilage using mature canine chondrocytes. *Tissue Engineering Part A*, 16(5):1781–1790, 2010.

Darryl Blalock, Andrew Miller, Michael Tilley, and Jinxi Wang. Joint instability and osteoarthritis. *Clinical Medicine Insights: Arthritis and Musculoskeletal Disorders*, 8:CMAMD–S22147, 2015.

Heide Boeth, Georg N Duda, Markus O Heller, Rainald M Ehrig, Ralf Doyscher, Tobias Jung, Philippe Moewis, Sven Scheffler, and William R Taylor. Anterior cruciate ligament–deficient patients with passive knee joint laxity have a decreased range of anterior-posterior motion during active movements. *The American journal of sports medicine*, 41(5):1051–1057, 2013.

C Bombardier, G Hawker, D Mosher, et al. Arthritis alliance of canada. the impact of arthritis in canada: Today and over the next 30 years, 2012.

ED Bonnevie, VJ Baro, L Wang, and David L Burris. In situ studies of cartilage microtribology: roles of speed and contact area. *Tribology letters*, 41(1):83–95, 2011.

ED Bonnevie, VJ Baro, L Wang, and DL Burris. Fluid load support during localized indentation of cartilage with a spherical probe. *Journal of biomechanics*, 45(6): 1036–1041, 2012.

Carl T Brighton and R Bruce Heppenstall. Oxygen tension in zones of the epiphyseal plate, the metaphysis and diaphysis: An in vitro and in viro study in rats and rabbits. *JBJS*, 53(4):719–728, 1971.

PG Bullough and ANAND Jagannath. The morphology of the calcification front in articular cartilage. its significance in joint function. *Journal of Bone & Joint Surgery, British Volume*, 65(1):72–78, 1983.

Michael D Buschmann, Julien Soulhat, Aboulfazl Shirazi-Adl, Jukka S Jurvelin, and Ernst B Hunziker. Confined compression of articular cartilage: linearity in ramp and sinusoidal tests and the importance of interdigitation and incomplete confinement. *Journal of biomechanics*, 31(2):171–178, 1997.

Michael D Buschmann, Young-Jo Kim, Marcy Wong, Eliot Frank, Ernst B Hunziker, and Alan J Grodzinsky. Stimulation of aggrecan synthesis in cartilage explants by cyclic loading is localized to regions of high interstitial fluid flow. *Archives of biochemistry and Biophysics*, 366(1):1–7, 1999.

Matteo Caligaris and Gerard A Ateshian. Effects of sustained interstitial fluid pressurization under migrating contact area, and boundary lubrication by synovial fluid, on cartilage friction. *Osteoarthritis and Cartilage*, 16(10):1220–1227, 2008.

Mattia Capulli, Riccardo Paone, and Nadia Rucci. Osteoblast and osteocyte: games without frontiers. *Archives of biochemistry and biophysics*, 561:3–12, 2014.

Michael J Carter, Ines M Basalo, and Gerard A Ateshian. The temporal response of the friction coefficient of articular cartilage depends on the contact area. *Journal of biomechanics*, 40(14):3257–3260, 2007.

Tirupathi R Chandrupatla, Ashok D Belegundu, T Ramesh, and Chaitali Ray. *Introduction to finite elements in engineering*, volume 2. Prentice Hall Upper Saddle River, NJ, 2002.

Adele Changoor, Liah Fereydoonzad, Alex Yaroshinsky, and Michael D Buschmann. Effects of refrigeration and freezing on the electromechanical and biomechanical properties of articular cartilage. *Journal of biomechanical engineering*, 132(6):064502, 2010.

Salman Chegini and Stephen J Ferguson. Time and depth dependent poisson's ratio of cartilage explained by an inhomogeneous orthotropic fiber embedded biphasic model. *Journal of biomechanics*, 43(9):1660–1666, 2010.

AC Chen, WC Bae, RM Schinagl, and RL Sah. Depth-and strain-dependent mechanical and electromechanical properties of full-thickness bovine articular cartilage in confined compression. *Journal of biomechanics*, 34(1):1–12, 2001.

Xingyu Chen, Yilu Zhou, Liyun Wang, Michael H Santare, Leo Q Wan, and X Lucas Lu. Determining tension–compression nonlinear mechanical properties of articular cartilage from indentation testing. *Annals of biomedical engineering*, 44 (4):1148–1158, 2016.

Emily E Coates and John P Fisher. Phenotypic variations in chondrocyte subpopulations and their response to in vitro culture and external stimuli. *Annals of biomedical engineering*, 38(11):3371–3388, 2010.

Emily E Coates and John P Fisher. Engineering superficial zone chondrocytes from mesenchymal stem cells. *Tissue Engineering Part C: Methods*, 20(8):630–640, 2014.

M Rita Correro-Shahgaldian, Chafik Ghayor, Nicholas D Spencer, Franz E Weber, and Luigi M Gallo. A model system of the dynamic loading occurring in synovial joints: the biological effect of plowing on pristine cartilage. *Cells Tissues Organs*, 199(5-6):364–372, 2014.

Maria Rita Correro-Shahgaldian, Jasmin Introvigne, Chafik Ghayor, Franz E Weber, Luigi M Gallo, and Vera Colombo. Properties and mechanobiological behavior of bovine nasal septum cartilage. *Annals of biomedical engineering*, 44(5): 1821–1831, 2016.

Philipp Damm, Ines Kutzner, Georg Bergmann, Antonius Rohlmann, and Hendrik Schmidt. Comparison of in vivo measured loads in knee, hip and spinal implants during level walking. *Journal of biomechanics*, 51:128–132, 2017.

Van der Voet and Adrian Frank. *Finite element modelling of load transfer through articular cartilage*. Calgary, 1992.

Erica Di Federico, Dan L Bader, and Julia C Shelton. Design and validation of an in vitro loading system for the combined application of cyclic compression and shear to 3d chondrocytes-seeded agarose constructs. *Medical engineering & physics*, 36(4):534–540, 2014.

Mark R DiSilvestro and Jun-Kyo Francis Suh. A cross-validation of the biphasic poroviscoelastic model of articular cartilage in unconfined compression, indentation, and confined compression. *Journal of biomechanics*, 34(4):519–525, 2001.

Mark R DiSilvestro, Qiliang Zhu, Marcy Wong, Jukka S Jurvelin, and Jun-Kyo Francis Suh. Biphasic poroviscoelastic simulation of the unconfined compression of articular cartilage: I—simultaneous prediction of reaction force and lateral displacement. *Journal of biomechanical engineering*, 123(2):191–197, 2001.

Duncan Dowson. Bio-tribology. *Faraday discussions*, 156(1):9–30, 2012.

Dorothy D Dunlop, Larry M Manheim, Edward H Yelin, Jing Song, and Rowland W Chang. The costs of arthritis. *Arthritis Care & Research*, 49(1):101–113, 2003.

Salvatore Federico and Walter Herzog. On the anisotropy and inhomogeneity of permeability in articular cartilage. *Biomechanics and modeling in mechanobiology*, 7 (5):367–378, 2008a.

Salvatore Federico and Walter Herzog. On the permeability of fibre-reinforced porous materials. *International Journal of Solids and Structures*, 45(7):2160–2172, 2008b.

Salvatore Federico, Guido La Rosa, Walter Herzog, and John Z Wu. Effect of fluid boundary conditions on joint contact mechanics and applications to the modeling of osteoarthritic joints. *Journal of Biomechanical Engineering*, 126(2):220–225, 2004.

SJ Ferguson, JT Bryant, R Ganz, and Keita Ito. The acetabular labrum seal: a poroelastic finite element model. *Clinical Biomechanics*, 15(6):463–468, 2000.

SJ Ferguson, JT Bryant, R Ganz, and Keita Ito. An in vitro investigation of the acetabular labral seal in hip joint mechanics. *Journal of biomechanics*, 36(2):171–178, 2003.

J Fisher, D Dowson, H Hamdzah, and HL Lee. The effect of sliding velocity on the friction and wear of uhmwpe for use in total artificial joints. *Wear*, 175(1-2): 219–225, 1994.

Jonathan B Fitzgerald, Moonsoo Jin, and Alan J Grodzinsky. Shear and compression differentially regulate clusters of functionally related temporal transcription patterns in cartilage tissue. *Journal of Biological Chemistry*, 281(34):24095–24103, 2006.

Charlene M Flahiff, Daria A Narmoneva, Janet L Huebner, Virginia B Kraus, Farshid Guilak, and Lori A Setton. Osmotic loading to determine the intrinsic material properties of guinea pig knee cartilage. *Journal of biomechanics*, 35(9): 1285–1290, 2002.

Alice J Sophia Fox, Asheesh Bedi, and Scott A Rodeo. The basic science of articular cartilage: structure, composition, and function. *Sports Health: A Multidisciplinary Approach*, 1(6):461–468, 2009.

Eliot H Frank, Moonsoo Jin, Andreas M Loening, Marc E Levenston, and Alan J Grodzinsky. A versatile shear and compression apparatus for mechanical stimulation of tissue culture explants. *Journal of biomechanics*, 33(11):1523–1527, 2000.

Mark I Froimson, Anthony Ratcliffe, Thomas R Gardner, and Van C Mow. Differences in patellofemoral joint cartilage material properties and their significance to the etiology of cartilage surface fibrillation. *Osteoarthritis and Cartilage*, 5(6): 377–386, 1997.

R Fujioka, T Aoyama, and T Takakuwa. The layered structure of the articular surface. *Osteoarthritis and cartilage*, 21(8):1092–1098, 2013.

Naoshi Fukui, Yasuko Ikeda, Toshiyuki Ohnuki, Nobuho Tanaka, Atsuhiko Hikita, Hiroyuki Mitomi, Toshihito Mori, Takuo Juji, Yozo Katsuragawa, Seizo Yamamoto, et al. Regional differences in chondrocyte metabolism in osteoarthritis: a detailed analysis by laser capture microdissection. *Arthritis & Rheumatism*, 58 (1):154–163, 2008.

Reinhold Ganz, Michael Leunig, Katharina Leunig-Ganz, and William H Harris. The etiology of osteoarthritis of the hip. *Clinical orthopaedics and related research*, 466(2):264–272, 2008.

Christophe Geuzaine and Jean-François Remacle. Gmsh: A 3-d finite element mesh generator with built-in pre-and post-processing facilities. *International Journal for Numerical Methods in Engineering*, 79(11):1309–1331, 2009.

Mary B Goldring. Osteoarthritis and cartilage: the role of cytokines. *Current rheumatology reports*, 2(6):459–465, 2000.

Mary B Goldring and Kenneth B Marcu. Cartilage homeostasis in health and rheumatic diseases. *Arthritis research & therapy*, 11(3):224, 2009.

MB Goldring, M Otero, K Tsuchimochi, K Ijiri, and Y Li. Defining the roles of inflammatory and anabolic cytokines in cartilage metabolism. *Annals of the rheumatic diseases*, 67(Suppl 3):iii75–iii82, 2008.

Steven R Goldring and Mary B Goldring. The role of cytokines in cartilage matrix degeneration in osteoarthritis. *Clinical Orthopaedics and Related Research (1976-2007)*, 427:S27–S36, 2004.

Kasper Kjaerulf Gosvig, Steffen Jacobsen, Stig Sonne-Holm, Henrik Palm, and Anders Troelsen. Prevalence of malformations of the hip joint and their relationship to sex, groin pain, and risk of osteoarthritis. *The Journal of Bone & Joint Surgery*, 92(5):1162–1169, 2010.

Sibylle Grad, David Eglin, Mauro Alini, and Martin J Stoddart. Physical stimulation of chondrogenic cells in vitro: a review. *Clinical Orthopaedics and Related Research®*, 469(10):2764–2772, 2011.

Alan J Grodzinsky, Marc E Levenston, Moonsoo Jin, and Eliot H Frank. Cartilage tissue remodeling in response to mechanical forces. *Annual review of biomedical engineering*, 2(1):691–713, 2000.

Farshid Guilak. Biomechanical factors in osteoarthritis. *Best practice & research Clinical rheumatology*, 25(6):815–823, 2011.

Farshid Guilak, B Christoph Meyer, Anthony Ratcliffe, and Van C Mow. The effects of matrix compression on proteoglycan metabolism in articular cartilage explants. *Osteoarthritis and cartilage*, 2(2):91–101, 1994a.

Farshid Guilak, Anthony Ratcliffe, Nancy Lane, Melvin P Rosenwasser, and Van C Mow. Mechanical and biochemical changes in the superficial zone of articular

cartilage in canine experimental osteoarthritis. *Journal of Orthopaedic Research*, 12 (4):474–484, 1994b.

Jussi Haapala, Jari PA Arokoski, Mika M Hyttinen, Mikko Lammi, Markku Tammi, Vuokko Kovanen, Heikki J Helminen, and Ilkka Kiviranta. Remobilization does not fully restore immobilization induced articular cartilage atrophy. *Clinical orthopaedics and related research*, 362:218–229, 1999.

Joseph M Haemer, Dennis R Carter, and Nicholas J Giori. The low permeability of healthy meniscus and labrum limit articular cartilage consolidation and maintain fluid load support in the knee and hip. *Journal of biomechanics*, 45(8): 1450–1456, 2012.

EunHee Han, Silvia S Chen, Stephen M Klisch, and Robert L Sah. Contribution of proteoglycan osmotic swelling pressure to the compressive properties of articular cartilage. *Biophysical journal*, 101(4):916–924, 2011.

WC Hayes, LM Keer, G Herrmann, and LF Mockros. A mathematical analysis for indentation tests of articular cartilage. *Journal of biomechanics*, 5(5):541–551, 1972.

WA Hodge, KL Carlson, RS Fijan, RG Burgess, PO Riley, WH Harris, and RW Mann. Contact pressures from an instrumented hip endoprosthesis. *JBJS*, 71(9):1378–1386, 1989.

MH Holmes and VC Mow. The nonlinear characteristics of soft gels and hydrated connective tissues in ultrafiltration. *Journal of biomechanics*, 23(11):1145–1156, 1990.

Jerry CY Hu and Kyriacos A Athanasiou. Structure and function of articular cartilage. In *Handbook of histology methods for bone and cartilage*, pages 73–95. Springer, 2003.

Alice H Huang, Brendon M Baker, Gerard A Ateshian, and Robert L Mauck. Sliding contact loading enhances the tensile properties of mesenchymal stem cell-seeded hydrogels. *Eur Cell Mater*, 24:29–45, 2012.

N Yu Ignat'eva, SV Averkiev, VV Lunin, TE Grokhovskaya, VN Bagratashvili, ES Yantsen, et al. Thermal stability of collagen ii in cartilage. In *Doklady Biochemistry and Biophysics*, volume 395, pages 96–98. Springer, 2004.

MRPharmS Ipresc and Andrew Barr. Osteoarthritis: pathophysiology and diagnosis. *Health*, 10:27, 2015.

MJ Jaffar. Prediction of the film thickness for the normal approach of a rigid sphere towards a thin soft layer. *Tribology Letters*, 22(3):247–251, 2006.

June E Jeon, Karsten Schrobback, Dietmar W Hutmacher, and Travis J Klein. Dynamic compression improves biosynthesis of human zonal chondrocytes from osteoarthritis patients. *Osteoarthritis and Cartilage*, 20(8):906–915, 2012.

Moonsoo Jin, Eliot H Frank, Thomas M Quinn, Ernst B Hunziker, and Alan J Grodzinsky. Tissue shear deformation stimulates proteoglycan and protein biosynthesis in bovine cartilage explants. *Archives of biochemistry and biophysics*, 395(1):41–48, 2001.

Kenneth Langstreth Johnson and Kenneth Langstreth Johnson. *Contact mechanics*. Cambridge university press, 1987.

Matti O Jortikka, Jyrki J Parkkinen, Ritva I Inkinen, Jüri Kärner, Hannu T Järveläinen, Lassi O Nelimarkka, Markku I Tammi, and Mikko J Lammi. The role of microtubules in the regulation of proteoglycan synthesis in chondrocytes under hydrostatic pressure. *Archives of biochemistry and biophysics*, 374(2):172–180, 2000.

Petro Julkunen, Wouter Wilson, Hanna Isaksson, Jukka S Jurvelin, Walter Herzog, and Rami K Korhonen. A review of the combination of experimental measurements and fibril-reinforced modeling for investigation of articular cartilage and chondrocyte response to loading. *Computational and mathematical methods in medicine*, 2013, 2013.

Ronald K June and David P Fyhrie. Temperature effects in articular cartilage biomechanics. *Journal of Experimental Biology*, 213(22):3934–3940, 2010.

JS Jurvelin, MD Buschmann, and EB Hunziker. Optical and mechanical determination of poisson's ratio of adult bovine humeral articular cartilage. *Journal of biomechanics*, 30(3):235–241, 1997.

Jukka S Jurvelin, Tuomas Räsänen, Pekka Kolmonens, and Tiina Lyyra. Comparison of optical, needle probe and ultrasonic techniques for the measurement of articular cartilage thickness. *Journal of biomechanics*, 28(2):231–235, 1995.

Jarred M Kaiser, Michael F Vignos, Richard Kijowski, Geoffrey Baer, and Darryl G Thelen. Effect of loading on in vivo tibiofemoral and patellofemoral kinematics of healthy and acl-reconstructed knees. *The American journal of sports medicine*, 45(14):3272–3279, 2017.

Christopher E Kawcak, C Wayne McIlwraith, RW Norrdin, RD Park, and SP James. The role of subchondral bone in joint disease: a review. *Equine veterinary journal*, 33(2):120–126, 2001.

GN Kiefer, K Sundby, D McAllister, NG Shrive, CB Frank, T Lam, and NS Schachar. The effect of cryopreservation on the biomechanical behavior of bovine articular cartilage. *Journal of Orthopaedic Research*, 7(4):494–501, 1989.

Young-Jo Kim, Robert LY Sah, Alan J Grodzinsky, Anna HK Plaas, and John D Sandy. Mechanical regulation of cartilage biosynthetic behavior: physical stimuli. *Archives of biochemistry and biophysics*, 311(1):1–12, 1994.

Young-Jo Kim, Lawrence J Bonassar, and Alan J Grodzinsky. The role of cartilage streaming potential, fluid flow and pressure in the stimulation of chondrocyte biosynthesis during dynamic compression. *Journal of biomechanics*, 28(9):1055–1066, 1995.

Ilkka Kiviranta, Markku Tammi, Jukka Jurvelin, Jari Arokoski, Anna-Marja Säämänen, and Heikki J Helminen. Articular cartilage thickness and glycosaminoglycan distribution in the young canine knee joint after remobilization of the immobilized limb. *Journal of orthopaedic research*, 12(2):161–167, 1994.

Derrick M Knapik, Joshua D Harris, Garett Pangrazzi, Michael J Griesser, Robert A Siston, Sudha Agarwal, and David C Flanigan. The basic science of continuous passive motion in promoting knee health: a systematic review of studies in a rabbit model. *Arthroscopy: The Journal of Arthroscopic & Related Surgery*, 29(10): 1722–1731, 2013.

RK Korhonen, MS Laasanen, J Töyräs, J Rieppo, J Hirvonen, HJ Helminen, and JS Jurvelin. Comparison of the equilibrium response of articular cartilage in unconfined compression, confined compression and indentation. *Journal of biomechanics*, 35(7):903–909, 2002.

Ramaswamy Krishnan, Seonghun Park, Felix Eckstein, and Gerard A Ateshian. Inhomogeneous cartilage properties enhance superficial interstitial fluid support and frictional properties, but do not provide a homogeneous state of stress. *Journal of biomechanical engineering*, 125(5):569–577, 2003.

Ramaswamy Krishnan, Monika Kopacz, and Gerard A Ateshian. Experimental verification of the role of interstitial fluid pressurization in cartilage lubrication. *Journal of Orthopaedic Research*, 22(3):565–570, 2004.

Ramaswamy Krishnan, Elise N Mariner, and Gerard A Ateshian. Effect of dynamic loading on the frictional response of bovine articular cartilage. *Journal of biomechanics*, 38(8):1665–1673, 2005.

Hideji Kura, Harold B Kitaoka, Zong-Ping Luo, and Kai-Nan An. Measurement of surface contact area of the ankle joint. *Clinical Biomechanics*, 13(4):365–370, 1998.

Bodo Kurz, Moonsoo Jin, Parth Patwari, Debbie M Cheng, Michael W Lark, and Alan J Grodzinsky. Biosynthetic response and mechanical properties of articular cartilage after injurious compression. *Journal of Orthopaedic Research*, 19(6):1140–1146, 2001.

Bodo Kurz, Angelika Lemke, Melanie Kehn, Christian Domm, Parth Patwari, Eliot H Frank, Alan J Grodzinsky, and Michael Schünke. Influence of tissue maturation and antioxidants on the apoptotic response of articular cartilage after injurious compression. *Arthritis & Rheumatism: Official Journal of the American College of Rheumatology*, 50(1):123–130, 2004.

MS Laasanen, J Toyras, RK Korhonen, J Rieppo, S Saarakkala, MT Nieminen, J Hirvonen, and JS Jurvelin. Biomechanical properties of knee articular cartilage. *Biorheology*, 40(1-3):133–140, 2003.

W Michael Lai, JS Hou, and Van C Mow. A triphasic theory for the swelling and deformation behaviors of articular cartilage. *Journal of biomechanical engineering*, 113(3):245–258, 1991.

WM Lai, Van C Mow, and V Roth. Effects of nonlinear strain-dependent permeability and rate of compression on the stress behavior of articular cartilage. *Journal of biomechanical engineering*, 103(2):61–66, 1981.

Emily H Lakes, Courtney L Kline, Peter S McFetridge, and Kyle D Allen. Comparing the mechanical properties of the porcine knee meniscus when hydrated in saline versus synovial fluid. *Journal of biomechanics*, 48(16):4333–4338, 2015.

A Latourte, J Maillet, J Goossens, HK Ea, M Cohen-Solal, E Haÿ, and P Richette. Op0007 ccr2 inhibition abrogates il-6–induced activation of matrix metalloproteinases in cartilage, 2017.

David A Lee, Takashi Noguchi, Martin M Knight, Liam O'donnell, George Bentley, and Dan L Bader. Response of chondrocyte subpopulations cultured within unloaded and loaded agarose. *Journal of orthopaedic research*, 16(6):726–733, 1998.

Guoan Li, Sang Eun Park, Louis E DeFrate, Matthew E Schutzer, Lunan Ji, Thomas J Gill, and Harry E Rubash. The cartilage thickness distribution in the tibiofemoral joint and its correlation with cartilage-to-cartilage contact. *Clinical biomechanics*, 20(7):736–744, 2005.

LP Li and W Herzog. Strain-rate dependence of cartilage stiffness in unconfined compression: the role of fibril reinforcement versus tissue volume change in fluid pressurization. *Journal of biomechanics*, 37(3):375–382, 2004.

LP Li, J Soulhat, MD Buschmann, and A Shirazi-Adl. Nonlinear analysis of cartilage in unconfined ramp compression using a fibril reinforced poroelastic model. *Clinical Biomechanics*, 14(9):673–682, 1999.

LP Li, MD Buschmann, and A Shirazi-Adl. A fibril reinforced nonhomogeneous

poroelastic model for articular cartilage: inhomogeneous response in unconfined compression. *Journal of biomechanics*, 33(12):1533–1541, 2000.

Qing Li, Basak Doyran, Laura W Gamer, X Lucas Lu, Ling Qin, Christine Ortiz, Alan J Grodzinsky, Vicki Rosen, and Lin Han. Biomechanical properties of murine meniscus surface via afm-based nanoindentation. *Journal of biomechanics*, 48(8):1364–1370, 2015.

Yang Li, Eliot H Frank, Yang Wang, Susan Chubinskaya, H-H Huang, and Alan J Grodzinsky. Moderate dynamic compression inhibits pro-catabolic response of cartilage to mechanical injury, tumor necrosis factor-α and interleukin-6, but accentuates degradation above a strain threshold. *Osteoarthritis and cartilage*, 21 (12):1933–1941, 2013.

Andreas M Loening, Ian E James, Marc E Levenston, Alison M Badger, Eliot H Frank, Bodo Kurz, Mark E Nuttall, Han-Hwa Hung, Simon M Blake, Alan J Grodzinsky, et al. Injurious mechanical compression of bovine articular cartilage induces chondrocyte apoptosis. *Archives of biochemistry and biophysics*, 381(2): 205–212, 2000.

Richard F Loeser. Aging and osteoarthritis: the role of chondrocyte senescence and aging changes in the cartilage matrix. *Osteoarthritis and cartilage*, 17(8):971–979, 2009.

Xin L Lu and Van C Mow. Biomechanics of articular cartilage and determination of material properties. *Medicine & Science in Sports & Exercise*, 40(2):193–199, 2008.

SA Maas, D Rawlins, JA Weiss, and GA Ateshian. Febio 2.7 theory manual, 2018.

Steve A Maas, Benjamin J Ellis, Gerard A Ateshian, and Jeffrey A Weiss. Febio:

finite elements for biomechanics. *Journal of biomechanical engineering*, 134(1): 011005, 2012.

Alisdair R MacLeod, Hannah Rose, and Harinderjit S Gill. A validated open-source multisolver fourth-generation composite femur model. *Journal of biomechanical engineering*, 138(12):124501, 2016.

Henning Madry, Frank P Luyten, and Andrea Facchini. Biological aspects of early osteoarthritis. *Knee Surgery, Sports Traumatology, Arthroscopy*, 20(3):407–422, 2012.

Franz Maier, Hicham Drissi, and David M Pierce. Shear deformations of human articular cartilage: certain mechanical anisotropies apparent at large but not small shear strains. *Journal of the mechanical behavior of biomedical materials*, 65:53–65, 2017.

AF Mak, WM Lai, and VC Mow. Biphasic indentation of articular cartilage—i. theoretical analysis. *Journal of biomechanics*, 20(7):703–714, 1987.

Bradley N Maker. A nonlinear, implicit, three-dimensional finite element code for solid and structural mechanics-users manual. Technical report, Lawrence Livermore National Lab., CA (United States), 1995.

Yuanqing Mao, Degang Yu, Chen Xu, Fengxiang Liu, Huiwu Li, and Zhenan Zhu. The fate of osteophytes in the superolateral region of the acetabulum after total hip arthroplasty. *The Journal of arthroplasty*, 29(12):2262–2266, 2014.

A Maroudas. Physicochemical properties of articular cartilage. *Adult articular cartilage*, 2:215–290, 1979.

A Maroudas, MT Bayliss, N Uchitel-Kaushansky, R Schneiderman, and E Gilav.

Aggrecan turnover in human articular cartilage: use of aspartic acid racemization as a marker of molecular age. *Archives of biochemistry and biophysics*, 350(1): 61–71, 1998.

Charles W McCutchen. The frictional properties of animal joints. *Wear*, 5(1):1–17, 1962.

Qingen Meng, Zhongmin Jin, John Fisher, and Ruth Wilcox. Comparison between febio and abaqus for biphasic contact problems. *Proceedings of the Institution of Mechanical Engineers, Part H: Journal of Engineering in Medicine*, pages 1009–1019, 2013.

Qingen Meng, Shuqiang An, Robin A Damion, Zhongmin Jin, Ruth Wilcox, John Fisher, and Alison Jones. The effect of collagen fibril orientation on the biphasic mechanics of articular cartilage. *Journal of the mechanical behavior of biomedical materials*, 65:439–453, 2017.

PL Mente and JL Lewis. Elastic modulus of calcified cartilage is an order of magnitude less than that of subchondral bone. *Journal of Orthopaedic Research*, 12(5): 637–647, 1994.

George R Milner and Jesper L Boldsen. Humeral and femoral head diameters in recent white american skeletons. *Journal of forensic sciences*, 57(1):35–40, 2012.

Linda Mitchell. Anatomy and human movement—structure and function. *Physical Therapy in Sport*, 4(1):46, 2003.

Hadi Mohammadi, Kibret Mequanint, and Walter Herzog. Computational aspects in mechanical modeling of the articular cartilage tissue. *Proceedings of the Institution of Mechanical Engineers, Part H: Journal of Engineering in Medicine*, 227(4): 402–420, 2013.

AP Monk, K Choji, JJ O'Connor, JW Goodfellow, and DW Murray. The shape of the distal femur: a geometrical study using mri. *Bone Joint J*, 96(12):1623–1630, 2014.

ME Mononen, P Julkunen, J Töyräs, JS Jurvelin, I Kiviranta, and RK Korhonen. Alterations in structure and properties of collagen network of osteoarthritic and repaired cartilage modify knee joint stresses. *Biomechanics and modeling in mechanobiology*, 10(3):357–369, 2011.

AC Moore and DL Burris. An analytical model to predict interstitial lubrication of cartilage in migrating contact areas. *Journal of biomechanics*, 47(1):148–153, 2014.

Axel C Moore and David L Burris. Tribological and material properties for cartilage of and throughout the bovine stifle: support for the altered joint kinematics hypothesis of osteoarthritis. *Osteoarthritis and cartilage*, 23(1):161–169, 2015.

Axel C Moore and David L Burris. Tribological rehydration of cartilage and its potential role in preserving joint health. *Osteoarthritis and cartilage*, 25(1):99–107, 2017.

Van C Mow and X Edward Guo. Mechano-electrochemical properties of articular cartilage: their inhomogeneities and anisotropies. *Annual Review of Biomedical Engineering*, 4(1):175–209, 2002.

Van C Mow and W Michael Lai. Recent developments in synovial joint biomechanics. *Siam Review*, 22(3):275–317, 1980.

Van C Mow, MC Gibbs, W Michael Lai, WB Zhu, and Kyriacos A Athanasiou. Biphasic indentation of articular cartilage—ii. a numerical algorithm and an experimental study. *Journal of biomechanics*, 22(8):853–861, 1989.

Van C Mow, Anthony Ratcliffe, and A Robin Poole. Cartilage and diarthrodial joints as paradigms for hierarchical materials and structures. *Biomaterials*, 13(2): 67–97, 1992.

VC Mow, SC Kuei, WM Lai, and CG Armstrong. Biphasic creep and stress relaxation of articular cartilage in compression: theory and experiments. *Journal of biomechanical engineering*, 102(1):73–84, 1980.

VC Mow, DC Fithian, and MA Kelly. Fundamentals of articular cartilage and meniscus biomechanics. *Articular cartilage and knee joint function: basic science and arthroscopy*, pages 1–18, 1990.

H Muir. Cartilage structure and metabolism and basic changes in degenerative joint disease. *Australian and New Zealand journal of medicine*, 8:1–5, 1978.

Helen Muir. The chondrocyte, architect of cartilage. biomechanics, structure, function and molecular biology of cartilage matrix macromolecules. *Bioessays*, 17(12): 1039–1048, 1995.

Magdalena Müller-Gerbl, Erik Schulte, and Reinhard Putz. The thickness of the calcified layer of articular cartilage: a function of the load supported? *Journal of anatomy*, 154:103, 1987.

Teruo Murakami. The lubrication in natural synovial joints and joint prostheses. *JSME international journal. Ser. 3, Vibration, control engineering, engineering for industry*, 33(4):465–474, 1990.

Corey P Neu, Kyriakos Komvopoulos, and A Hari Reddi. The interface of functional biotribology and regenerative medicine in synovial joints. *Tissue Engineering Part B: Reviews*, 14(3):235–247, 2008.

GD Nicodemus and SJ Bryant. Mechanical loading regimes affect the anabolic and catabolic activities by chondrocytes encapsulated in peg hydrogels. *Osteoarthritis and cartilage*, 18(1):126–137, 2010.

Siobhan O'Donnell, C Lagacé, Louise Mcrae, and Christina Bancej. Report summary: Life with arthritis in canada - a personal and public health challenge. 31: 135–6, 06 2011.

Theodore R Oegema, Randall J Carpenter, Francine Hofmeister, and Roby C Thompson. The interaction of the zone of calcified cartilage and subchondral bone in osteoarthritis. *Microscopy research and technique*, 37(4):324–332, 1997.

S Park, CT Hung, and GA Ateshian. Mechanical response of bovine articular cartilage under dynamic unconfined compression loading at physiological stress levels. *Osteoarthritis and cartilage*, 12(1):65–73, 2004.

P Patwari, V Gaschen, IE James, E Berger, SM Blake, MW Lark, AJ Grodzinsky, and Ernst Bruno Hunziker. Ultrastructural quantification of cell death after injurious compression of bovine calf articular cartilage. *Osteoarthritis and cartilage*, 12(3): 245–252, 2004.

Parth Patwari, Michael N Cook, Michael A DiMicco, Simon M Blake, Ian E James, Sanjay Kumar, Ada A Cole, Michael W Lark, and Alan J Grodzinsky. Proteoglycan degradation after injurious compression of bovine and human articular cartilage in vitro: interaction with exogenous cytokines. *Arthritis & Rheumatism*, 48(5):1292–1301, 2003.

Parth Patwari, Debbie M Cheng, Ada A Cole, Klaus E Kuettner, and Alan J

Grodzinsky. Analysis of the relationship between peak stress and proteogly-can loss following injurious compression of human post-mortem knee and ankle cartilage. *Biomechanics and modeling in mechanobiology*, 6(1-2):83–89, 2007.

SS Pawaskar, ZM Jin, and J Fisher. Modelling of fluid support inside articular cartilage during sliding. *Proceedings of the Institution of Mechanical Engineers, Part J: Journal of Engineering Tribology*, 221(3):165–174, 2007.

Andrew D Pearle, Russell F Warren, and Scott A Rodeo. Basic science of articular cartilage and osteoarthritis. *Clinics in sports medicine*, 24(1):1–12, 2005.

Thomas M Quinn, Alan J Grodzinsky, Michael D Buschmann, Young-Jo Kim, and Ernst B Hunziker. Mechanical compression alters proteoglycan deposition and matrix deformation around individual cells in cartilage explants. *Journal of cell science*, 111(5):573–583, 1998a.

Thomas M Quinn, Alan J Grodzinsky, Ernst B Hunziker, and John D Sandy. Effects of injurious compression on matrix turnover around individual cells in calf articular cartilage explants. *Journal of orthopaedic research*, 16(4):490–499, 1998b.

Eric L Radin, Francois de Lamotte, and Paul Maquet. Role of the menisci in the distribution of stress in the knee. *Clinical orthopaedics and related research*, 185: 290–294, 1984.

Boris Reynaud and Thomas M Quinn. Anisotropic hydraulic permeability in compressed articular cartilage. *Journal of biomechanics*, 39(1):131–137, 2006.

V Roth and VC Mow. Finite element analysis of contact problems for indentation of articular cartilage. *Advances in Bioengineering*, pages 47–48, 1977.

Leonardo Ruggiero, Brandon K Zimmerman, Miri Park, Lin Han, Liyun Wang, David L Burris, and X Lucas Lu. Roles of the fibrous superficial zone in the mechanical behavior of tmj condylar cartilage. *Annals of biomedical engineering*, 43(11):2652–2662, 2015.

Robert L-Y Sah, Young-Jo Kim, Joe-Yuan H Doong, Alan J Grodzinsky, Anna HK Plass, and John D Sandy. Biosynthetic response of cartilage explants to dynamic compression. *Journal of Orthopaedic Research*, 7(5):619–636, 1989.

RB Salter, DF Simmonds, BW Malcolm, et al. The biological effects of continuous passive motion on the healing of full thickness defects in articular cartilage: an experimental investigation in the rabbit. *J Bone Joint Surg [Am]*, 62:1232–1251, 1980.

K Sauerland, RX Raiss, and J Steinmeyer. Proteoglycan metabolism and viability of articular cartilage explants as modulated by the frequency of intermittent loading. *Osteoarthritis and cartilage*, 11(5):343–350, 2003.

Oliver R Schätti, Michala Marková, Peter A Torzilli, and Luigi M Gallo. Mechanical loading of cartilage explants with compression and sliding motion modulates gene expression of lubricin and catabolic enzymes. *Cartilage*, 6(3):185–193, 2015.

Oliver R Schätti, Luigi M Gallo, and Peter A Torzilli. A model to study articular cartilage mechanical and biological responses to sliding loads. *Annals of biomedical engineering*, 44(8):2577–2588, 2016.

Oliver R Schätti, Vera Colombo, Peter A Torzilli, and Luigi M Gallo. Articular cartilage response to a sliding load using two different-sized spherical indenters. *Biorheology*, 54(2-4):109–126, 2018.

Robert M Schinagl, Donnell Gurskis, Albert C Chen, and Robert L Sah. Depth-dependent confined compression modulus of full-thickness bovine articular cartilage. *Journal of Orthopaedic Research*, 15(4):499–506, 1997.

DET Shepherd and BB Seedhom. Thickness of human articular cartilage in joints of the lower limb. *Annals of the rheumatic diseases*, 58(1):27–34, 1999.

R Shirazi, A Shirazi-Adl, and M Hurtig. Role of cartilage collagen fibrils networks in knee joint biomechanics under compression. *Journal of biomechanics*, 41(16):3340–3348, 2008.

Narendra K Simha, Hui Jin, Mellanie L Hall, Sidharth Chiravarambath, and Jack L Lewis. Effect of indenter size on elastic modulus of cartilage measured by indentation. *Journal of biomechanical engineering*, 129(5):767–775, 2007.

R Lane Smith, BS Donlon, MK Gupta, M Mohtai, P Das, DR Carter, J Cooke, G Gibbons, N Hutchinson, and DJ Schurman. Effects of fluid-induced shear on articular chondrocyte morphology and metabolism in vitro. *Journal of Orthopaedic Research*, 13(6):824–831, 1995.

R Lane Smith, SF Rusk, BE Ellison, P Wessells, K Tsuchiya, DR Carter, WE Caler, LJ Sandell, and DJ Schurman. In vitro stimulation of articular chondrocyte mrna and extracellular matrix synthesis by hydrostatic pressure. *Journal of orthopaedic research*, 14(1):53–60, 1996.

Michael A Soltz and Gerard A Ateshian. A conewise linear elasticity mixture model for the analysis of tension-compression nonlinearity in articular cartilage. *Journal of biomechanical engineering*, 122(6):576–586, 2000.

Alice J Sophia Fox, Asheesh Bedi, and Scott A Rodeo. The basic science of articular cartilage: structure, composition, and function. *Sports health*, 1(6):461–468, 2009.

J Soulhat, MD Buschmann, and A Shirazi-Adl. A fibril-network-reinforced bipha-
sic model of cartilage in unconfined compression. *Journal of biomechanical engi-
neering*, 121(3):340–347, 1999.

AD Speirs, PE Beaulé, KS Rakhra, ME Schweitzer, and H Frei. Bone density
is higher in cam-type femoroacetabular impingement deformities compared to
normal subchondral bone. *Osteoarthritis and Cartilage*, 21(8):1068–1073, 2013.

Andrew D Speirs, Paul E Beaulé, Stephen J Ferguson, and Hanspeter Frei. Stress
distribution and consolidation in cartilage constituents is influenced by cyclic
loading and osteoarthritic degeneration. *Journal of biomechanics*, 47(10):2348–
2353, 2014.

Andrew D Speirs, Paul E Beaulé, Adrian Huang, and Hanspeter Frei. Properties
of the cartilage layer from the cam-type hip impingement deformity. *Journal of
biomechanics*, 55:78–84, 2017.

Robert L Spilker, Jun-Kyo Suh, and Van C Mow. A finite element analysis of the in-
dentation stress-relaxation response of linear biphasic articular cartilage. *Journal
of biomechanical engineering*, 114(2):191–201, 1992.

Mats Stading and Robert Langer. Mechanical shear properties of cell-polymer car-
tilage constructs. *Tissue engineering*, 5(3):241–250, 1999.

Yubo Sun, David R Mauerhan, Jeffrey S Kneisl, H James Norton, Natalia
Zinchenko, Jane Ingram, Edward N Hanley Jr, and Helen E Gruber. Histological
examination of collagen and proteoglycan changes in osteoarthritic menisci. *The
open rheumatology journal*, 6:24, 2012.

Mihra S Taljanovic, Anna R Graham, James B Benjamin, Arthur F Gmitro, Eliza-
beth A Krupinski, Stephanie A Schwartz, Tim B Hunter, and Donald L Resnick.

Bone marrow edema pattern in advanced hip osteoarthritis: quantitative assessment with magnetic resonance imaging and correlation with clinical examination, radiographic findings, and histopathology. *Skeletal radiology*, 37(5):423–431, 2008.

R Teshima, T Otsuka, N Takasu, N Yamagata, and K Yamamoto. Structure of the most superficial layer of articular cartilage. *The Journal of bone and joint surgery. British volume*, 77(3):460–464, 1995.

Anika I Tsuchida, Michiel Beekhuizen, Marieke Ct Hart, Timothy RDJ Radstake, Wouter JA Dhert, Daniel BF Saris, Gerjo JVM van Osch, and Laura B Creemers. Cytokine profiles in the joint depend on pathology, but are different between synovial fluid, cartilage tissue and cultured chondrocytes. *Arthritis research & therapy*, 16(5):441, 2014.

A Unsworth, D Dowson, and V Wright. Some new evidence on human joint lubrication. *Annals of the Rheumatic Diseases*, 34(4):277, 1975.

JPG Urban. Present perspectives on cartilage and chondrocyte mechanobiology. *Biorheology*, 37(1, 2):185–190, 2000.

Wilmot B Valhmu, Enrico J Stazzone, Nathaniel M Bachrach, Fatemeh Saed-Nejad, Stuart G Fischer, Van C Mow, and Anthony Ratcliffe. Load-controlled compression of articular cartilage induces a transient stimulation of aggrecan gene expression. *Archives of Biochemistry and Biophysics*, 353(1):29–36, 1998.

Eric J Vanderploeg, Christopher G Wilson, and Marc E Levenston. Articular chondrocytes derived from distinct tissue zones differentially respond to in vitro oscillatory tensile loading. *Osteoarthritis and cartilage*, 16(10):1228–1236, 2008.

A Verteramo and BB Seedhom. Zonal and directional variations in tensile properties of bovine articular cartilage with special reference to strain rate variation. *Biorheology*, 41(3-4):203–213, 2004.

Nicole Verzijl, Jeroen DeGroot, Suzanne R Thorpe, Ruud A Bank, J Nikki Shaw, Timothy J Lyons, Johannes WJ Bijlsma, Floris PJG Lafeber, John W Baynes, and Johan M TeKoppele. Effect of collagen turnover on the accumulation of advanced glycation end products. *Journal of Biological Chemistry*, 275(50):39027–39031, 2000.

Christopher CB Wang, Jian-Ming Deng, Gerard A Ateshian, and Clark T Hung. An automated approach for direct measurement of two-dimensional strain distributions within articular cartilage under unconfined compression. *Journal of biomechanical engineering*, 124(5):557–567, 2002.

Guangye Wang, Wenjun Huang, Qi Song, and Jinfeng Liang. Three-dimensional finite analysis of acetabular contact pressure and contact area during normal walking. *Asian journal of surgery*, 40(6):463–469, 2017.

Xibin Wang, Paul A Manner, Alan Horner, Lillian Shum, Rocky S Tuan, and Glen H Nuckolls. Regulation of mmp-13 expression by runx2 and fgf2 in osteoarthritic cartilage. *Osteoarthritis and Cartilage*, 12(12):963–973, 2004.

Joanna F Weber and Stephen D Waldman. In situ and ex vivo biomechanical testing of articular cartilage. In *Experimental Methods in Orthopaedic Biomechanics*, pages 331–347. Elsevier, 2017.

W Wilson, JM Huyghe, and CC Van Donkelaar. Depth-dependent compressive equilibrium properties of articular cartilage explained by its composition. *Biomechanics and modeling in mechanobiology*, 6(1-2):43–53, 2007.

Wouter Wilson, CC Van Donkelaar, R Van Rietbergen, and R Huiskes. The role of computational models in the search for the mechanical behavior and damage mechanisms of articular cartilage. *Medical engineering & physics*, 27(10):810–826, 2005.

M Wong, P Wuethrich, MD Buschmann, P Eggli, and E Hunziker. Chondrocyte biosynthesis correlates with local tissue strain in statically compressed adult articular cartilage. *Journal of Orthopaedic Research*, 15(2):189–196, 1997.

Marcy Wong, Mark Siegrist, and Xuesong Cao. Cyclic compression of articular cartilage explants is associated with progressive consolidation and altered expression pattern of extracellular matrix proteins. *Matrix Biology*, 18(4):391–399, 1999.

SL-Y Woo, P Lubock, MA Gomez, GF Jemmott, SC Kuei, and WH Akeson. Large deformation nonhomogeneous and directional properties of articular cartilage in uniaxial tension. *Journal of biomechanics*, 12(6):437–446, 1979.

Fumiko Yamairi, Hiroyuki Utsumi, Yuuichi Ono, Naruyasu Komorita, Masaharu Tanaka, and Atsushi Fukunari. Expression of vascular endothelial growth factor (vegf) associated with histopathological changes in rodent models of osteoarthritis. *Journal of toxicologic pathology*, 24(2):137–142, 2011.

Wenbo Zhu, Van C Mow, Thomas J Koob, and David R Eyre. Viscoelastic shear properties of articular cartilage and the effects of glycosidase treatments. *Journal of Orthopaedic Research*, 11(6):771–781, 1993.

Appendix A

A.1 Mesh Sensitivity Analysis

In finite element analysis, mesh sensitivity study is performed to track the influence of the mesh on the predicted results. That involves continues mesh refinement until a critical result, (i.e. Max pore pressure), does not change significantly with mesh refinement. That usually requires series of runs with different number of elements before satisfactory mesh density is determined. Therefore and for computational efficiency this analysis is normally conducted by mean of 2D or axisymmetric models.

However, FEBio does not support 2D axisymmetric elements; thus, using a single wedge (slice) out of the 3D geometry and a properly aligned symmetry plane, Figure A.1, an axisymmetric analysis can be simulated. For detailed instructions on creating this geometry in Preview, please refer to (Preview User Manual 2.0, Section 2.9, Tutorial 9: Axisymmetric analysis of biphasic indentation).
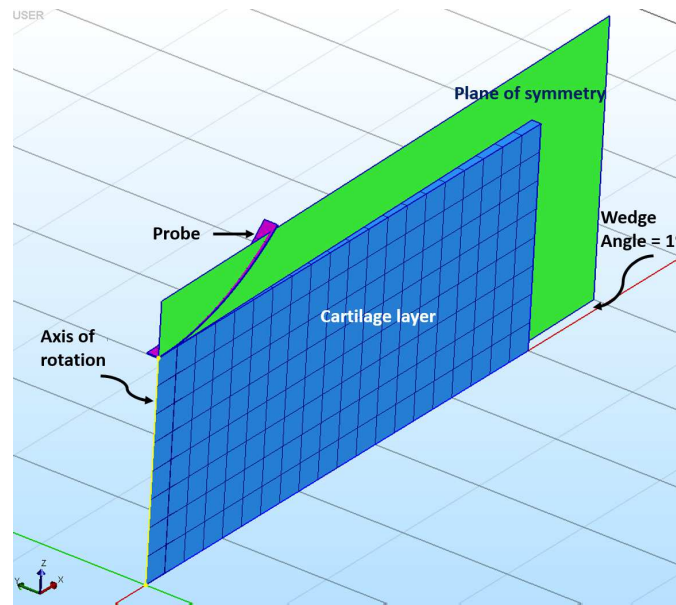
Figure A.1: Simulating axisymmetric analysis in FEBio using wedge geometry.

An initial mesh convergence study is then preformed by reducing the size of elements by half while monitoring the associated change in the peak of the fluid pressure. The adopted mesh density is decided when the change in the maximum fluid pressure caused by doubling the meshes is less than 5%. As can be seen from Table A.1 and Figure A.2, mesh refinement in model 4 resulted in difference of only 1% from the model 3. Therefore, model 3 with total number of element of 640 was adopted.

Table A.1: Results of the initial mesh sensitivity study.

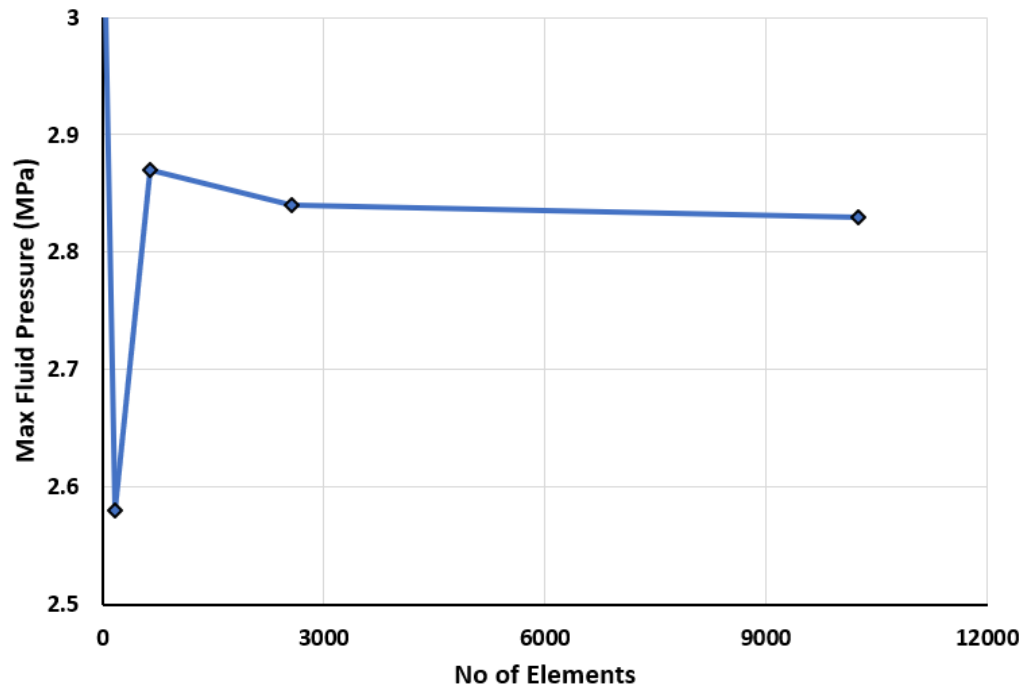| Model (No of elements)	Element size (mm)	Max fluid pressure (MPa)	Error (%)
1 (40)	0.5	3.01	–
2 (160)	0.25	2.58	14.28
3 (640)	0.125	2.87	11.24
4 (2560)	0.0625 0	2.84	1.04
5 (10240)	0.03125	2.83	0.35

Figure A.2: Maximum fluid pressure obtained from each model in mesh sensitivity study.

It should be noted that the mesh of all models presented in this thesis was re-fined in the loaded regions and near the cartilage surface to capture the expected rapid change in fluid pressure and tissue deformation. That resulted in further reduction in computational time with results still in the acceptable range. For ex-ample, the number of elements of model 3 adopted for this mesh sensitivity study can be reduced by more than 50% using biased mesh in both X and Z directions. As cab be seen in Figure A.3, the maximum fluid pressure was further reduced by $\sim$ 2.5% due to biased mesh which allowed for reducing the total number of element from 640 to 300), which is significant.
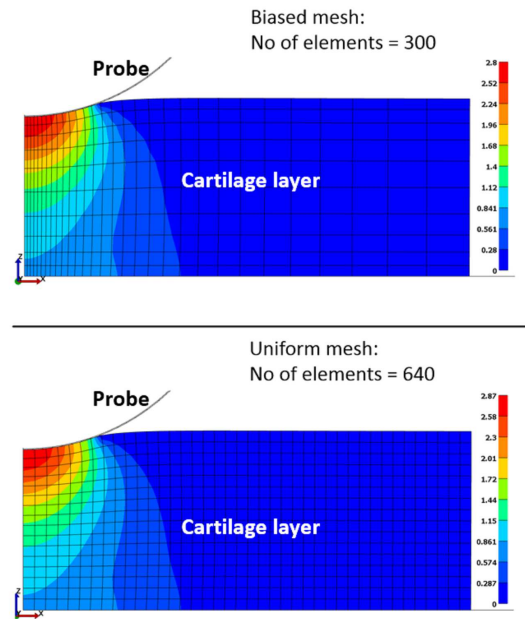
Figure A.3: Predicted fluid pressure using uniform and biased meshes.

It should also be noted that the newer FEBio versions (R E L E A S E 2.7.0 and up) have implemented a new symmetry plane feature that allowed for modeling axisymmetric problem without the need for creating the actual geometry of the symmetry plane.

Sample of FEBio .feb file for sliding contact model:

```xml
<?xml version="1.0" encoding="ISO-8859-1"?>
<febio_spec version="2.5">
    <Module type="biphasic"/>
    <Control>
        <time_steps>1020</time_steps>
        <step_size>0.1</step_size>
        <max_refs>15</max_refs>
        <max_ups>0</max_ups>
        <diverge_reform>1</diverge_reform>
        <reform_each_time_step>1</reform_each_time_step>
        <dtol>0.001</dtol>
        <etol>0.01</etol>
        <rtol>0</rtol>
        <ptol>0.01</ptol>
        <lstol>0.9</lstol>
        <min_residual>1e-020</min_residual>
        <qnmethod>0</qnmethod>
        <time_stepper>
            <dtmin>0.01</dtmin>
            <dtmax lc="1"></dtmax>
            <max_retries>5</max_retries>
            <opt_iter>10</opt_iter>
        </time_stepper>
        <symmetric_biphasic>0</symmetric_biphasic>
    </Control>
    <Globals>
        <Constants>
            <T>0</T>
            <R>0</R>
            <Fc>0</Fc>
        </Constants>
    </Globals>
    <Material>
        <material id="1" name="indenter" type="rigid body">
            <density>1</density>
            <center_of_mass>0,0,0</center_of_mass>
        </material>
        <material id="2" name="AC" type="biphasic">
            <phi0>0.2</phi0>
            <fluid_density>1</fluid_density>
            <solid type="solid mixture">
                <solid type="neo-Hookean">
                    <density>1</density>
                    <E>0.395</E>
                    <v>0.1</v>
                </solid>
                <solid type="spherical fiber distribution">
                    <alpha>0</alpha>
                    <beta>2</beta>
                    <ksi>0.188</ksi>
                </solid>
            </solid>
            <permeability type="perm-const-iso">
                <perm>0.00367</perm>
            </permeability>
        </material>
    </Material>




    <Geometry>
        <Nodes name="indenter">
            Nodes coordinates section
        </Nodes>
        <Nodes name="AC">
            Nodes coordinates section
        </Nodes>
        <Elements type="hex8" mat="1" name="Part27">
            Include elements
        </Elements>
        <Elements type="penta6" name="AC">
            Include elements
        </Elements>
        <Surface name="BiphasicContact01_master">
                </Surface>
        </Surface>
        <Surface name="BiphasicContact01_slave">
                </Surface>
        </Surface>
        <SurfacePair name="BiphasicContact01">
            <master surface="BiphasicContact01_master"/>
            <slave surface="BiphasicContact01_slave"/>
        </SurfacePair>
    </Geometry>
    <Boundary>
        <fix bc="p" node_set="FixedFluidPressure"/>
        <fix bc="y" node_set="FixedDisplacement_Y"/>
        <fix bc="x,y,z" node_set="FixedDisplacement"/>
        <rigid_body mat="1">
            <fixed bc="y"/>
            <fixed bc="Rx"/>
            <fixed bc="Ry"/>
            <fixed bc="Rz"/>
        </rigid_body>
        <rigid_body mat="1">
            <force bc="z" lc="2">0.5</force>
        </rigid_body>
        <rigid_body mat="1">
            <prescribed bc="x" lc="3">1</prescribed>
        </rigid_body>
    </Boundary>
    <Contact>
        <contact type="sliding-biphasic" name="BiphasicContact01" surface_pair="BiphasicContact01">
            <laugon>1</laugon>
            <tolerance>0.05</tolerance>
            <gaptol>0</gaptol>
            <ptol>0</ptol>
            <penalty>0.2</penalty>
            <two_pass>0</two_pass>
            <auto_penalty>1</auto_penalty>
            <pressure_penalty>0.1</pressure_penalty>
            <symmetric_stiffness>0</symmetric_stiffness>
            <search_radius>1</search_radius>
            <seg_up>0</seg_up>
            <minaug>0</minaug>
            <maxaug>10</maxaug>
            <search_tol>0.01</search_tol>
        </contact>
    </Contact>
```

```
<LoadData>
        <loadcurve id="1" type="step">
                <point>0,0</point>
                <point>2,0.1</point>
                <point>3,0.2</point>
                        :
                        :
                <point>102,0.2</point>
        </loadcurve>
        <loadcurve id="2" type="linear">
                <point>0,0</point>
                <point>2,-0.16</point>
                <point>102,-0.16</point>
        </loadcurve>
        <loadcurve id="3" type="linear">
                <point>0,0</point>
                <point>2,0</point>
                <point>3,3</point>
                <point>4,0</point>
                <point>5,-3</point>
                <point>6,0</point>
                        :
                        :
                <point>102,0</point>
        </loadcurve>
</LoadData>
<Output>
        <plotfile type="febio">
                <var type="contact gap"/>
                <var type="contact pressure"/>
                <var type="contact traction"/>
                <var type="displacement"/>
                <var type="reaction forces"/>
                <var type="relative volume"/>
                <var type="stress"/>
                <var type="effective fluid pressure"/>
                <var type="fluid pressure"/>
                <var type="fluid flux"/>
        </plotfile>
</Output>
</febio_spec>
```

A.2   Motor Power Calculation

Calculating the torque required by the stepper motor to drive the ball screw at constant speed. The relative motion between the sample and the indenter is initiated by the linear motion of the ball screw to which the indenter is attached. The ball screw is operated by mean of a stepper motor. The torque against which the motor must act is given by:

$$T_c = T_d + T_p + T_f \qquad (A.1)$$

Where:

T_c = Torque at constant speed (Nm).

T_d = Torque to drive the load (Nm).

T_p = Torque due to preload (provided by manufacturer) (Nm).

T_f = Torque due to friction of support bearings (provided by manufacturer) (Nm).

However, the drive torque is primarily influenced by the axial load on the screw

and the screws' lead.

$$T_d = F_a.P/2.\pi.\eta \tag{A.2}$$

Where:

P = Lead (12mm).

η = Efficiency of ball screw (90%), but taken to be 40% as the worst case scenario.

$F_a = F + W * \mu$ (N)

Where: F = Total axial force (N), W the load applied to the cartilage, and μ is the friction between the indenter and the cartilage sample.

The weight of the vertical stand, cantilever beam, indenter, linear guide, and max of additional weights of 100 g were found to be ~ 5 N. The friction between indenter and healthy cartilage could be neglected, but to allow for the possibility of testing degenerated cartilage in the future, μ was taken to be 1 and maximum load of 2.5 N.

Therefore:

$F_a = 5 + 2.5 = 7.5$ (N), and Hence:

$T_d \simeq 0.035$ ($N.m$)

Therefore, the chosen motor (NEMA 23) with torque of 0.54 $N.m$ is sufficient.

A.3 Sample Preparation

Human osteochondral plugs were cut by the surgeon inside the operating room; however, sample were later prepared for mechanobiological testing by removing the cartilage layer off the bone and sample were cut at the required dimensions.

Therefore, this procedure describes the procedure used to prepare bovine cartilage samples used for biomechanical testing in this thesis. osteochondral bovine plugs were harvested from freshly slaughtered bovine tibial plateaus obtained from a local butchery. Tibiofemoral joints were chosen due their large radius of curvature which allows for cutting samples with relatively flat surface especially from tibial plateau. As discussed in Section 3.3.2, the specimen clamp was designed to fit cartilage plugs of diameter $10 - 15$ *mm* and minimum thickness of 5 *mm*. Hence, $5 - 6$ *mm* of bone layer were left such that complete cartilage layer sticks above the cartilage clamp. This should eliminate any stresses could result from the clamping mechanism on the cartilage tissue. The following procedure summarizes steps taken to obtain specimens at the required dimensions and intact cartilage surface:

- First, tibiofemoral joints were opened and carefully inspected for any visual sign of fibrillation or damage that might be present. Only joints with healthy appearance and smooth cartilage surface were selected.

Figure A.4: cartilage with adequate bone layer is removed of the joint.

- The tibia was then mounted on a bench vise where the meniscus and other tissue are removed. Then, the tibia is sawed horizontally at 8-10 mm below

the joint surface using *Dremel Multi Max MM40* saw to obtain adequate bone layer below the cartilage surface, as in Figure A.4.

- Then, a surgical stainless steel trephine, diameter of 10 *mm* was used to slowly bore through the cartilage thin layer and approximately $6 - 8$ *mm* into the subchondral bone. To ensures that the cartilage margins are not overheated during the cutting process, the tissue was kept moisturized by continuous flow of PBS solution.

- The cutting tool was then slowly pulled out without breaking the cartilage plug. Sometimes, multiple specimens can be drilled out from the same joint as in Figure A.5A.

- After that, osteochondral plugs were removed by pushing them out from the bottom side. In some cases the saw was used to open the bone and remove the samples. Depending on the shape of the joint and the horizontal cutting, the obtained plugs may become in different thicknesses with non-flat surfaces from the bone side, see Figure A.5B.
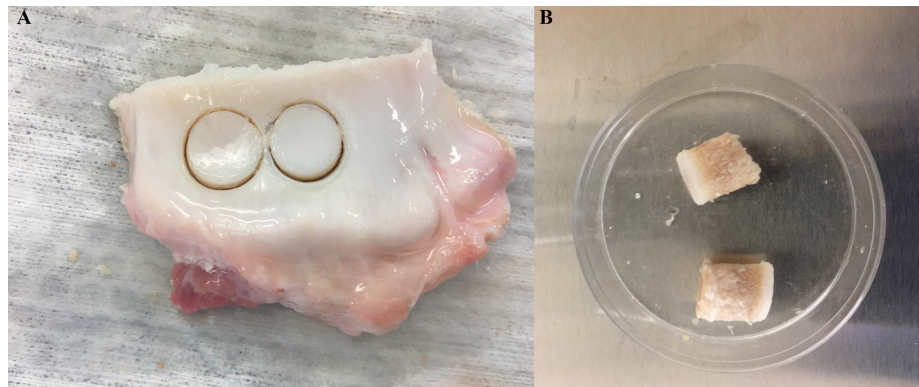
Figure A.5: Cutting the sample out of the cartilage-bone layer.

- Therefore, a rotary saw, Buehler Isomet, was used to trim the samples to the required thickness, minimum of $5 - 6$ *mm* of the bone, and ensure a flat

surface at the bone side. The rotary saw was operated at low speed while the specimen is is clamped using specimen holder.

Figure A.6: Rotary saw is used to trim off the subchondral bone and obtain flat surface on the bone side.

- In most cases, the rotary saw cut produced flat surface from the bone side; however, a sand paper was used to further smooth the samples' lower side when necessary.

- The final osteochondral plugs should all be at 10 mm diameter and $5 - 6\ mm$ thickness. The final shape of the specimen is shown in Figure A.7.

Figure A.7: Cutting the sample out of the cartilage-bone layer.

A.4   System Operating Procedure

Before any experiment can be performed using this apparatus, the user need to make sure that all wires are properly connected, and the stepper motor drive is correctly set.

- Connect both encoders to the micro-controller and manually move the cantilever beam and the lead screw to make sure that both encoders and force sensor outputs are received by the micro-controller.

- To ensure that the current designated by the drive is appropriate for the motor, set the rotary motor switch to 3 and dip-switch 1 and 2 down as shown in the figure below.
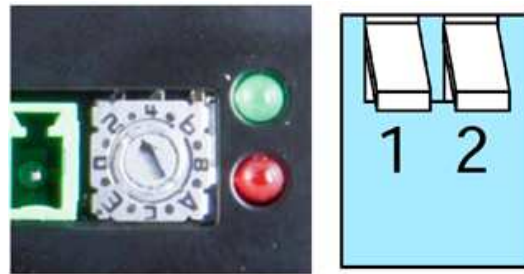
Figure A.8: Setting the motor current.

- The used stepper motor has 1.8º step angle, which makes 200 steps/ rev. Using switches 5, 6, and 7, the motor drive can be set to produce a smaller step size as shown in figure 2. Please refer to the STR 4 & 8 hardware manual, pages number 20 - 21, for more information about the motor drive step size setting.
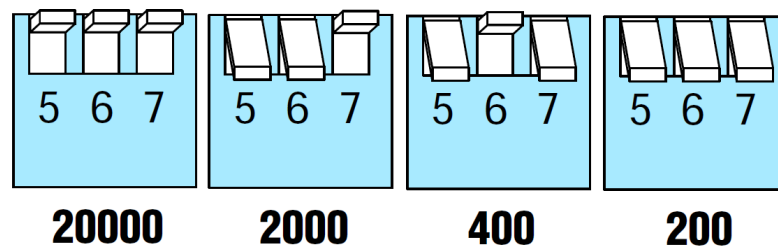
Figure A.9: Setting the motor step size.

- After deciding the on the step size, using table in the appendix A, calculate the required time delay between micro-controller pluses, to achieve the desired sliding speed.

- It is highly recommended to dry-run the system to ensure that all wires are connected and components are working as required.

- Cut the cartilage specimen as described in section x and firmly secure it in the specimen clamp and in the BPS bath.

- Place the PBS bath in its location on the specimen bath base and fill it with BPS to cover the specimen surface by 2-3 mm.

- Note the change in the force sensor output due the increased PBS bath weight.

- Wait for $\sim$ 5 minutes until the force sensor output settle. Take the value and code it in the motor micro-controller program.

- Left the indenter up and manually move the monocarrier while monitoring the horizontal encoder reading. Stop at encoder reading zero which represents the center of the cartilage specimen.

- Gently lower the cantilever beam and place the indenter on the cartilage surface. The actual start time of the test is determined by the change in the force sensor as the indenter tip reaches the cartilage surface.

- Now the test begins, outputs from both encoders and force sensor readings must be collected to a text file. The motor will start running after the initial loading step time that has been already prescribed in the micro-controller program.

- When the experiment is completed, stop collecting the data, turn off the motor drive, rise the indenter, and manually drive the monocarrier to bring the indenter out of the PBS bath.

- A second test or cartilage thickness measurement can be performed after allowing the sample to recover for a minimum time of 30 minutes.

A.5 Mechanobiological Testing Results
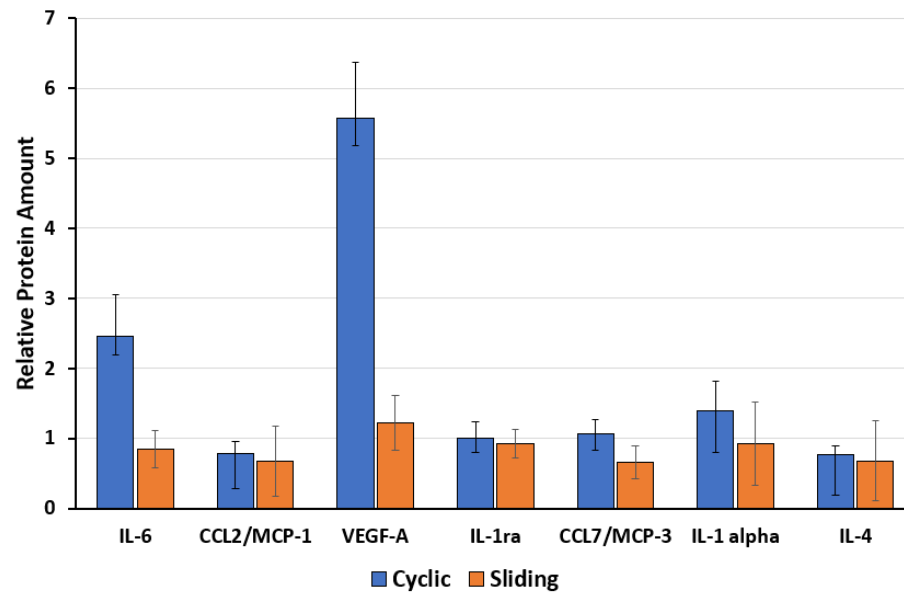
Figure A.10: The relative expression of cytokines in FNF "healthy" specimens. Results were normalized to control represented by red dashed line.
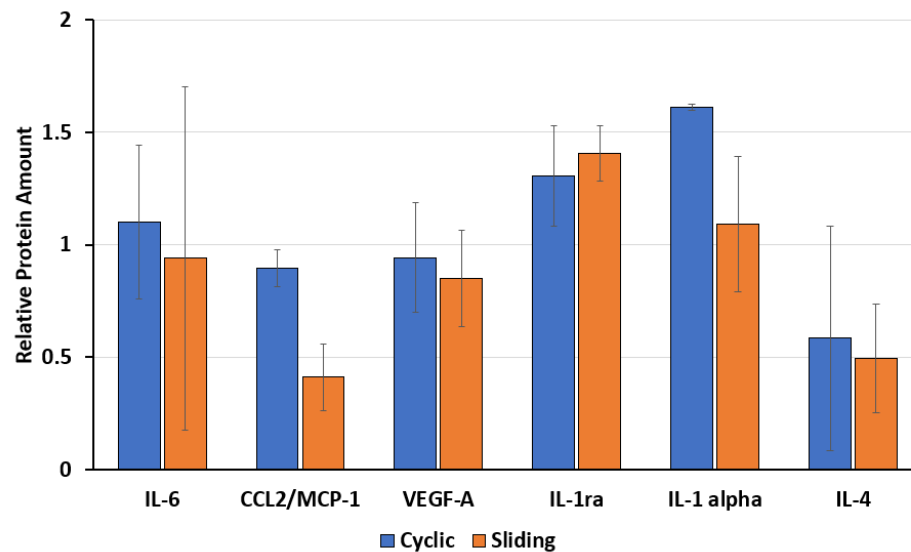
Figure A.11: The relative expression of cytokines in OA "osteoarthritis" specimens. Results were normalized to control.
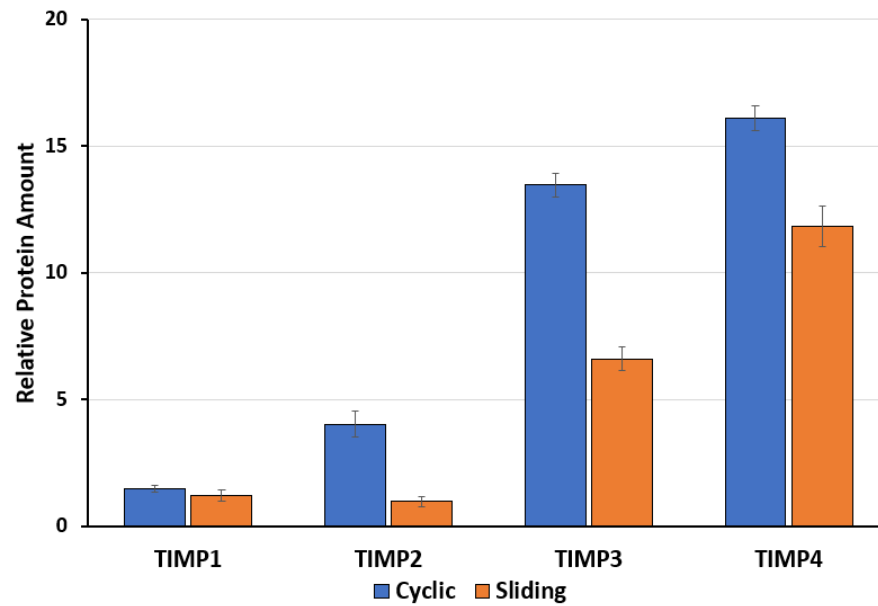
Figure A.12: The relative expression of TIMPs in FNF "healthy" specimens. Results were normalized to control.
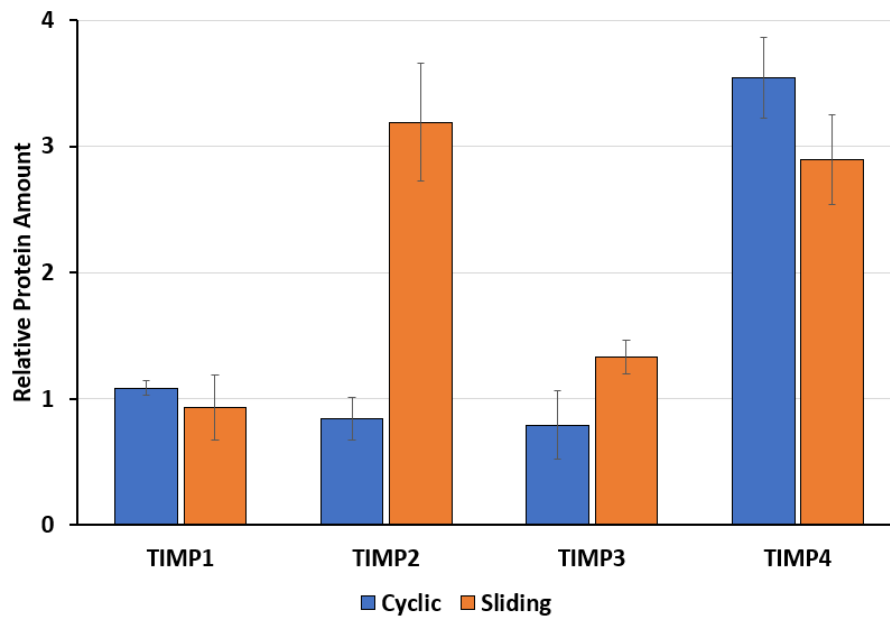
Figure A.13: The relative expression of TIMPs in OA "osteoarthritis" specimens. Results were normalized to control.

Appendix B

Engineering Drawings

B.1 Engineering Drawings for Bi-axial Apparatus

Section No.	Description
1	Specimen bath and clamping mechanism
2	Loading and displacement measurement section
3	Sliding motion section
4	Base

* Detailed views and drawings of the essential parts are to follow.
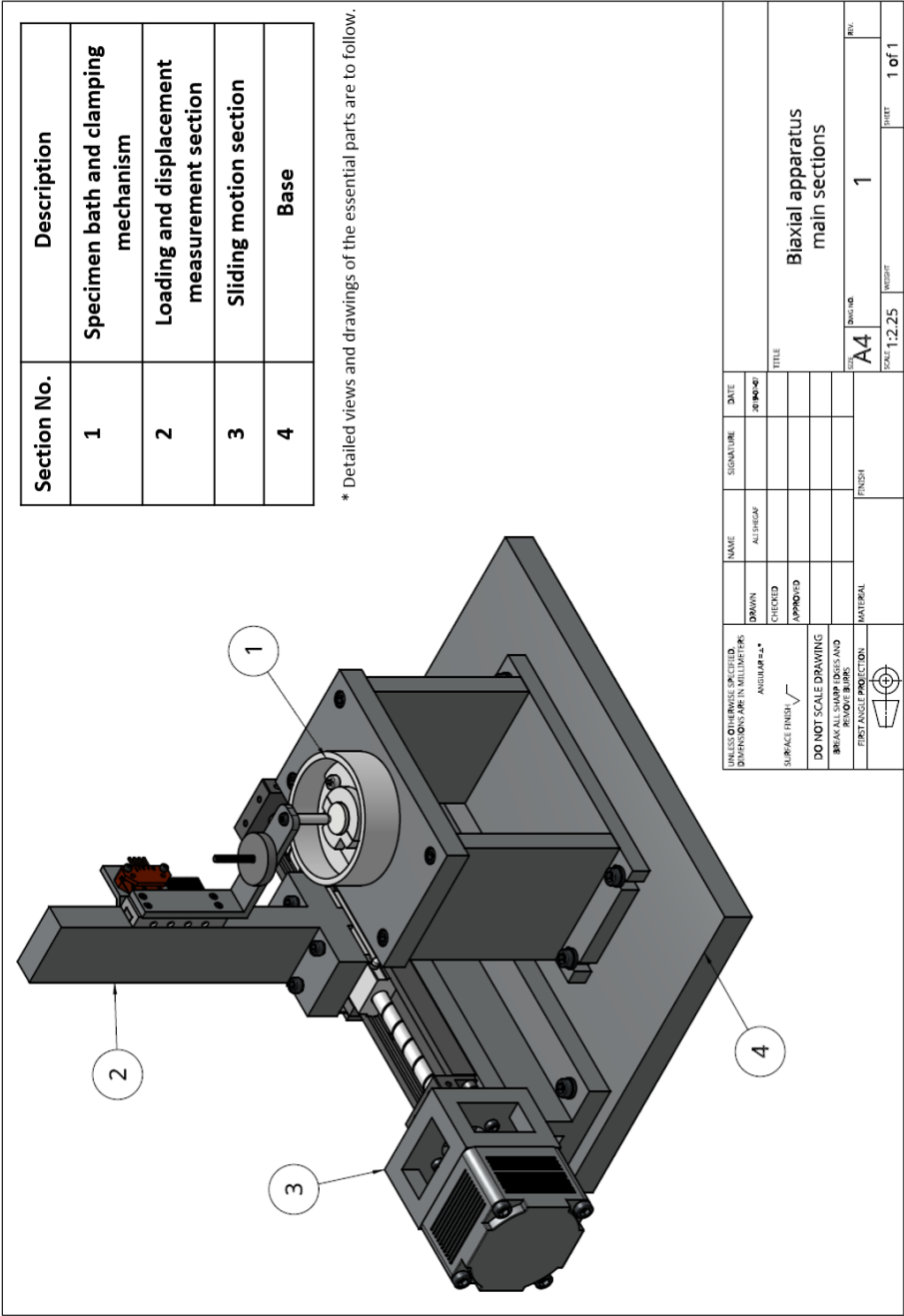
Figure B.1: Biaxial apparatus divided into four main sections.

Item No.	Quantity	Part name	Part No.
1	1	Specimen bath	PRT 1.1.1
2	1	Specimen clamp A	PRT 1.1.2
3	1	Specimen clamp A	PRT 1.1.3
4	2	M2 bolt	--
5	1	Tested specimen	--
6	2	M2 bolt	--
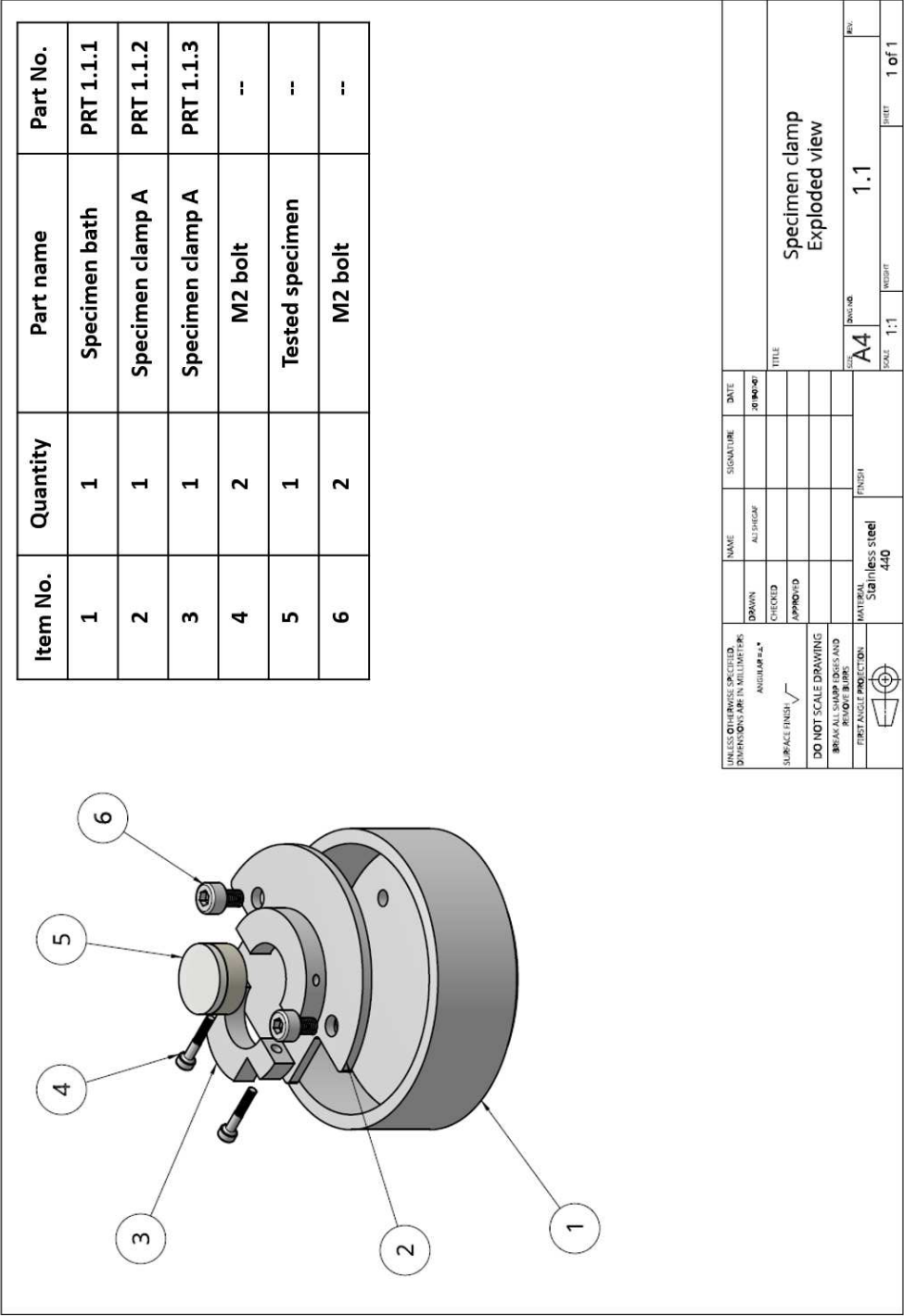
Figure B.2: Exploded view of the specimen bath and clamping mechanism section.
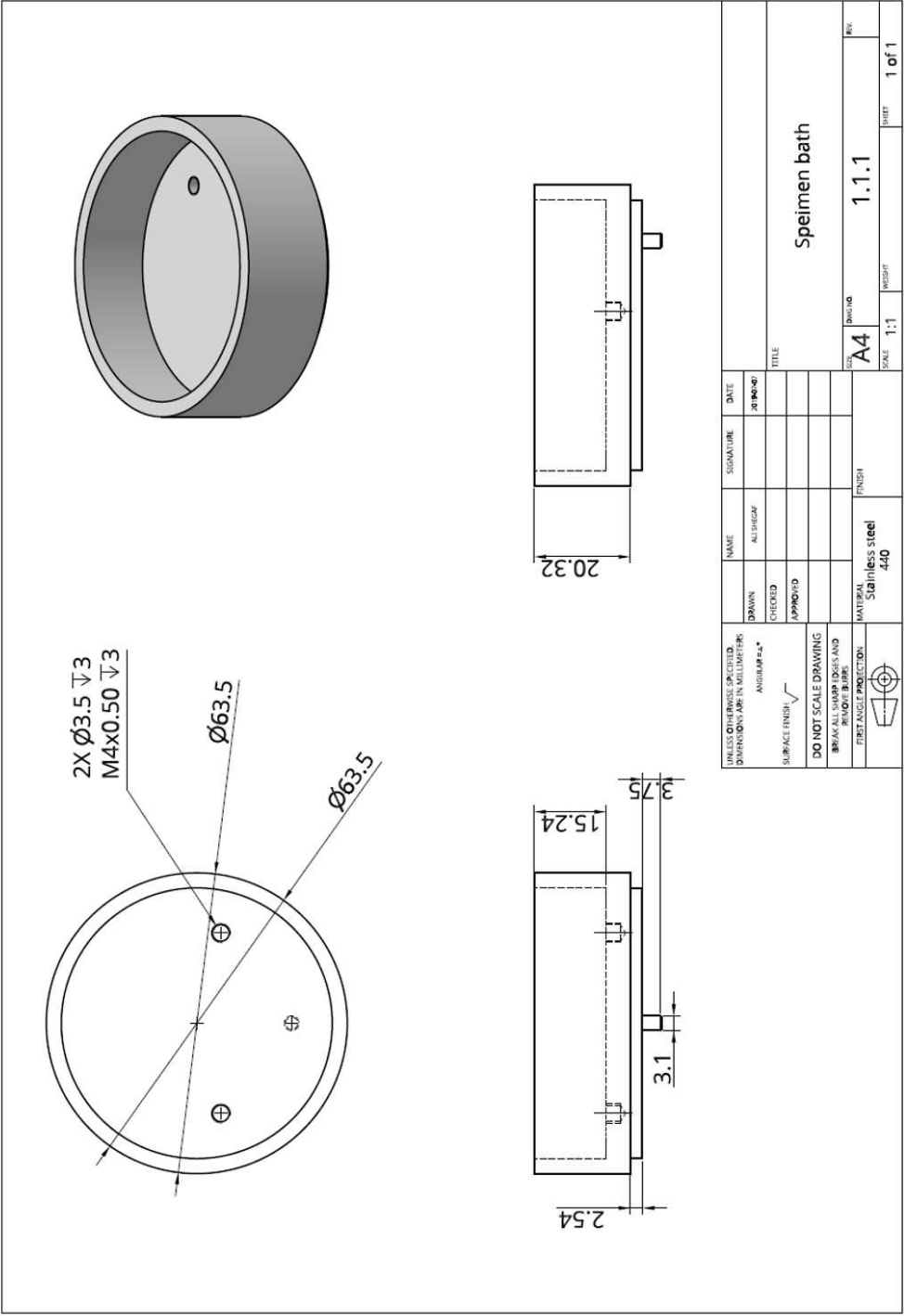
Figure B.3: Specimen bath.
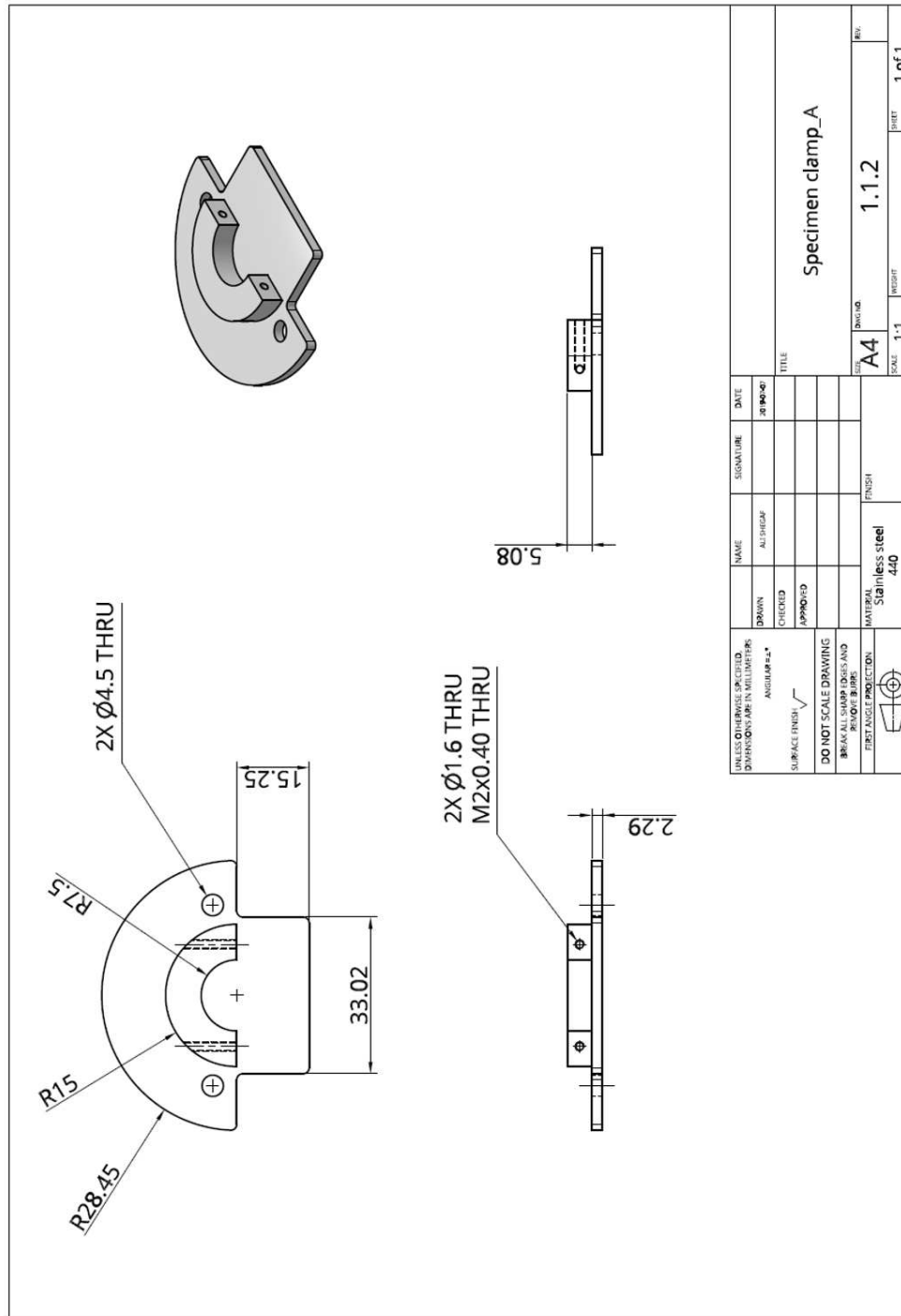
Figure B.4: Specimen clamp: part A.
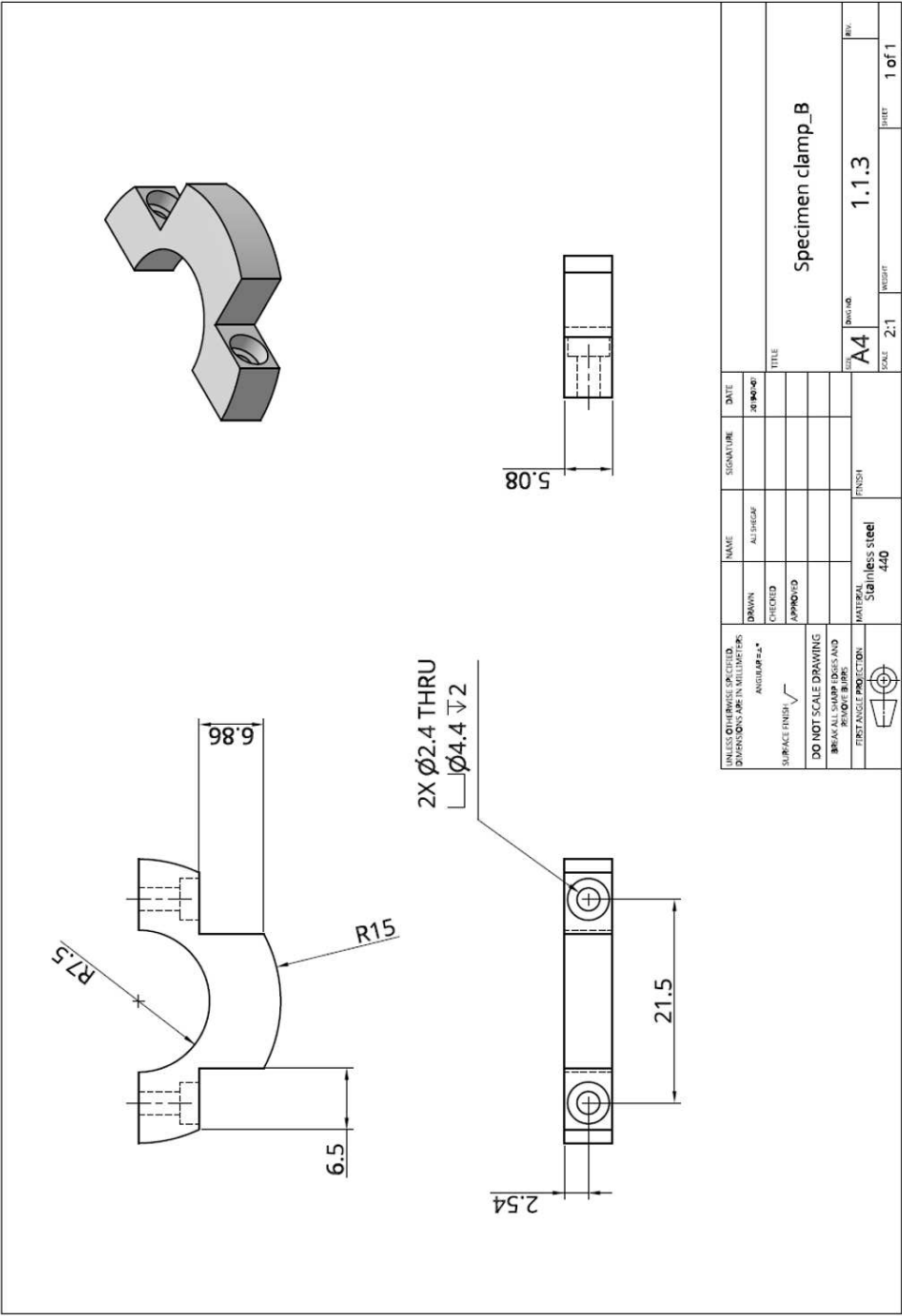
Figure B.5: Specimen clamp: part B.

Item No.	Quantity	Part name	Part No.
1	1	Spherical-end indenter	PRT 1.2.1
2	1	Cantilever beam	PRT 1.2.2
3	--	Metallic weight	--
4	2	EM2 Encoder	--
5	4	M2 bolt	--
6	4	M3 bolt	--
7	1	Vertical stand	PRT 1.2.3
8	1	Ball slide	--
9	1	Encoder holder	PRT 1.2.4
10	2	M3 bolt	--
11	2	Encoder strip	--
12	4	M2 bolt	--
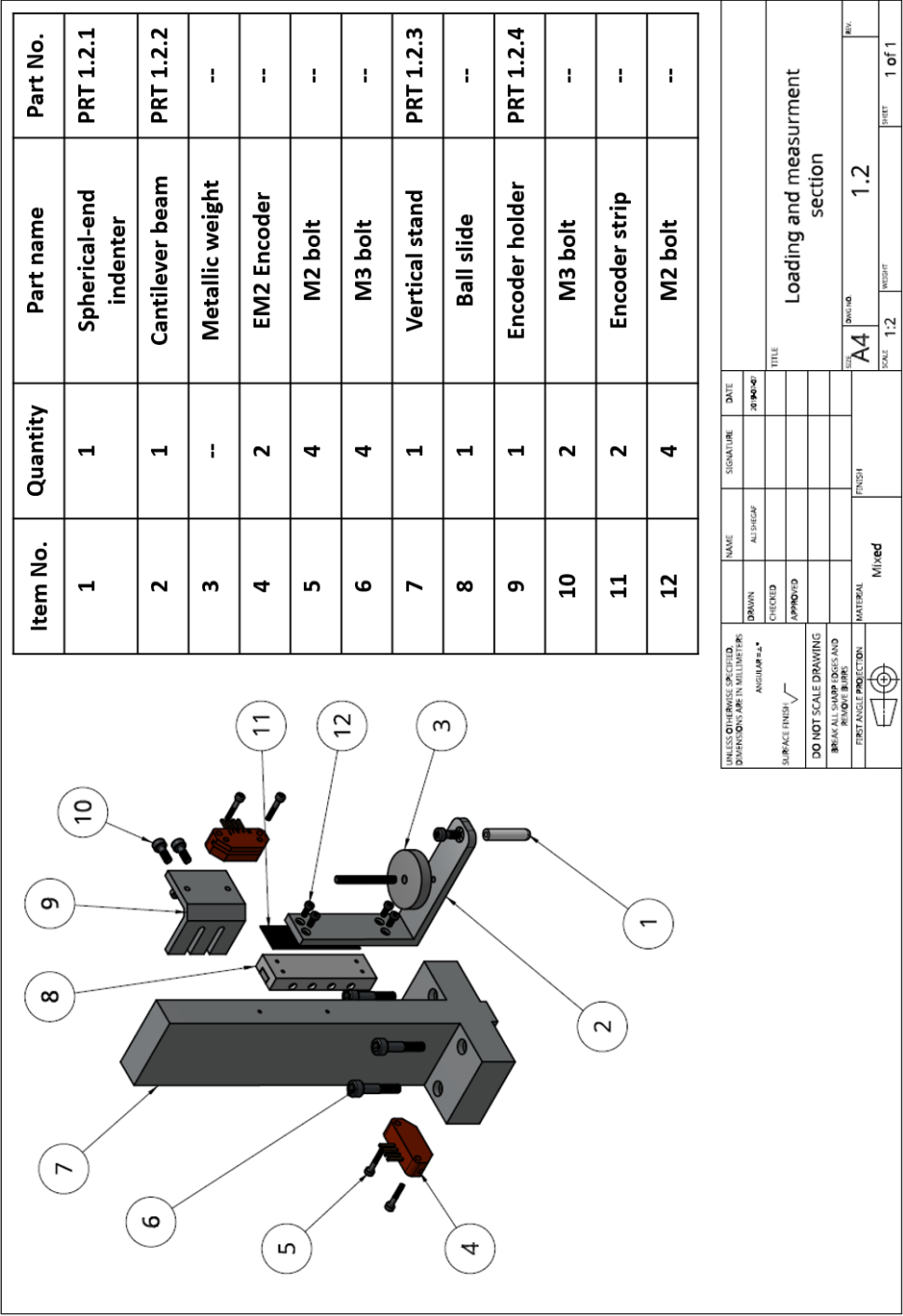
Figure B.6: Exploded view of the loading and measurement section.
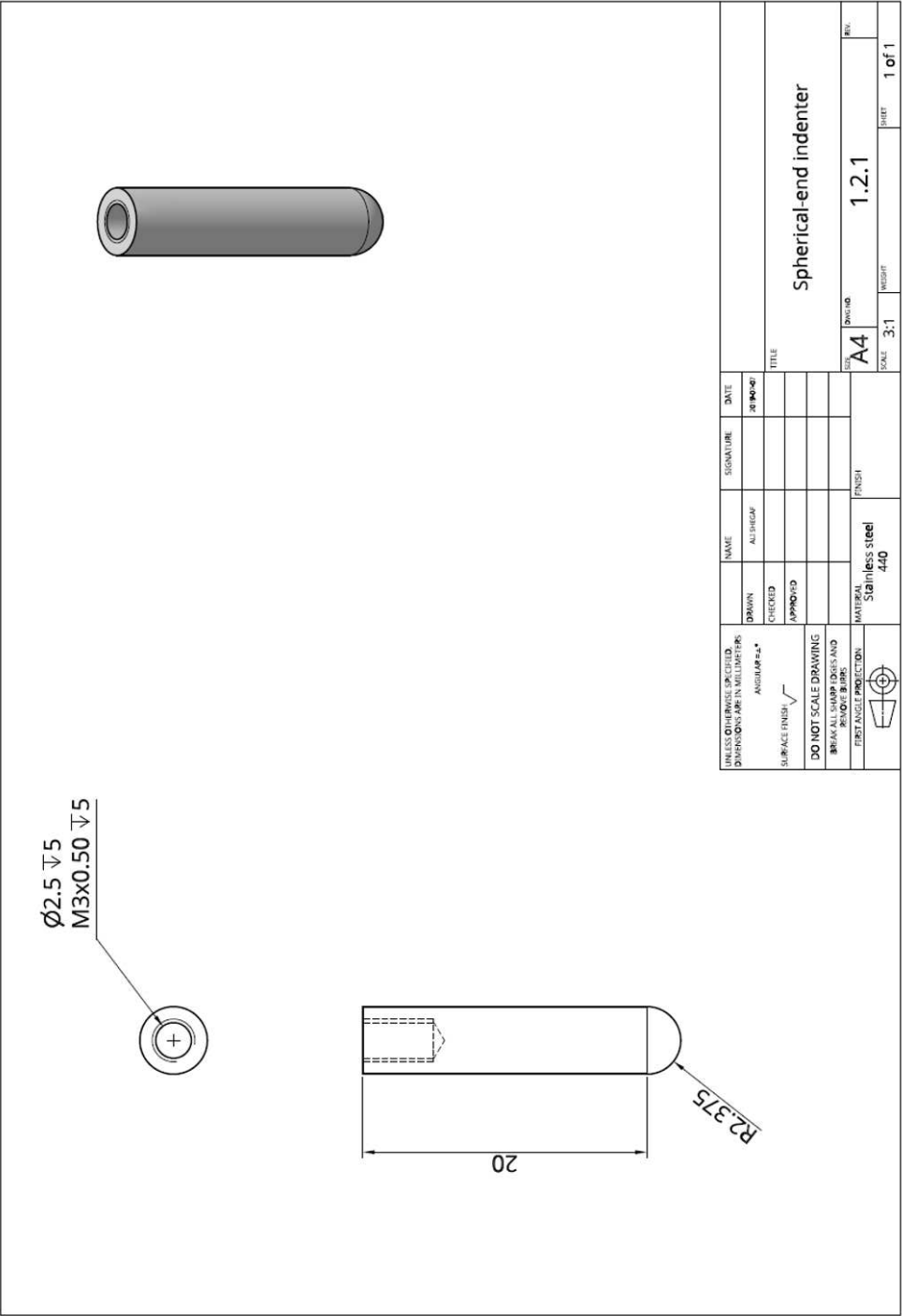
Figure B.7: Spherical-end indenter.
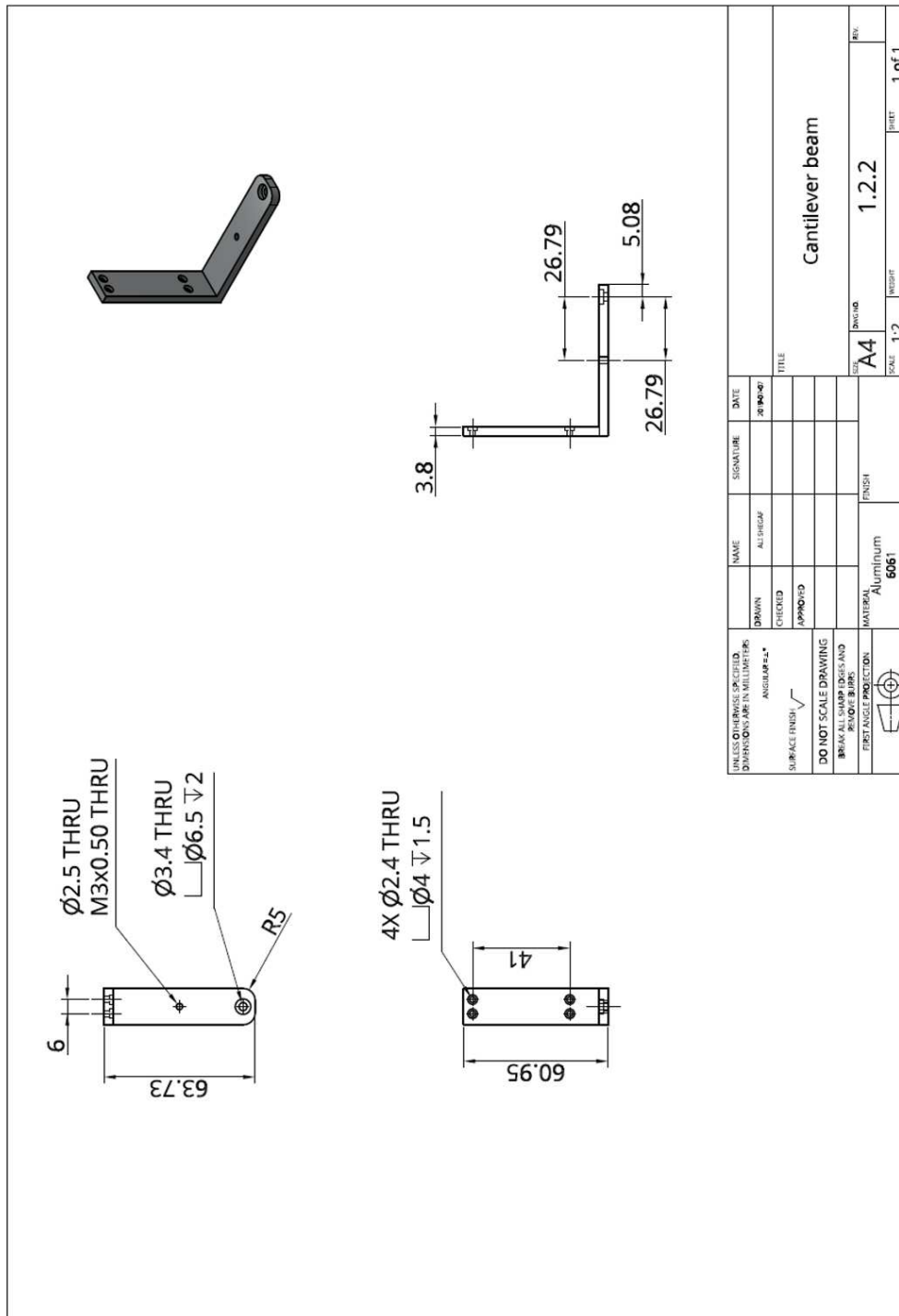
Figure B.8: cantilever beam.
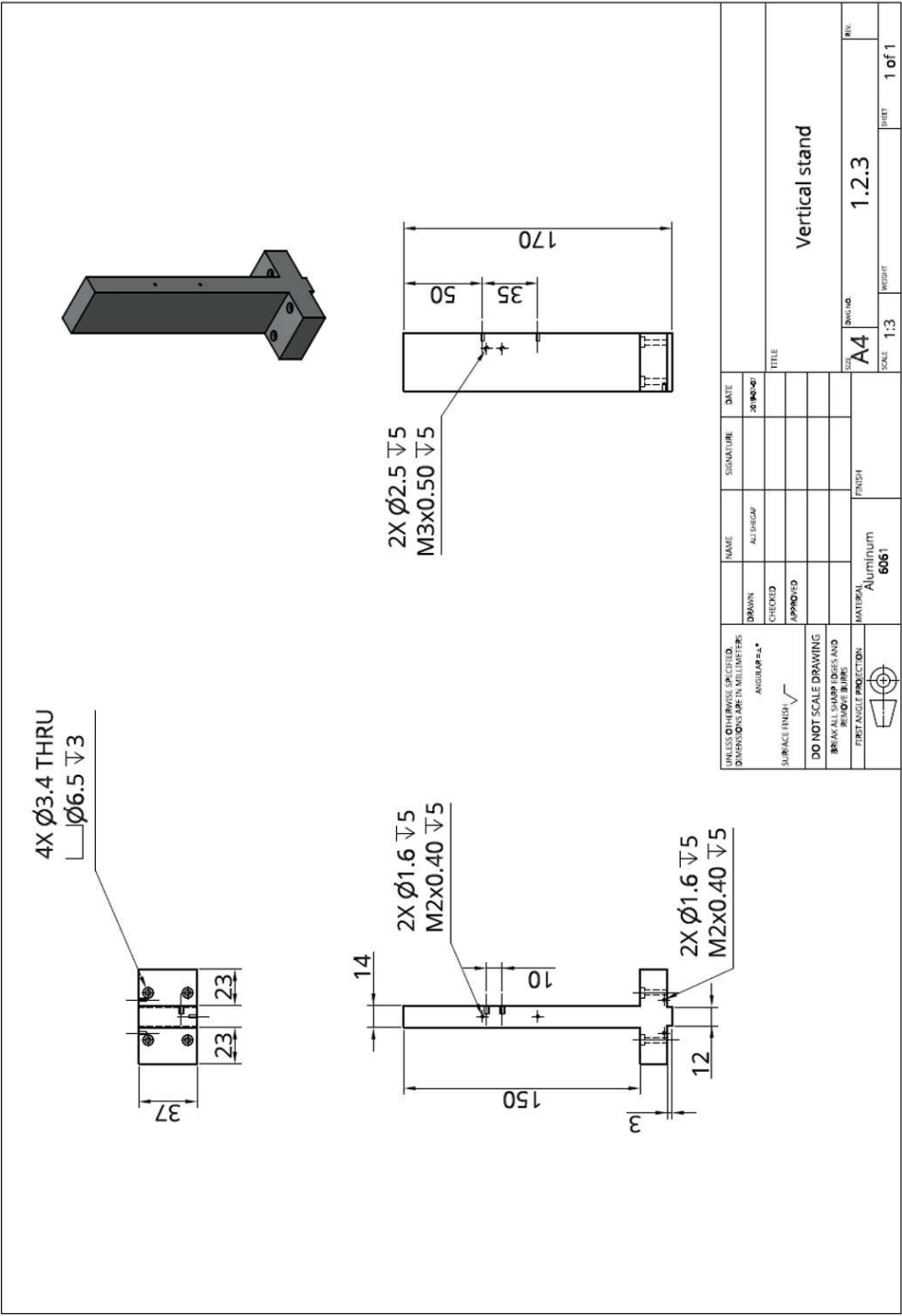
Figure B.9: Vertical stand.
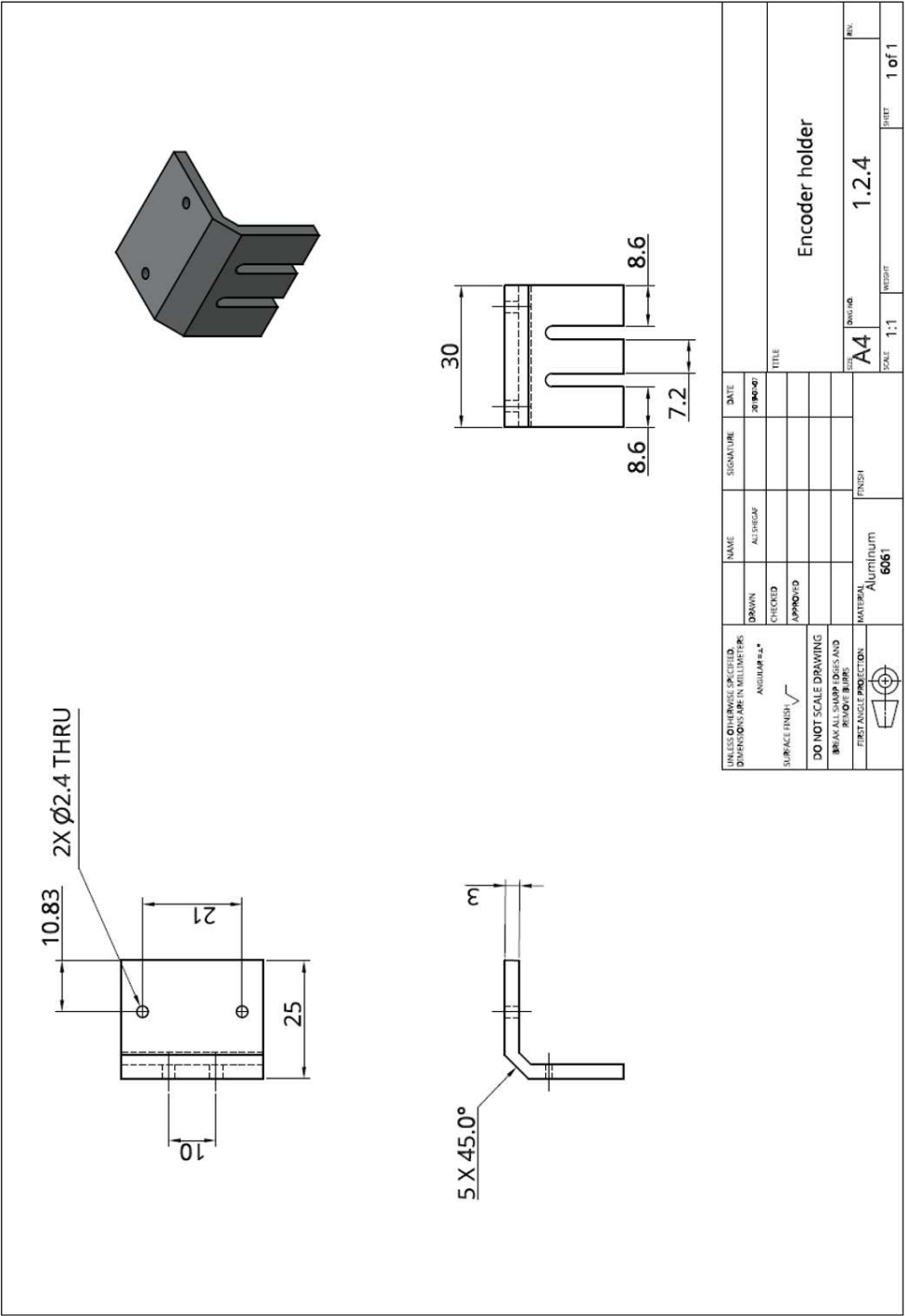
Figure B.10: Encoder holder.

Item No.	Quantity	Part name	Part No.
1	1	Ball screw Model No: MCM03010H12K	--
2	2	M2 blot	--
3	4	M3 blot	--
4	1	Nema 23 stepper motor	--
5	4	M5 blot	--
6	1	stepper motor - Ball screw connector	PRT 1.3.2
7	1	Shaft coupler	PRT 1.3.3
8	10	M4 blot	--
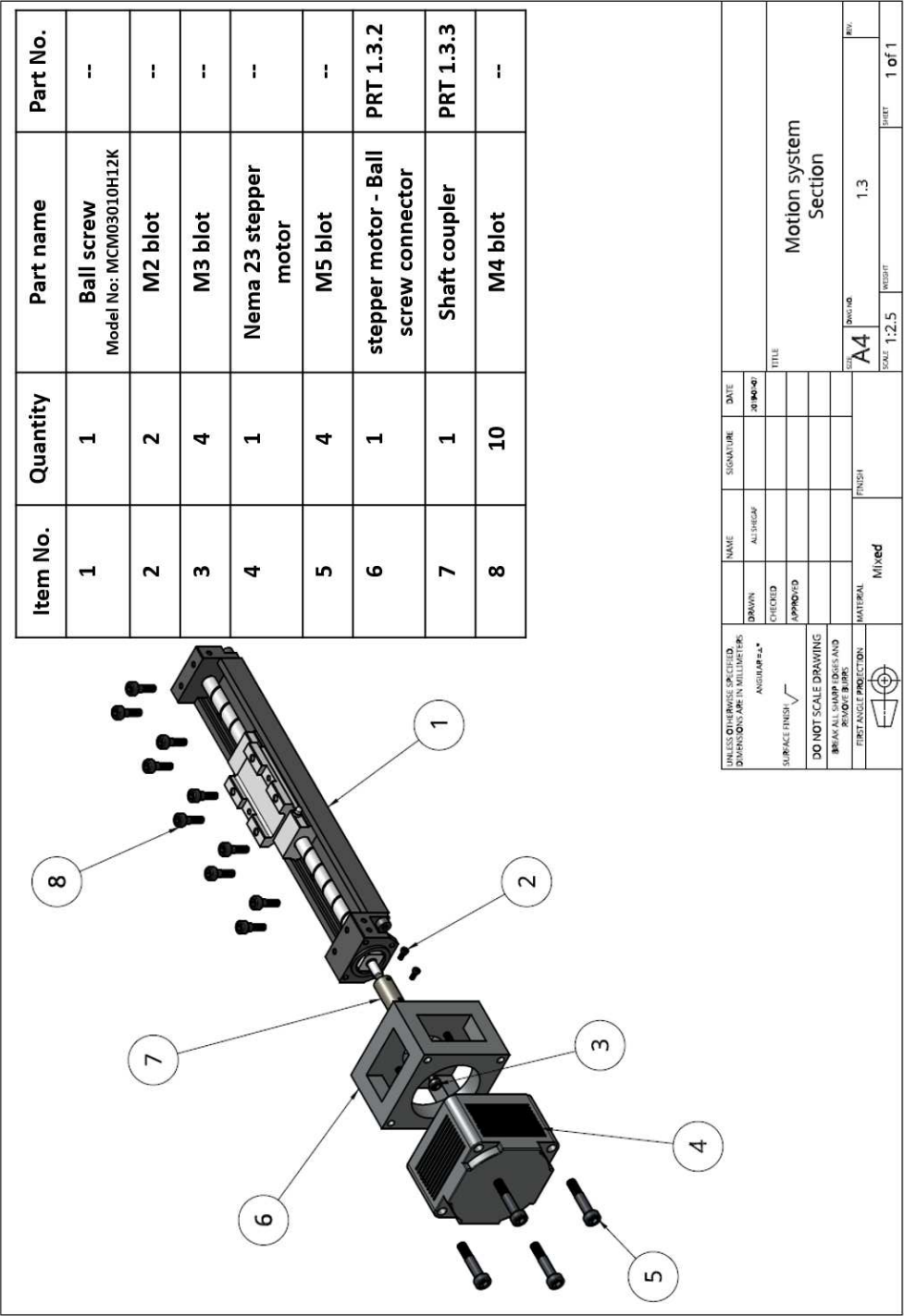
Figure B.11: Exploded view of the sliding motion section.
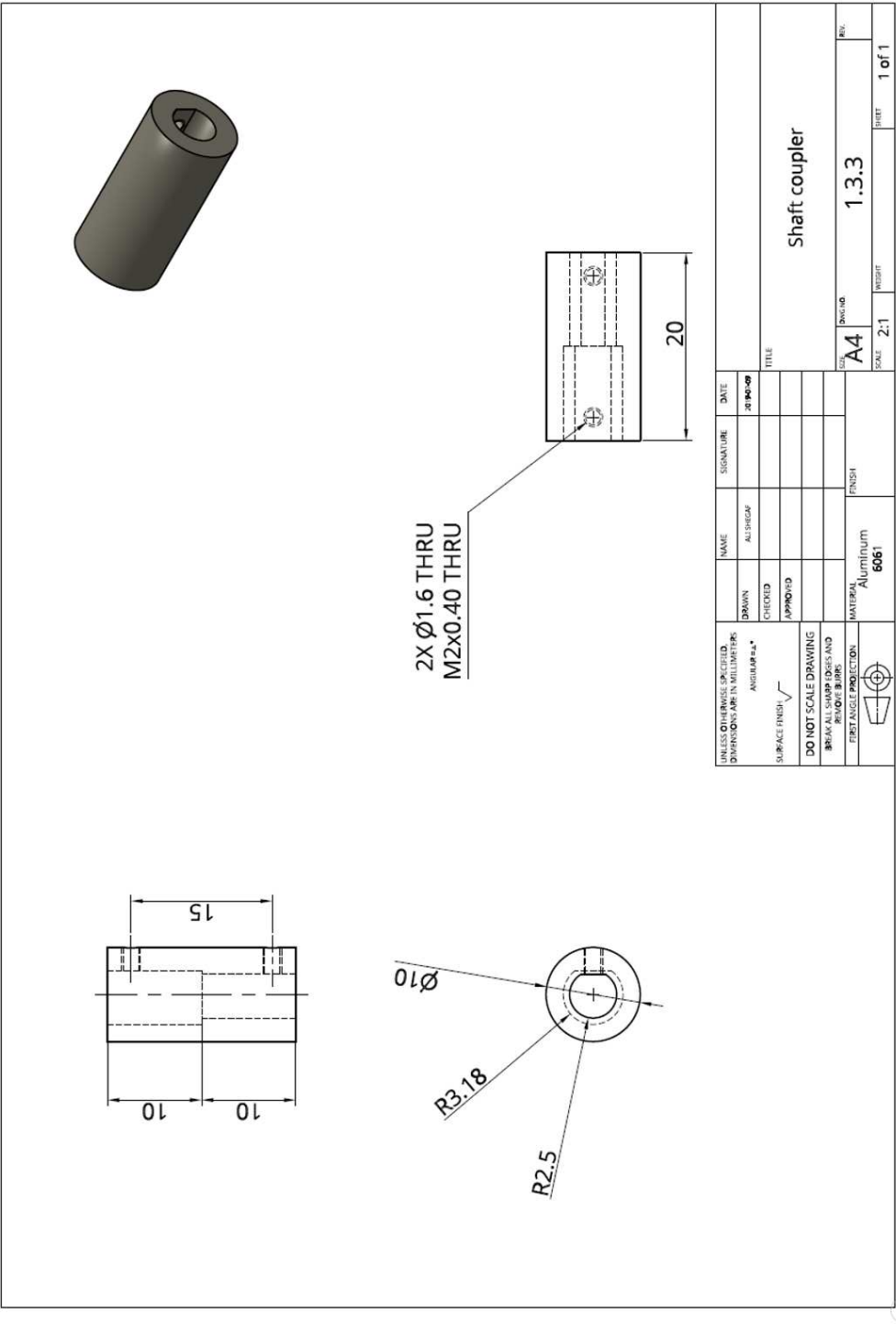
Figure B.12: Shaft coupler.
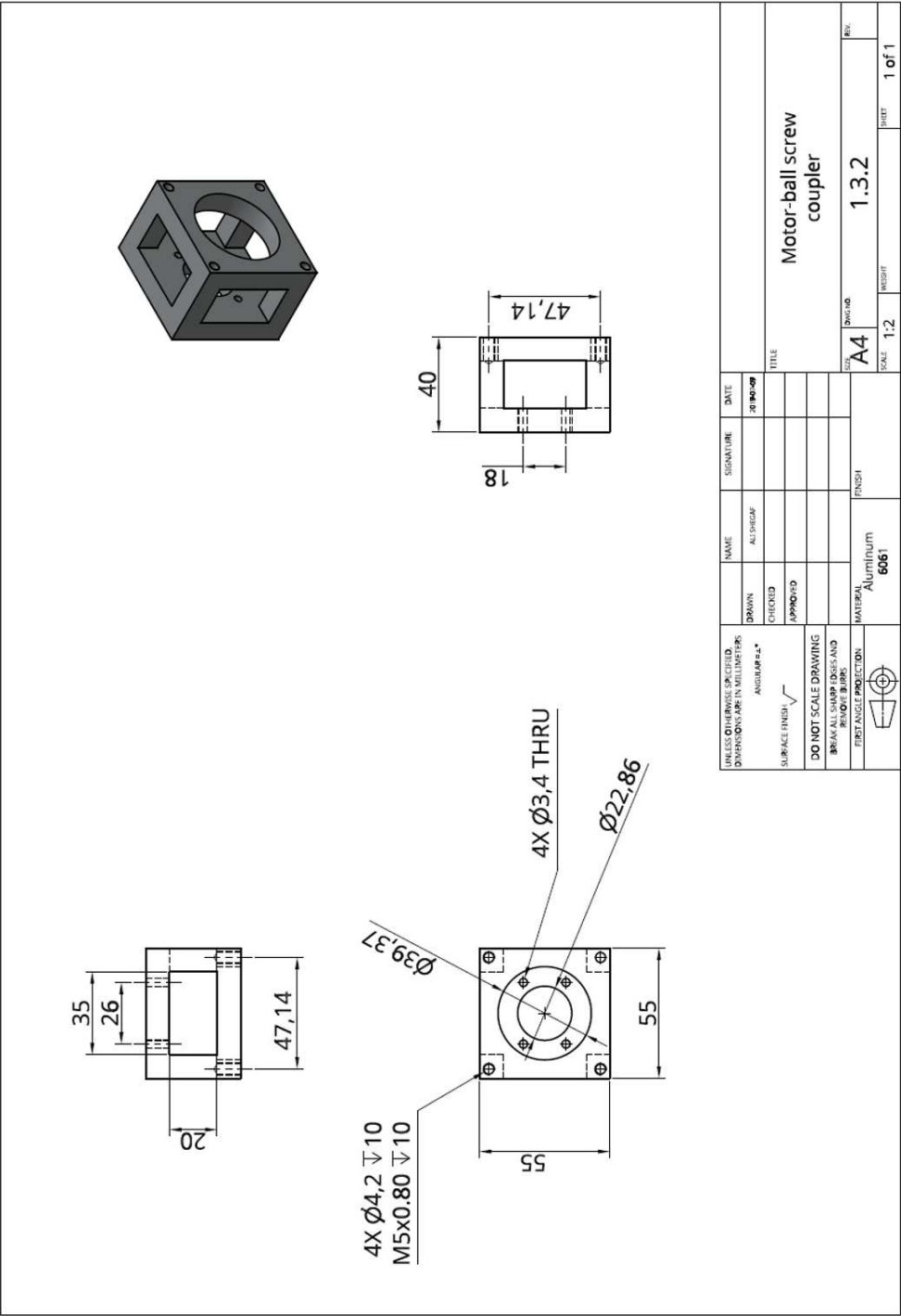
Figure B.13: Motor-Ball screw Connector.

Item No.	Quantity	Part name	Part No.
1	1	Apparatus main base	PRT 1.4.1
2	2	Specimen bath lower base	PRT 1.4.2
3	4	Ball screw base	PRT 1.4.3
4	1	Specimen bath base	PRT 1.4.4
5	8	M4 blot	--
6	2	Specimen bath vertical stand	PRT 1.3.2
7	8	M5 blot	--
8	8	M5 washer	--
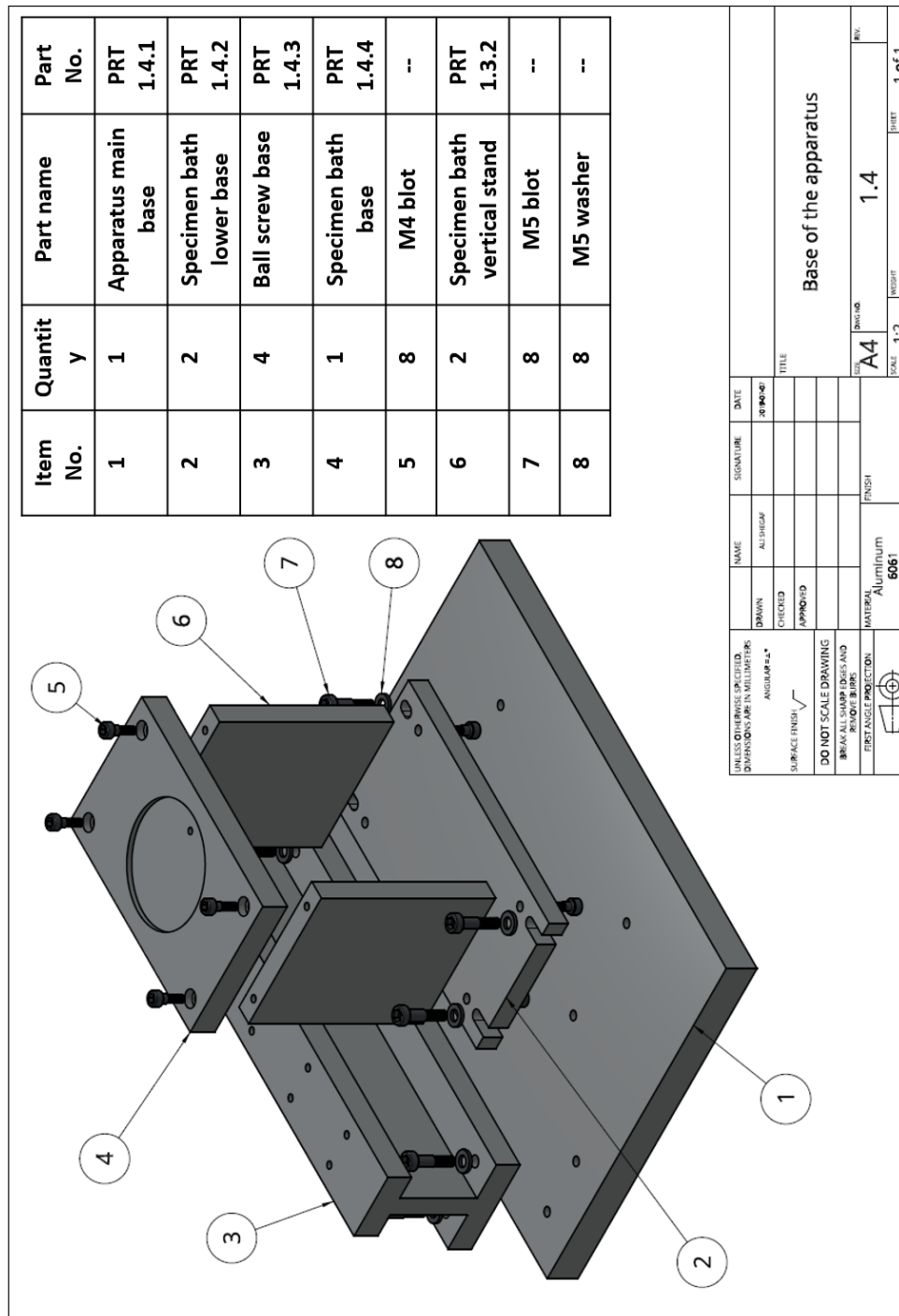
Figure B.14: Exploded view of the base of the biaxial apparatus.
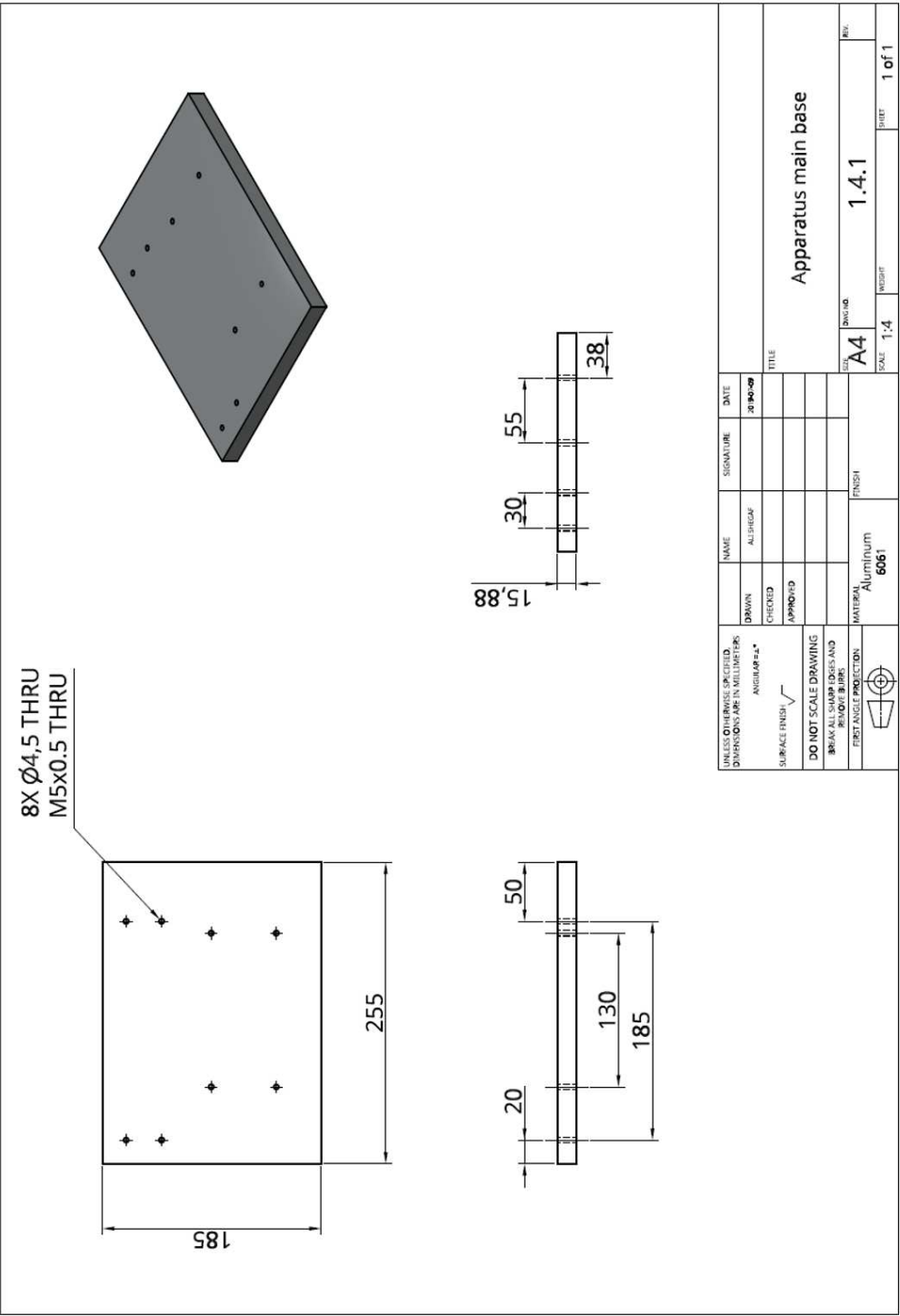
Figure B.15: Apparatus main base.
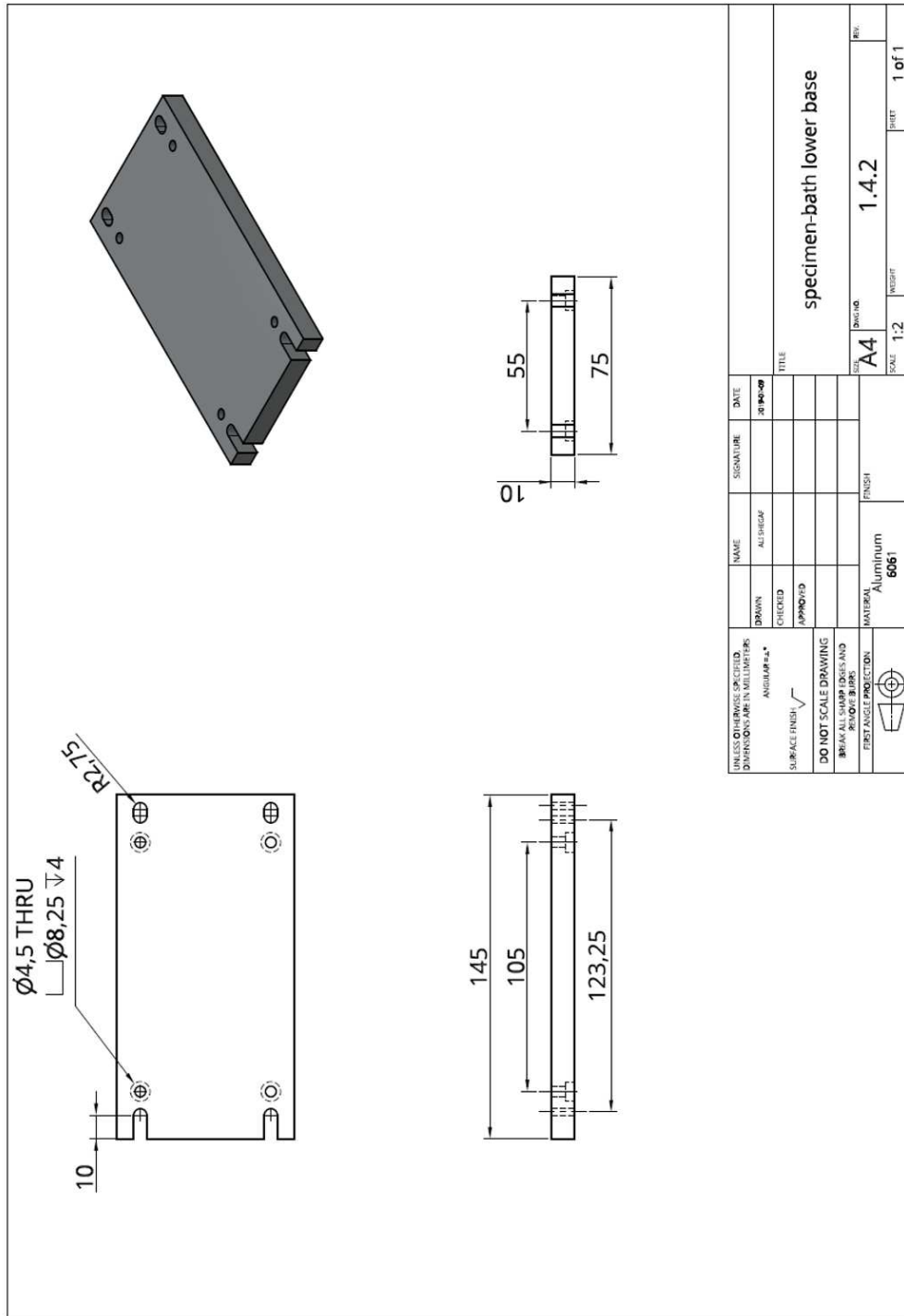
Figure B.16: Specimen bath bottom base.
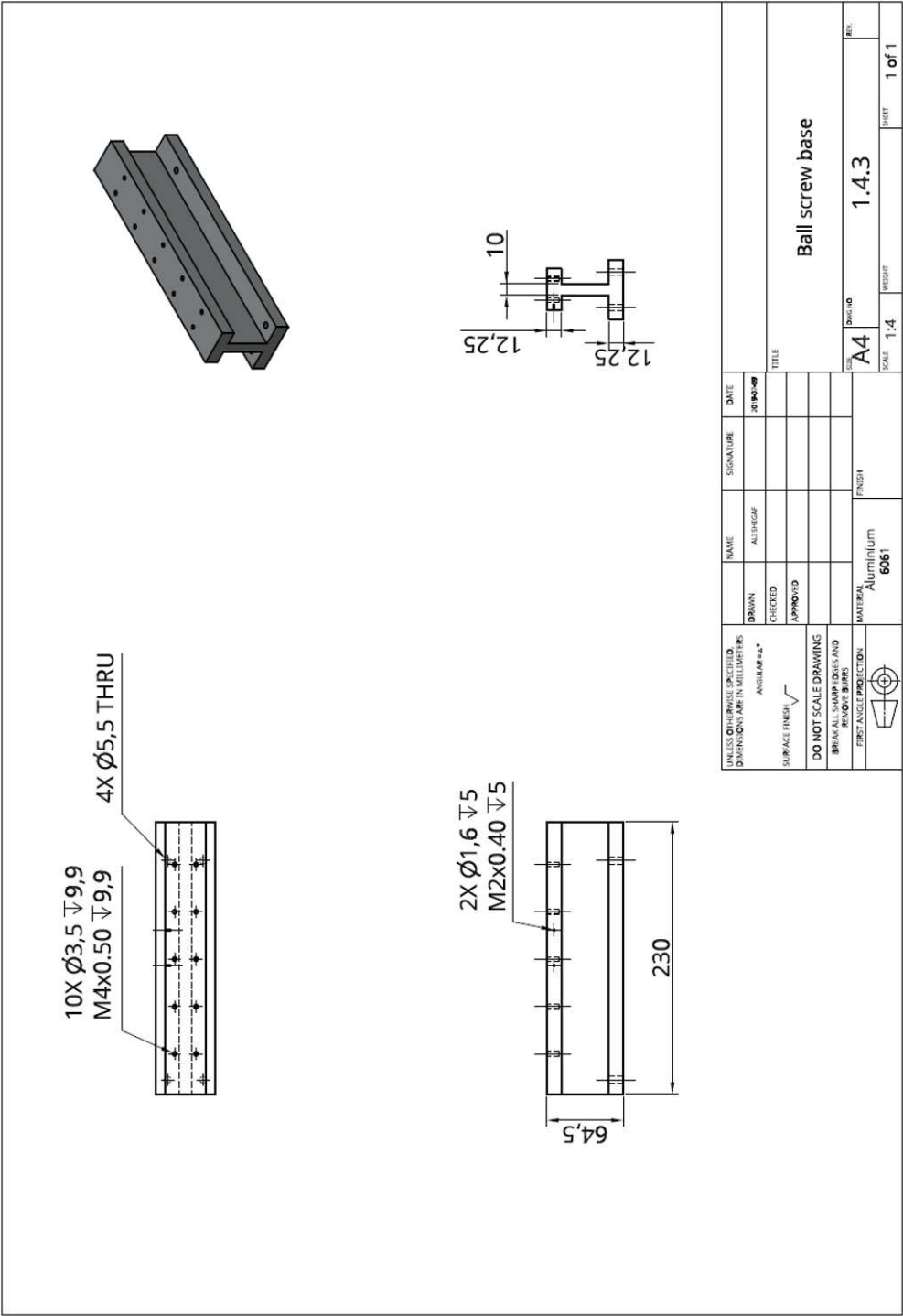
Figure B.17: Ball screw base.
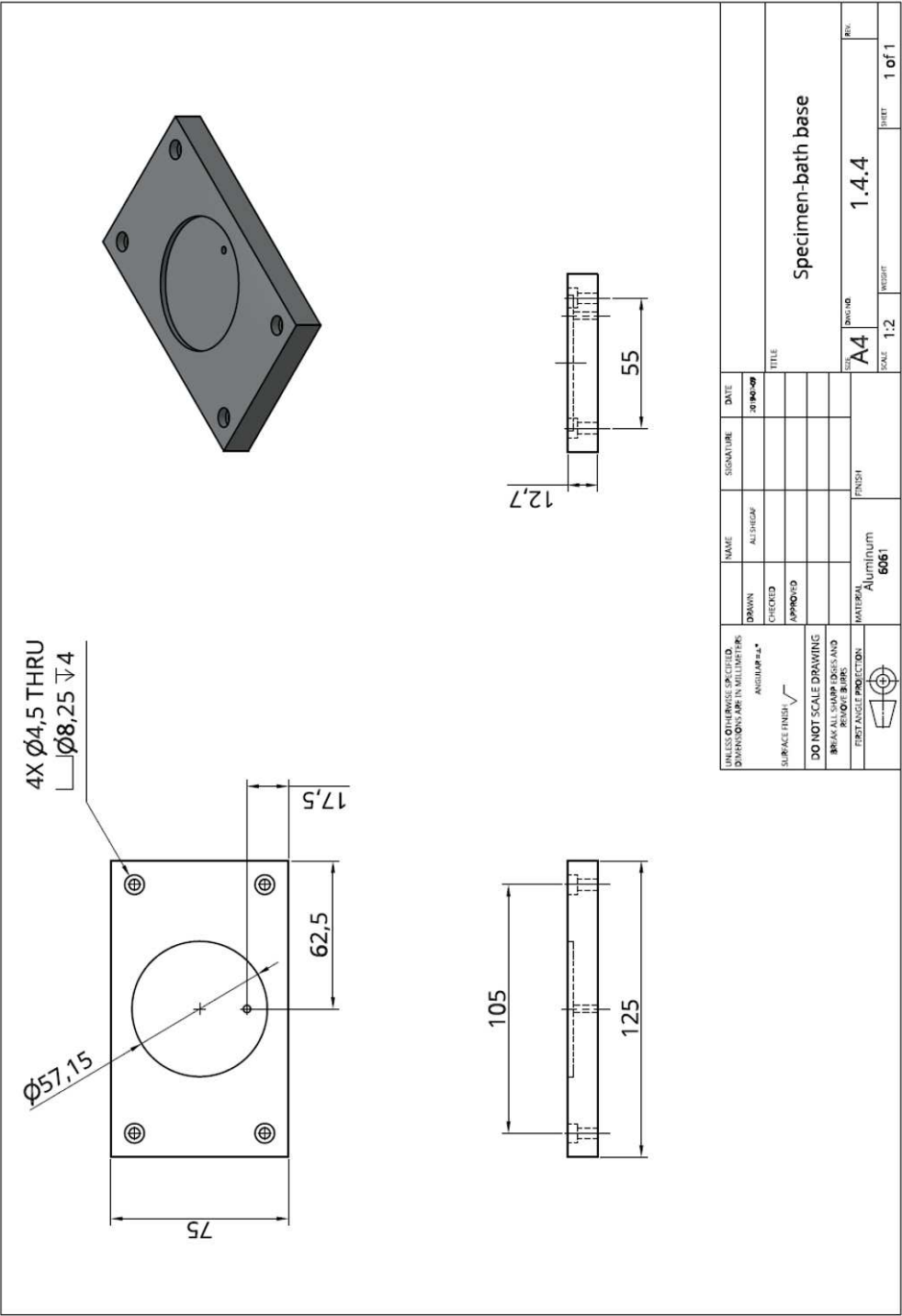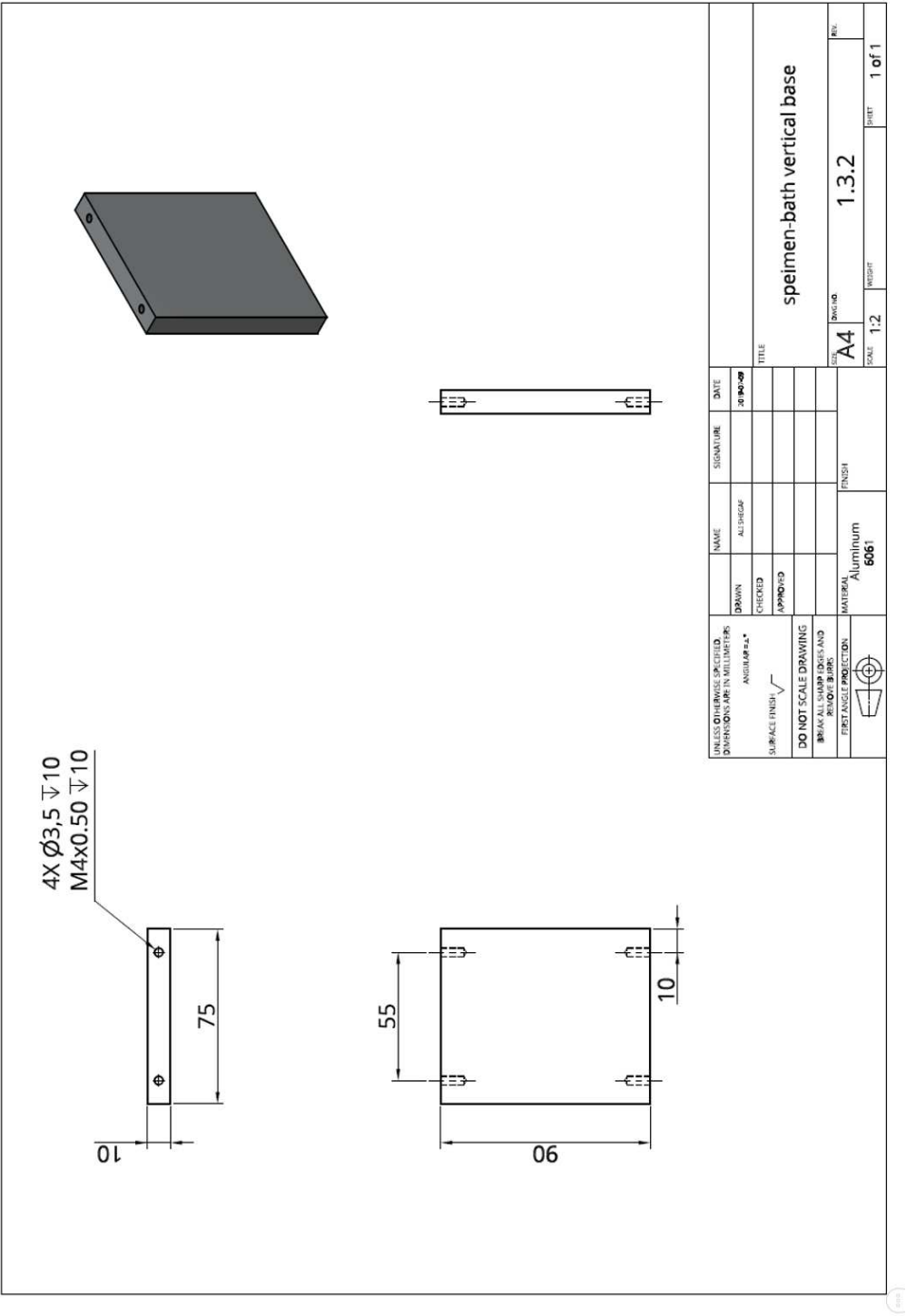
Figure B.18: Specimen bath base.

Figure B.19: Specimen bath base vertical support.

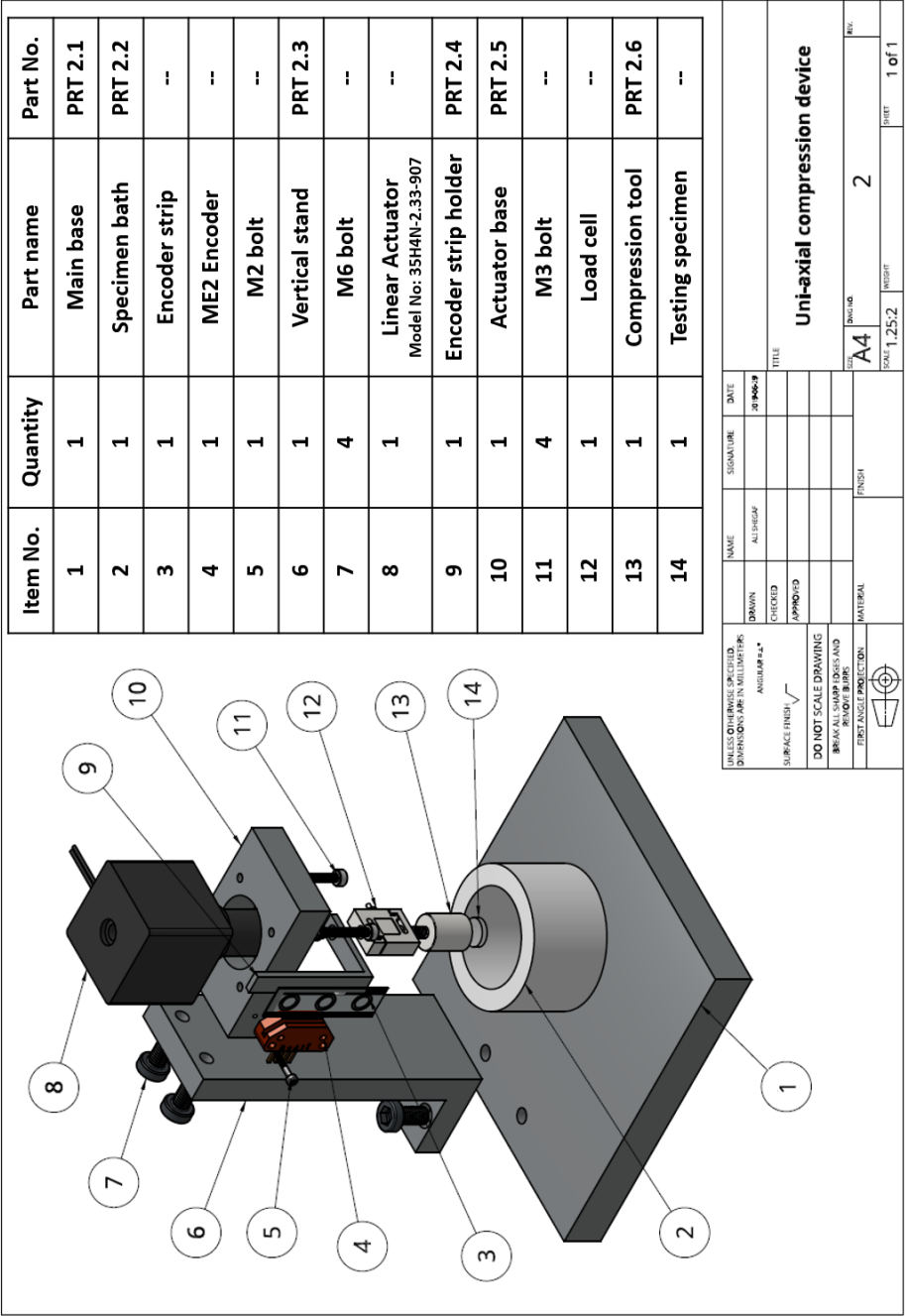## B.2 Engineering Drawings for Uni-axial compression Apparatus

Item No.	Quantity	Part name	Part No.
1	1	Main base	PRT 2.1
2	1	Specimen bath	PRT 2.2
3	1	Encoder strip	--
4	1	ME2 Encoder	--
5	1	M2 bolt	--
6	1	Vertical stand	PRT 2.3
7	4	M6 bolt	--
8	1	Linear Actuator Model No: 35H4N-2.33-907	--
9	1	Encoder strip holder	PRT 2.4
10	1	Actuator base	PRT 2.5
11	4	M3 bolt	--
12	1	Load cell	--
13	1	Compression tool	PRT 2.6
14	1	Testing specimen	--

Uni-axial compression device

Figure B.20: Uni-axial compression Apparatus: Exploded view.
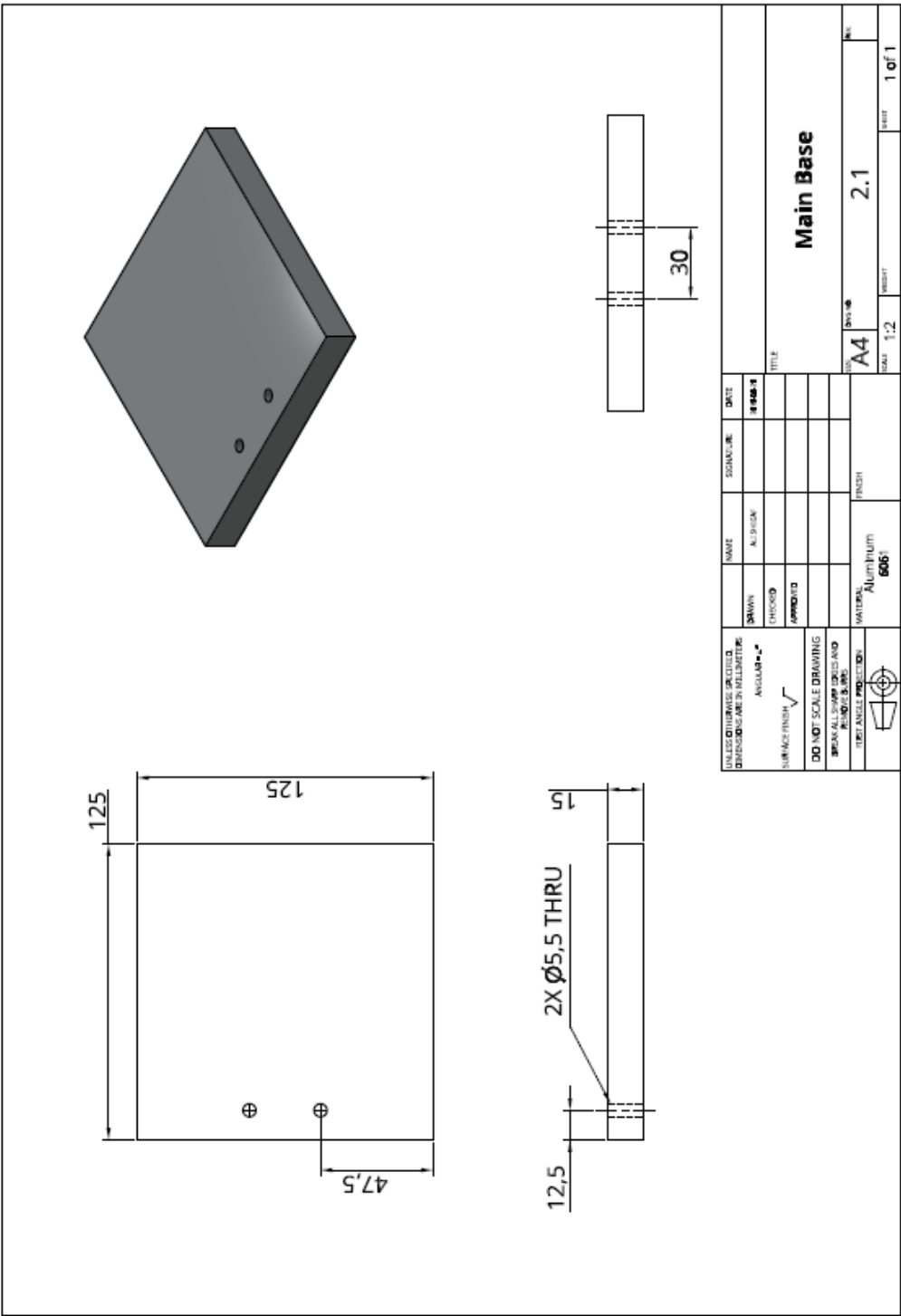
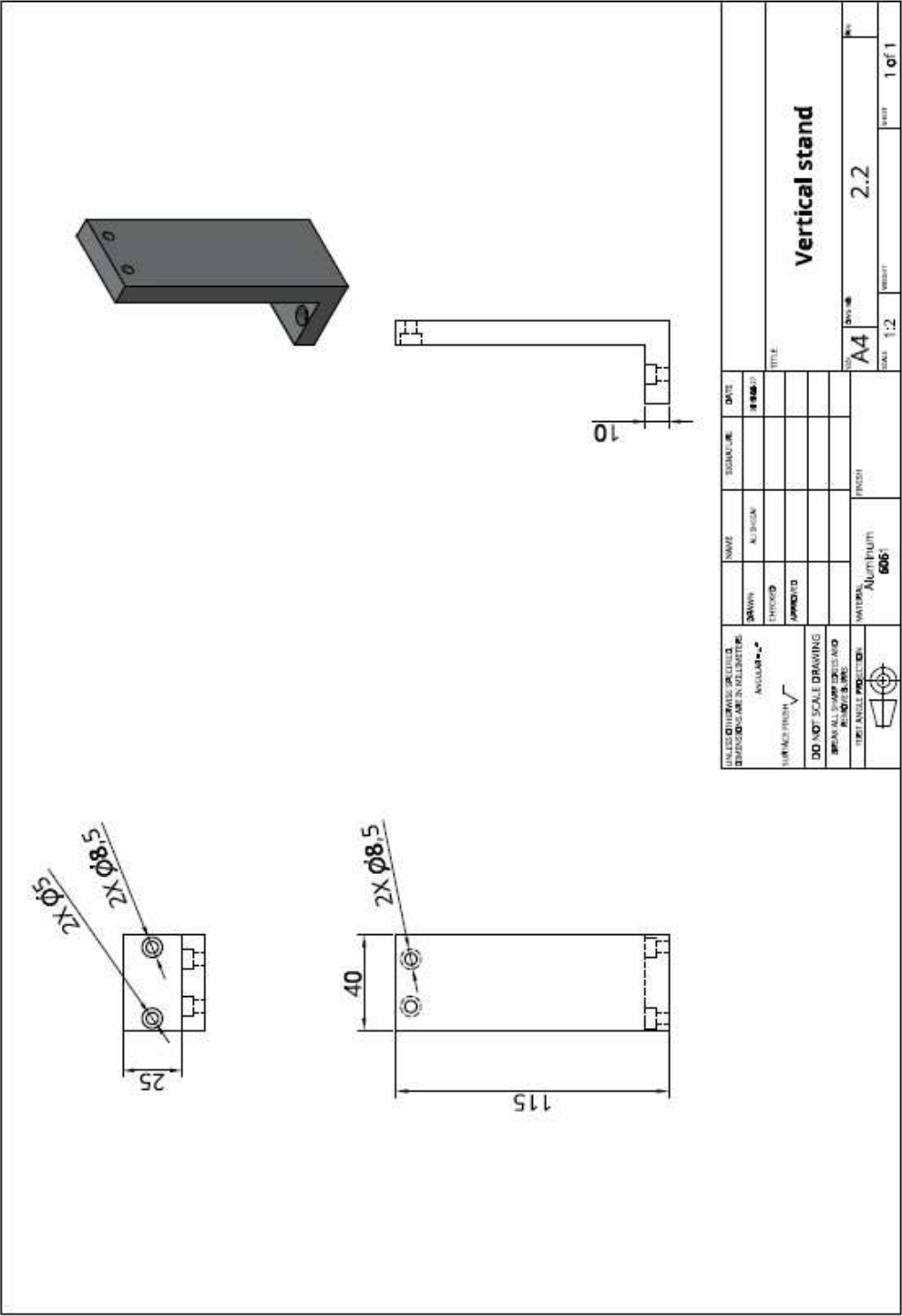**Figure B.21:** Apparatus main base).
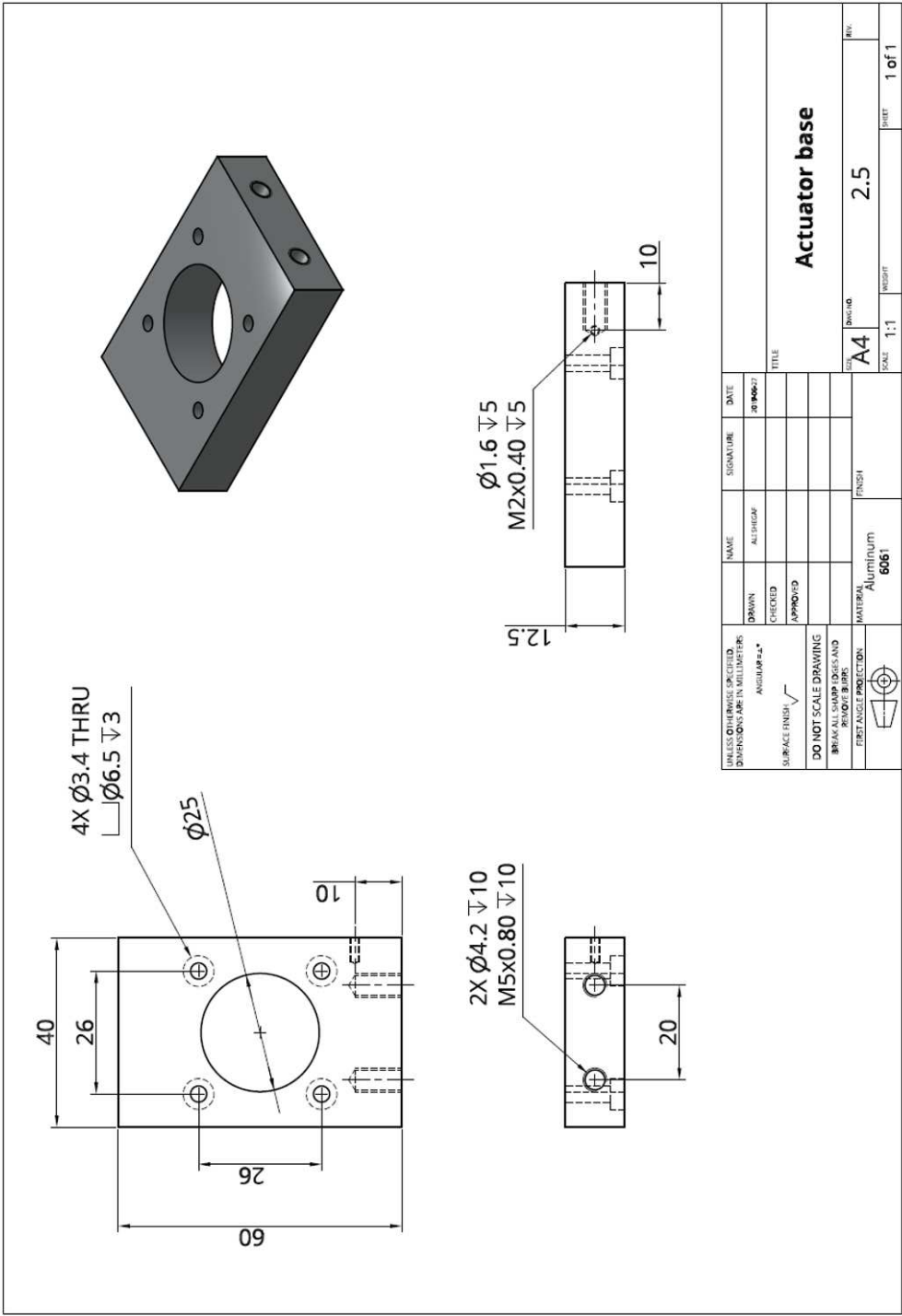
Figure B.22: Vertical stand).
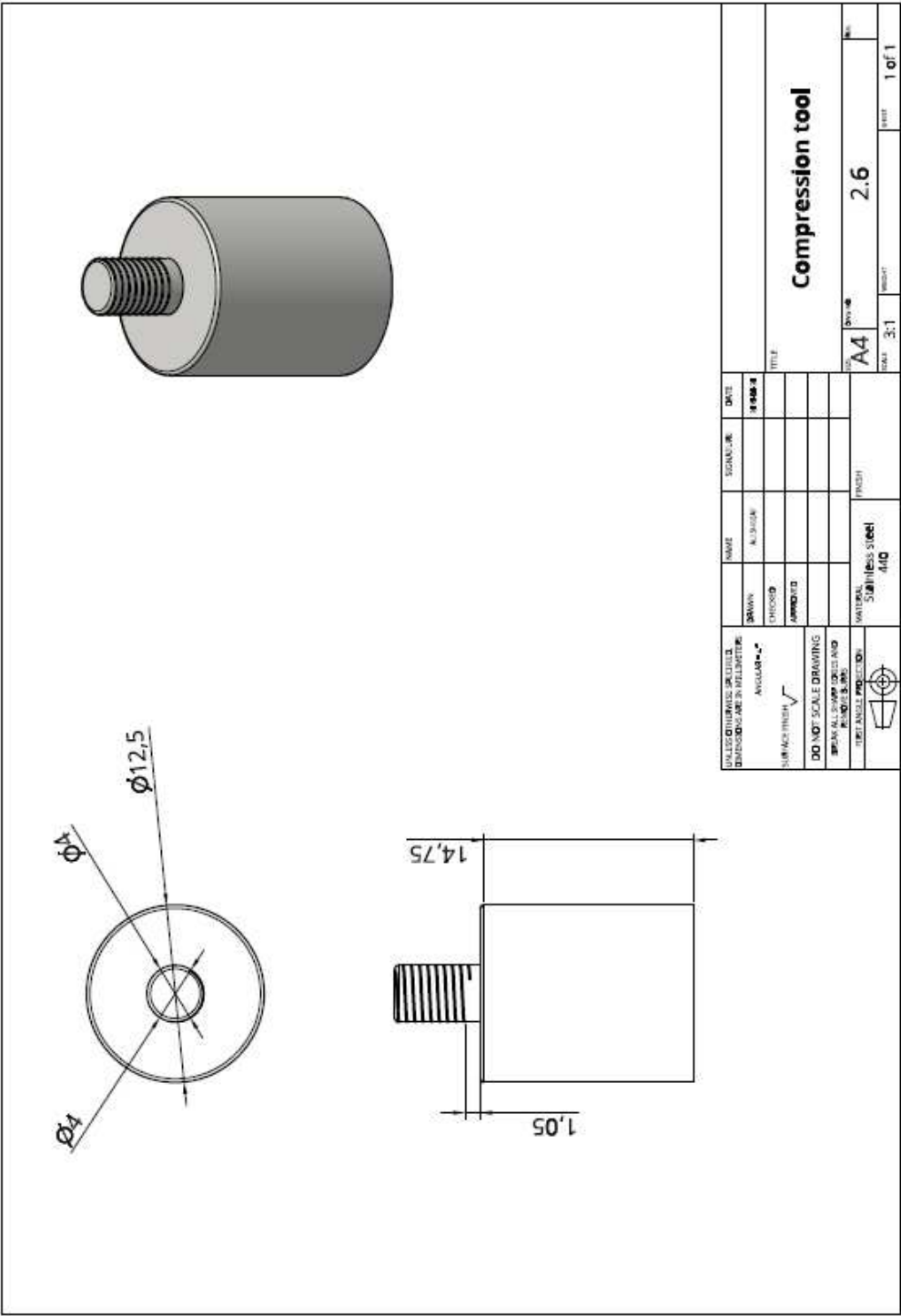
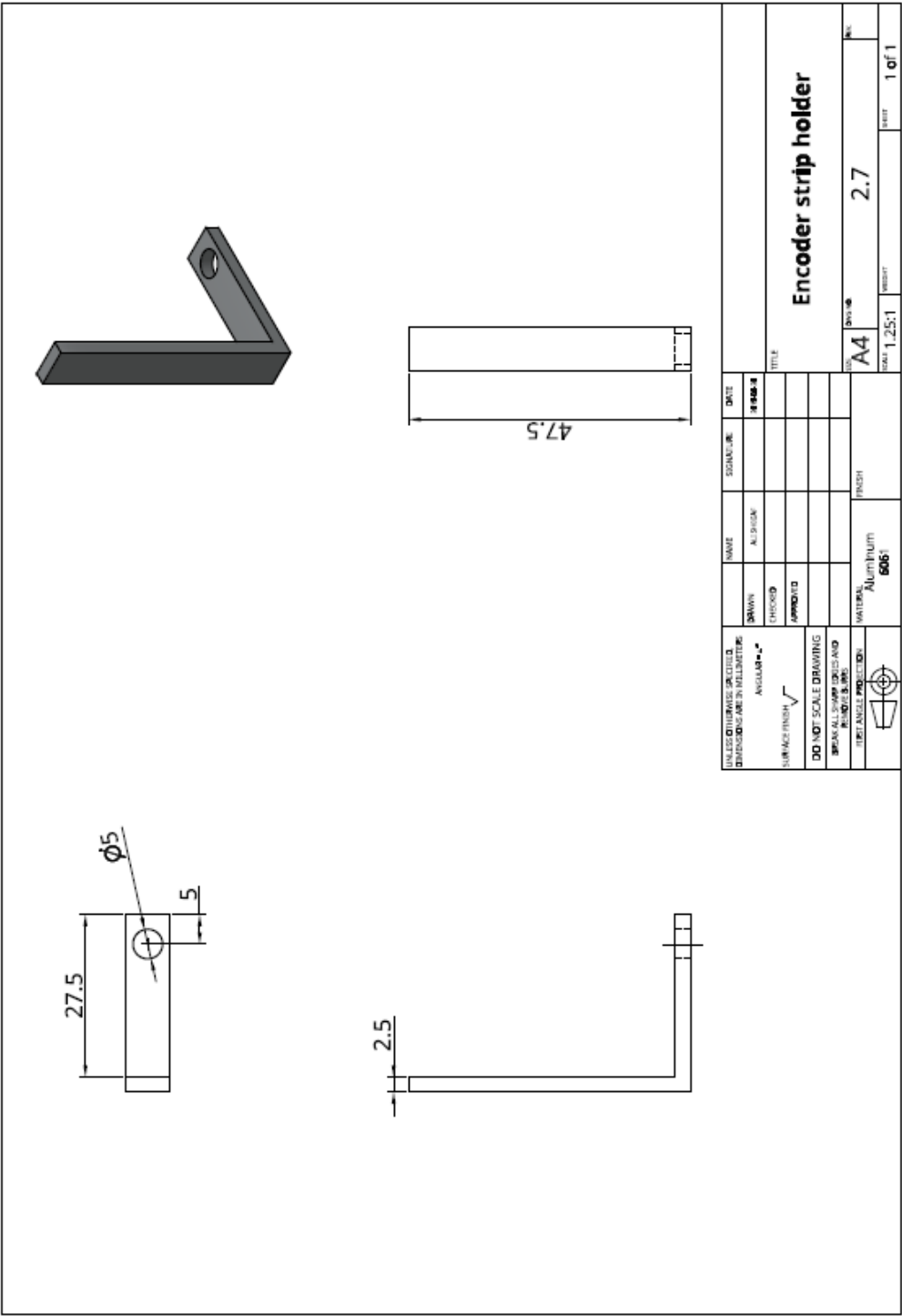**Figure B.23:** Linear actuator base.

Figure B.24: Compression tool for unconfined compression.

Figure B.25: Encoder strip holder.